SOFT MATERIAL PLATFORM FOR ROBOTICS AND ENERGY HARVESTING

A Dissertation

by

SINA BAGHBANI KOEDMAHALE

Submitted to the Office of Graduate and Professional Studies of
Texas A&M University
in partial fulfillment of the requirements for the degree of

DOCTOR OF PHILOSOPHY

Chair of Committee,	Jun Kameoka
Co-Chair of Committee,	Pao-Tai Lin
Committee Members,	Anastasia H. Muliana
	Kamran Entesari
Head of Department,	Miroslav M. Begovic

May 2021

Major Subject: Electrical Engineering

Copyright 2021 Sina Baghbani Kordmahale

ABSTRACT

Using Soft materials in the design and fabrication of new devices and structures that can carry out various tasks became appealing. While the different properties of materials (e.g., mechanical, thermal, electronic, optical, etc.) can be combined to achieve some functionality for specific devices, using soft materials and their special characters can bring unique functionality for the devices which may not be fabricated from rigid structures.

Choosing proper characteristics of soft material and using those properties in a proper design and combining the different characteristics of various materials can bring novel devices and tools to existing to handle new applications from safe handling and manipulation of a fragile specimen, to medical applications, to sustainability and green energy harvesting.

In this research, a micro-scale hydraulic/pneumatic soft gripper developed, and the handling of live specimens was demonstrated. This gripper was built with PDMS using the molding technique. From the optical characterization under the microscope, the bending-volume specification was determined, and the force-volume characterization was achieved by using a microforce sensor. The simulation of the structure was done using Abaqus software. The characterization and simulations showed a good level of agreement.

Also in this research, a new soft wave energy converter (SWEC) platform is developed by combining soft material and piezoelectric fibers. With the abundance of ocean coverage on the earth, wave energy conversion platforms can provide a high percentage of green energy demands. Currently, there are multiple types of wave energy converters that have drawbacks like being very large, require a high cost of deployment and maintenance. To decrease the maintenance cost and

increase the power generation efficiency, we proposed to develop a SWEC by integrating soft material with piezoelectric fibers as a low-cost, maintenance-free device. A Macro Fiber Composite and bubble wraps, for floatation, are integrated into a soft elastomer Ecoflex sheet. The power generation efficiency of the device has been investigated in a wave tank and its conversion ability from water waves has been proved. The promising wave energy harvesting capability combined with low cost and no maintenance can impact the SWECs platforms development and their real-world applications.

DEDICATION

Dedicated to my beloved family

To my Maman, Baba, and Dadash Ali

None of this would have been possible without their support

ACKNOWLEDGEMENTS

I would like to express my deepest gratitude to my advisor, Prof. Jun Kameoka for his tremendous help and support during my years of study and research at Texas A&M University. His immense knowledge impacted and determined the path of my research and guided me through my Ph.D., and I learned a lot from his research doctrine. Working with him was a great step toward being a more mature and passionate researcher. My growth was obvious to myself and I observed how my research standards improved under his supervision. I learned a lot of useful lessons in my life, and I must be appreciative of all of them.

Furthermore, I also want to thank the following dissertation committee members: Prof. Anastasia H.Muliana for her constant consultation and assistance, and Prof. Kamran Entesari and Prof. Pao-Tai Lin for their time and support.

In addition, I would like to express my most sincere appreciation to those faculty members from various departments at Texas A&M University that were my collaborators, Profs. Anastasia H.Muliana (Mechanical Engineering), Kamran Entesari (Electrical Engineering), Roland R.Kaunas (Biomedical Engineering), Kuang-An Chang (Ocean Engineering & Civil Engineering), Darren Hartl (Aerospace Engineering), Gerard L.Cote (Biomedical Engineering), and Jens Figlus (Ocean Engineering-Galveston Campus). I deeply appreciate their dedication, providing equipment and lab facilities, teamwork spirit, share of expertise, and overall support. Working with them was a privilege for me to expand my professional expertise and knowledge.

Working in several research groups at Texas A&M, I had several collaborators and worked with wonderful student researchers that I want to acknowledge their support. These student

researchers include Onder, Po-Jung, Ting, Zach, Sravani, Samarasing, Eli, Ana, Oscar, Mohit, Xiaohan, Alireza, Reza, Ali, Jaskirat, Manya, Rajiv, and Ashkan.

I spent a significant time researching at the nanofabrication facility named “Aggiefab”. During the years of working at Aggiefab, many people helped me in my projects. I cannot mention all of their names but I appreciate all their help in providing proper service, equipment, training, and technical and scientific expertise, especially Mr.Larry Rehn, Dr.Ming-Wei Lin, Mr.Robert Atkins, Mr.Donnald A.Marek, and Dr.Manoochehr Teimouri.

During the years at Texas A&M University, I had the chance to be the mentor of four M.Sc. students and their collaborator simultaneously. The chance of mentoring Rijiv, Manya, Ana, and Oscar and collaborating with them was one of the most challenging tasks I had during my Ph.D. I tried to show the highest level of commitment toward the collaborative projects. It was a great opportunity to understand the ambitions of master students and practice mentoring styles based on the cultural background of each individual student.

And last, but not least I want to express my appreciation and love from the bottom of my heart toward my family; Baba, Maman, and Dadash Ali. I could not have done this without their support and dedication. I thank them for being the best family members any person on this planet can wish for. I thank them for supporting me through my journey. I thank them for assuring me they are there for me in any circumstances. I thank them for their selfless, forgiving, and unconditional love. I cannot find proper words to appreciate my dad to be a perfect teacher and supporter for me. To find time for me in any condition, to respond to my infinite questions, or spend time to find the proper person to answer these endless questions that guided me toward

my professional ambitions. Still, the experiments my dad and I did together are the most exciting experiments of my life. About my mom, I cannot tell if she was just a teacher or a kind mom. She taught me how to love myself. She taught me to be responsible and have commitment. She taught me how to be patient and have the dedication to achieve my goals. I am so thankful to have Mom and Dad. And I thank them for working so hard in their lives to enable me to go where I am. I am very appreciative to have Dadash Ali as my big brother. He is not just supportive and smart. He is a true friend. A very different person with a modern personality ahead of society. I cannot believe still the best movies I enjoyed are the movies I watched with him, the best books I read are the books I picked from his library, the best articles have been the ones he sent to me. I am very lucky to be the youngest member of this family.

CONTRIBUTORS AND FUNDING SOURCES

Contributors

This work was supervised by a dissertation committee consisting of Professor Jun Kameoka [advisor] and Professor Kamran Entesari of the Department of Electrical and Computer Engineering, Professor Pao-Tai Lin [co-advisor] of the Department of Material Science and Engineering, and Professor Anastasia H.Muliana of the Department of Mechanical Engineering.

The simulations depicted in Chapter 2 were conducted by Jian Qu of the Department of Mechanical Engineering.

All other work conducted for the dissertation was completed by the student independently.

NOMENCLATURE

MFC	Macro Fiber Composite
WEC	Wave Energy Convertor
OWEC	Open water Wave Energy Convertor
SWEC	Soft Wave Energy Converter
MIS	Minimally Invasive Surgery
PDMS	Polydimethylsiloxane
OTS	Octadecyltrichlorosilane
SAM	Self-assembled monolayer
TCE	Trichloroethylene
UCT	United Chemical Technologies
IPA	Isopropyl Alcohol
N_2	Nitrogen
TI	Texas Instruments
PCB	Printed Circuit Board

TABLE OF CONTENTS

LIST OF FIGURES

LIST OF TABLES

CHAPTER I

INTRODUCTION

1-1-Introduction and Motivation

New materials brought new possibilities to various disciplines like sustainable energy harvesting, robotics, medical devices, sensors, and remote sensing [1-5]. Polymeric elastomers are among materials that can bring various required properties into many fields. Optical transparency of some elastomers makes them suitable to be used in optical systems [6,7]. Most of the elastomers are temperature and electricity isolators that can be used for proper isolation in various applications [8,9]. Some polymers can endure autoclave sterilizing temperatures that make them appealing for biomedical applications [10]. Because the polymers' mass density is lower than materials like Silicon and metals, the use of them can lead to lighter devices [11]. The mechanical properties of soft elastomers are adjustable; this gives higher freedom to the device designer to use hyperelastic or brittle polymeric structures based on the requirements [12,13]. Enduring harsh chemical media and be inert is another advantage of some polymeric materials and can be used in the design and fabrication of required structures [14]. The low price of material and fabrication process is another advantage of this family of materials. The low cost, fast, and highly parallel soft material casting is a suitable method to form elastomers in a proper way to fabricate required structures [15,16].

As an alternative to hard-material robotics, soft material-based robots are popular to handle fragile biospecimen and objects [17,18]. They can be used for in-vivo and in-vitro biomedical grabbing and manipulation [18-20]. Biologists can use biofriendly and biocompatible

soft material-based robots to handle delicate organisms in their natural environment [21]. For instance, soft polymeric robots can be functional in harsh environments and endure chemicals like corrosive salt water while they are manipulating marine biospecimen [22]. In the field of surgery that is under constant evolution, soft robots can be used in minimally invasive surgery to minimize soft tissue damage during the procedures [23,24]. In addition, it can be used as the developed technology to address the requirements of flexible access surgery [25]. While there are still efforts to miniaturize soft robots to the microscale, finding efficient actuators for microscale soft robots is still a challenge [26]. Because of this, it is difficult to copy the industrial and bigger size soft robots and miniaturize them directly [27]. To achieve a proper micro-size soft-robot, new designs should be combined with new fabrication techniques.

Borrowing the characteristics of soft materials and using them to invent new types of energy harvesters, can open new horizons toward green energy conversion as a sustainable source [28]. Elastomers are naturally flexible, bendable, lightweight, and with a low-cost fabrication and forming process [29]. That makes them an attractive candidate for encapsulation purposes of electrical elements and transducers for working in harsh chemical mediums [30,31]. Mechanical vibration is one of the abundant sources of green energy that can be found on Earth [32]. One of the sources of vibrational mechanical energy that can be used as green energy is the water wave [33]. Some types of water wave energy converters are commercially available [34]. However, the high maintenance and high deployment costs, releasing chemicals into the water, and making sound pollution are disadvantages of these water wave energy converters [35,36].

Already, among the investigated water wave energy harvesters, different types of transducers have been used. Various types of transducers to convert mechanical vibrational

energy to electrical energy are working based on various physical phenomena like electromagnetic, electrostatic, triboelectric, and piezoelectric, or a combination of the four [37,38]. These ones have been extensively investigated. Vibrational energy conversion to electrical energy in each convertor can happen by the use of one or a combination of these types of transducers [39]. A device developer to overcome shortcomings of available energy harvesting systems, can combine proper characters of the soft materials with transducers and introduce an energy harvester with the required characteristics. For instance, among various piezoelectric converters, some piezoelectric patches are flexible. Macro Fiber Composites (MFCs) are intriguing options to be integrated into soft materials to form bendable and floatable water wave energy converters (WECs) [40].

1-2-Dissertation Structure

In the following chapter "Soft Material and development of soft robotics" after the literature review and the detailed motivation, the design strategy will be introduced. The actuation mechanism that is described is an actuating membrane works based on pressure difference on two sides of a flexible membrane. Also, it is described how the proper fingers in the introduced designs can be placed on the membrane and form the required monolithic microgripper. This introduced structure can be a hydraulic/pneumatic microgripper. The fabrication steps and required materials also are described. PDMS is chosen as the fabrication material and low-cost soft material molding is described as the fabrication method. Three different soft material-based grippers are described in this chapter. Two monolithic micro grippers based on the PDMS with the same mechanism and different shapes are described. Also, another gripper was developed, suitable for minimally invasive surgery, which is a combined

structure made from soft material and 3D printed parts. These microgrippers were successfully characterized and their ability to grab live bio specimen were approved by grabbing an ant. The handling of a piece of chicken was done successfully by a hybrid gripper to mimic the soft abdominal tissue manipulation. This proved the ability of the developed device, which is compatible with standard trocars, to be useful for abdominal minimally invasive surgery.

In chapter 3 of this dissertation, "Soft materials and development of hybrid structure of piezoelectric transducers and soft materials as wave energy converter," the possibility of blue energy harvesting based on the developed platforms by using biofriendly soft materials is investigated. For this research, Ecoflex is chosen as the soft elastomer to form the proper platform and encapsulation of other elements. A Wave Energy Converter (WEC) is designed based on this elastomer. To overcome the common drawbacks of the current WECs, a WEC encapsulated in a biofriendly soft materials sheet is designed, fabricated, and investigated successfully. To form a flexible, floatable, and bendable WEC to overcome the common drawbacks of the conventional blue energy harvesters, a proper piezoelectric transducer was chosen to be the conversion element. Macro Fiber Composite (MFC) is chosen as a flexible transducer. Integration of a piece of commercial bubble wrap in the elastomer, alongside piezoelectric transducers and electrical connections, inside the Ecoflex elastomer sheet formed the proper WEC. After fabrication of the WECs with various numbers of the MFCs, they were placed in wave fume tanks and their functionality was investigated. The output of the WECs was connected during the experiments to a diode bridge AC-DC converter. The outputs in this way were recorded and compared with each other and the optimized number of integrated MFCs in

each WEC was recognized. The effects of anchoring were also experimented successfully in this dissertation and explained in Chapter 3.

In chapter 4, “Summary and Future Works,” a summary of the research presented in various chapters of this dissertation is shown. Innovative suggestions for future works are also mentioned.

1-3-Bibliography

1) G. X. Liu *et al.*, “Soft Tubular Triboelectric Nanogenerator for Biomechanical Energy Harvesting,” *Adv. Sustain. Syst.*, vol. 2, no. 12, pp. 1–8, 2018, doi: 10.1002/adsu.201800081.

2) C. Majidi, “Soft-Matter Engineering for Soft Robotics,” *Adv. Mater. Technol.*, vol. 4, no. 2, pp. 1–13, 2019, doi: 10.1002/admt.201800477.

3) K. Vithani, A. Goyanes, V. Jannin, A. W. Basit, S. Gaisford, and B. J. Boyd, “An Overview of 3D Printing Technologies for Soft Materials and Potential Opportunities for Lipid-based Drug Delivery Systems,” *Pharm. Res.*, vol. 36, no. 1, pp. 1–20, 2019, doi: 10.1007/s11095-018-2531-1.

4) M. Qin, M. Sun, M. Hua, and X. He, “Bioinspired structural color sensors based on responsive soft materials,” *Curr. Opin. Solid State Mater. Sci.*, vol. 23, no. 1, pp. 13–27, 2019, doi: 10.1016/j.cossms.2018.10.001.

5) S. Gong, L. W. Yap, B. Zhu, and W. Cheng, “Multiscale Soft–Hard Interface Design for Flexible Hybrid Electronics,” *Adv. Mater.*, vol. 32, no. 15, pp. 1–28, 2020, doi: 10.1002/adma.201902278.

6) B. Karunakaran, J. Tharion, A. R. Dhawangale, D. Paul, and S. Mukherji, “Fabrication of miniature elastomer lenses with programmable liquid mold for smartphone microscopy: curing

polydimethylsiloxane with in situ curvature control," *J. Biomed. Opt.*, vol. 23, no. 02, p. 1, 2018, doi: 10.1117/1.jbo.23.2.025002.

7) X. Huang *et al.*, "Adaptive electrofluid-actuated liquid lens," *Opt. Lett.*, vol. 45, no. 2, pp. 3–6, 2020, doi: 10.1364/OL.45.000331.

8) S. H. Jeong *et al.*, "Mechanically Stretchable and Electrically Insulating Thermal Elastomer Composite by Liquid Alloy Droplet Embedment," *Sci. Rep.*, vol. 5, no. September, pp. 1–10, 2015, doi: 10.1038/srep18257.

9) Z. Xing *et al.*, "Investigation of the thermal conductivity of resin-based lightweight composites filled with hollow glass microspheres," *Polymers (Basel).*, vol. 12, no. 3, pp. 1–15, 2020, doi: 10.3390/polym12030518.

10) Y. Zhao, B. Zhu, Y. Wang, C. Liu, and C. Shen, "Effect of different sterilization methods on the properties of commercial biodegradable polyesters for single-use, disposable medical devices," *Mater. Sci. Eng. C*, vol. 105, no. July, p. 110041, 2019, doi: 10.1016/j.msec.2019.110041.

11) S. Chen, S. Peng, W. Sun, G. Gu, Q. Zhang, and X. Guo, "Scalable Processing Ultrathin Polymer Dielectric Films with a Generic Solution Based Approach for Wearable Soft Electronics," *Adv. Mater. Technol.*, vol. 4, no. 7, pp. 1–8, 2019, doi: 10.1002/admt.201800681.

12) M. Walter, M. Friess, S. M. H. Zolanvar, G. Grün, H. Kröber, and T. Pretsch, "Shape Memory Polymer Foam with Programmable Apertures," *Polymers (Basel).*, vol. 12, no. 1914, pp. 1–23, 2020, doi: 10.3390/polym12091914.

13) Y. Cao *et al.*, "Direct Fabrication of Stretchable Electronics on a Polymer Substrate with

Process-Integrated Programmable Rigidity," *Adv. Funct. Mater.*, vol. 28, no. 50, pp. 1–9, 2018, doi: 10.1002/adfm.201804604.

14) K. Mayandi *et al.*, "An overview of endurance and ageing performance under various environmental conditions of hybrid polymer composites," *J. Mater. Res. Technol.*, vol. 9, no. 6, pp. 15962–15988, 2020, doi: 10.1016/j.jmrt.2020.11.031.

15) A. P. Saghati, S. B. Kordmahale, J. Kameoka, and K. Entesari, "Reconfigurable Quarter-Mode Substrate Integrated Waveguide Cavity Filter Employing Liquid-Metal Capacitive Loading," in *2015 IEEE MTT-S International Microwave Symposium*, 2015, pp. 20–22, doi: 10.1109/MWSYM.2015.7166885.

16) A. P. Saghati, S. B. Kordmahale, A. P. Saghati, J. Kameoka, and K. Entesari, "Reconfigurable quarter-mode SIW antenna employing a fluidically switchable via," in *2016 IEEE Antennas and Propagation Society International Symposium, APSURSI 2016 - Proceedings*, 2016, pp. 845–846, doi: 10.1109/APS.2016.7696131.

17) M. Cianchetti, T. Nanayakkara, and T. Ranzani, "Soft Robotics Technologies to Address Shortcomings in Today ' s Minimally Invasive Surgery : The STIFF-FLOP Approach," *Soft Robot.*, vol. 1, no. 2, pp. 122–131, 2014, doi: 10.1089/soro.2014.0001.

18) N. R. Sinatra, C. B. Teeple, D. M. Vogt, K. K. Parker, D. F. Gruber, and R. J. Wood, "Ultragentle manipulation of delicate structures using a soft robotic gripper," *Sci. Robot.*, vol. 4, no. 33, pp. 1–12, 2019, doi: 10.1126/SCIROBOTICS.AAX5425.

19) A. Degani, H. Choset, A. Wolf, and M. A. Zenati, "Highly Articulated Robotic Probe for

Minimally Invasive Surgery," in *IEEE International Conference on Robotics and Automation*, May 2006, pp. 4167–4172.

20) M. Runciman, A. Darzi, and G. P. Mylonas, "Soft Robotics in Minimally Invasive Surgery," *Soft Robot.*, vol. 6, no. 4, pp. 423–443, 2019, doi: 10.1089/soro.2018.0136.

21) M. Tessler *et al.*, "Ultra-gentle soft robotic fingers induce minimal transcriptomic response in a fragile marine animal," *Curr. Biol.*, vol. 30, no. 4, pp. R157–R158, 2020, doi: 10.1016/j.cub.2020.01.032.

22) K. C. Galloway *et al.*, "Soft Robotic Grippers for Biological Sampling on Deep Reefs," *Soft Robot.*, vol. 3, no. 1, pp. 23–46, 2016, doi: 10.1089/soro.2015.0019.

23) J. Guo, J. H. Low, Y. R. Wong, and C. H. Yeow, "Design and evaluation of a Novel Hybrid soft surgical gripper for safe digital nerve manipulation," *Micromachines*, vol. 10, no. 3, pp. 1–16, 2019, doi: 10.3390/mi10030190.

24) J. Guo *et al.*, "Design and fabrication of a pneumatic soft robotic gripper for delicate surgical manipulation," *2017 IEEE Int. Conf. Mechatronics Autom. ICMA 2017*, pp. 1069–1074, 2017, doi: 10.1109/ICMA.2017.8015965.

25) O. M. Omisore, J. Xiong, H. Li, and L. Wang, "A Review on Flexible Robotic Systems for Minimally invasive surgery," *IEEE Trans. Syst. Man, Cybermetics Syst.*, pp. 1–14, 2020, doi: 10.1016/B978-1-56053-579-9.50016-0.

26) J. Paek, I. Cho, and J. Kim, "Microrobotic tentacles with spiral bending capability based on

shape-engineered elastomeric microtubes," *Scientific Reports*, vol. 5. pp. 1–12, 2015, doi: 10.1038/srep10768.

27) M. De Volder and D. Reynaerts, "Pneumatic and hydraulic microactuators: A review," *J. Micromechanics Microengineering*, vol. 20, no. 4, pp. 1–18, 2010, doi: 10.1088/0960-1317/20/4/043001.

28) S. B. Kordmahale, J. Do, K. A. Chang, and J. Kameoka, "Low Cost and Piezoelectric based Soft Wave Energy Harvester," *MRS Adv.*, vol. 4, no. 15, pp. 889–895, 2019, doi: 10.1557/adv.2018.675.

29) S. B. Kordmahale, J.Kameoka, "Smart Soft Actuation System," *Ann. Mater. Sci. Eng.*, vol. 2, no. c, pp. 2–3, 2015, doi: 10.1557/adv.2018.675.

30) Y. Sargolzaeiaval *et al.*, "Flexible thermoelectric generators for body heat harvesting – Enhanced device performance using high thermal conductivity elastomer encapsulation on liquid metal interconnects," *Appl. Energy*, vol. 262, no. January, p. 114370, 2020, doi: 10.1016/j.apenergy.2019.114370.

31) R. Xu *et al.*, "Designing Thin, Ultrastretchable Electronics with Stacked Circuits and Elastomeric Encapsulation Materials," *Adv. Funct. Mater.*, vol. 27, no. 4, pp. 1–12, 2017, doi: 10.1002/adfm.201604545.

32) C. Wei and X. Jing, "A comprehensive review on vibration energy harvesting : Modelling and realization," *Renew. Sustain. Energy Rev.*, vol. 74, no. February, pp. 1–18, 2017, doi: 10.1016/j.rser.2017.01.073.

33) A. Uihlein and D. Magagna, “Wave and tidal current energy – A review of the current state of research beyond technology,” *Renew. Sustain. Energy Rev.*, vol. 58, pp. 1070–1081, 2016, doi: 10.1016/j.rser.2015.12.284.

34) M. Lehmann, F. Karimpour, C. A. Goudey, P. T. Jacobson, and M. R. Alam, “Ocean wave energy in the United States: Current status and future perspectives,” *Renew. Sustain. Energy Rev.*, vol. 74, no. February 2016, pp. 1300–1313, 2017, doi: 10.1016/j.rser.2016.11.101.

35) S.Patricio, A.Moura, T.Simas, “Wave energy and Underwater noise: State of art and uncertainties”, OCEANS 2009-EUROPE, 11-14 May 2009; doi:10,.1109/OCEANSE.2009.5278302

36) T. Aderinto and H. Li, “Review on Power Performance and Efficiency of Wave Energy Converters,” *energies*, vol. 12, no. 22, 2019, doi: 10.3390/en12224329.

37) H. X. Zou *et al.*, “Mechanical modulations for enhancing energy harvesting: Principles, methods and applications,” *Appl. Energy*, vol. 255, no. February, p. 113871, 2019, doi: 10.1016/j.apenergy.2019.113871.

38) Z. L. Wang, T. Jiang, and L. Xu, “Toward the blue energy dream by triboelectric nanogenerator networks,” *Nano Energy*, vol. 39, no. June, pp. 9–23, 2017, doi: 10.1016/j.nanoen.2017.06.035.

39) T. Cabral *et al.*, “Performance assessment of a hybrid wave energy converter integrated into a harbor breakwater,” *Energies*, vol. 13, no. 1, pp. 1–22, 2020, doi: 10.3390/en13010236.

40) F. Gao, G. Liu, B. L. H. Chung, H. H. T. Chan, and W. H. Liao, “Macro fiber composite-based energy harvester for human knee,” *Appl. Phys. Lett.*, vol. 115, no. 3, pp. 1–5, 2019, doi: 10.1063/1.5098962.

CHAPTER II

SOFT MATERIALS AND DEVELEPEMENT OF SOFT ROBOTICS

2-1-Introduction

The evolution in robotics in the past several decades opened new opportunities in various fields like the fields of surgery, biological studies, and small object manipulation in the industry [1-6]. Minimally Invasive Surgery (MIS) is highly dependent on robotic technology to minimize patient trauma and improve clinical outcomes [7]. More clinical uptake of MIS needs more flexible robots to provide higher dexterity to the surgeon, minimize the blueprint, and delicate robot-tissue contact [7,8]. Also, Biological specimen collection and handling of delicate organisms in various environments, and with different sizes need to be performed successfully by using robotic manipulators [9]. Most of the commercially available manipulation systems with their rigid structures are not suitable to handle delicate tissues and specimens [9,10]. In the industry, precisely controlled grippers are essential and widely used to do tasks in various environments [11]. As the developed soft actuators in the industry became more precise their complexity also increases [7,12]. To introduce new robotic platforms to address the demands of the modern era, proper actuators and materials should be used to achieve the required specifications of the robotic platforms [13]. Shape memory alloys (SMA)[14], piezoelectric[15], Electrostatic MEMS[16], and hydraulic/pneumatic actuators[17] are among the widely used actuators to design better robots.

Piezoelectric ceramics and thin films have been used extensively to develop various actuators that are proper to use in robots and end effectors [18]. The precise control of the

movement of piezoelectric actuators, a high-power density, and a fast response time are the main benefits of piezoelectric actuators [19-21]. Using piezoceramics can lead to the development of various types of actuators, which still requires complicated micro-displacement transmission mechanism, and assembling miniaturized actuators is a difficult task [22]. The required high voltage driving signal for piezoelectric material actuation is another drawback of this family of actuators that can limit their applications in the fields of biomedical study and surgery [23]. SMA actuators use SMA wires or thin films as the actuating element. This simple mechanism can produce large force and stroke [24]. While various actuators can be developed by using SMA wires and thin films, assembling them is more challenging when the size of the devices shrinks [25]. The complexity of the required heating/colling systems alongside slow response are the drawbacks of the SMA actuators [26-27]. The proper thermal control and isolation are essential because it affects the force and position of the actuator [28-29]. The heating requirement for SMA elements of actuators can limit the application of these actuators to manipulate sensitive biospecimen and live tissues due to lateral thermal damage [30,31]. Electrostatic MEMS actuators are mainly based on the silicon processing [32]. The well-established fabrication process made this group of actuators an ideal and cost-effective actuator as 2D structures and a good candidate for miniaturization [32,33]. The challenges in proper packaging and isolation of MEMS actuators are the main drawbacks of this family of actuators [34]. All aforementioned actuators are developed based on hard materials. This feature is a drawback that makes a proper soft material encapsulation essential for these actuators for fragile sample manipulation, which will increase their complexities [35,36]. Hydraulic and pneumatic actuators and end effectors are another family of widely developed actuators [37]. The

complexity of these actuators is with miniaturization and assembling them when the actuator is in micro size [38]. They do not have some of the drawbacks of other actuators. They use tubing to energize the actuator that removes the risk of wiring, high voltage, and high-temperature damages to the live tissues [39]. One of the main benefits of this family of actuators is their compatibility with soft materials [40]. If a designer can overcome the assembling, miniaturization, and complex movement dynamic of hydraulic/pneumatic actuators, the desired robotic structure can be achieved.

Choosing the proper material to fabricate the new robotic platform and its robotic end effectors is an essential step for a designer [41]. Soft materials can be an alternative for hard polymers and metals, which using them allows robotic end effectors to mimic the properties of soft tissues and biological actuators[40,42]. This allows surgeons and researchers to delicately handle live tissues[43]. Biocompatible, elastomers are among good candidates for soft robotic applications.

After determining the required amount of force, working media, and the required method of transferring force to the specimens, the proper micromanipulator can be developed[44]. In this research, soft material casting was used to fabricate monolithic PDMS-based three finger-like columns on a deformable membrane to conform two different types of microhand-like manipulators. Additionally, a combination of a deformable membrane with 3D printed fingers was used to develop a hand-like device with a potential application in minimally invasive surgery(MIS). The bending characterization of these devices was performed successfully by using microsyringes and an optical microscope. The force production characterization for microhands was done using the AE-801 piezoresistive microforce sensor while a qualitative force

measurement was performed to characterize the bigger hand-like device. The finite-element method using ABAQUS 6.12 software was used to simulate the closing or opening of the micro hand based on the prescribed pressures. The Gent model is implemented within user material subroutines (UMAT) within ABAQUS finite element analysis. The simulation can be used as a design tool for future optimization and actuator designs prior to fabrication. To approve the ability of the developed microhand devices to manipulate fragile biospecimen, a live ant and a goat embryo were grabbed, held, and released successfully without any physical damage. A piece of chicken breast was used to mimic an internal organ and was grabbed and manipulated by using the hand-like device that was developed for MIS.

2-2-Monolithic Device Developing

2-2-1-Monolithic Device Design and Mechanism

The idea to achieve a 3D microhand-like structure in this research is to form a micro-scale gripper that its closing and opening can be adjusted by using pressure in a cavity. The main part of the designed hydraulic/pneumatic 3D microhand is created from a combination of a 150 μm PDMS-based membrane placed on the top of a cylindrical void and three columns, which are placed on the top of the membrane as fingers. The void, membrane, and three fingers form the monolithic gripper. There have been two different designs as it is depicted in figure 1. The design pictured in figure 1(a) is matched with microfluidic systems, while the one in figure 1(b) is designed to be used directly on the tip of a syringe.

As it is depicted in figure 2 the fingers are placed on a deformable membrane. By deforming the membrane's shape into being concave or convex, the three fingertips on the top

can cause opening or closing. Thus, the internal pressure of the cavity should be higher than the exterior's pressure to create convex membranes and lower for concave membranes. The deformation of the membrane can be calculated, either analytically or numerically, based on the amount of pressure. The deformation mechanism based on this pressure difference is independent of

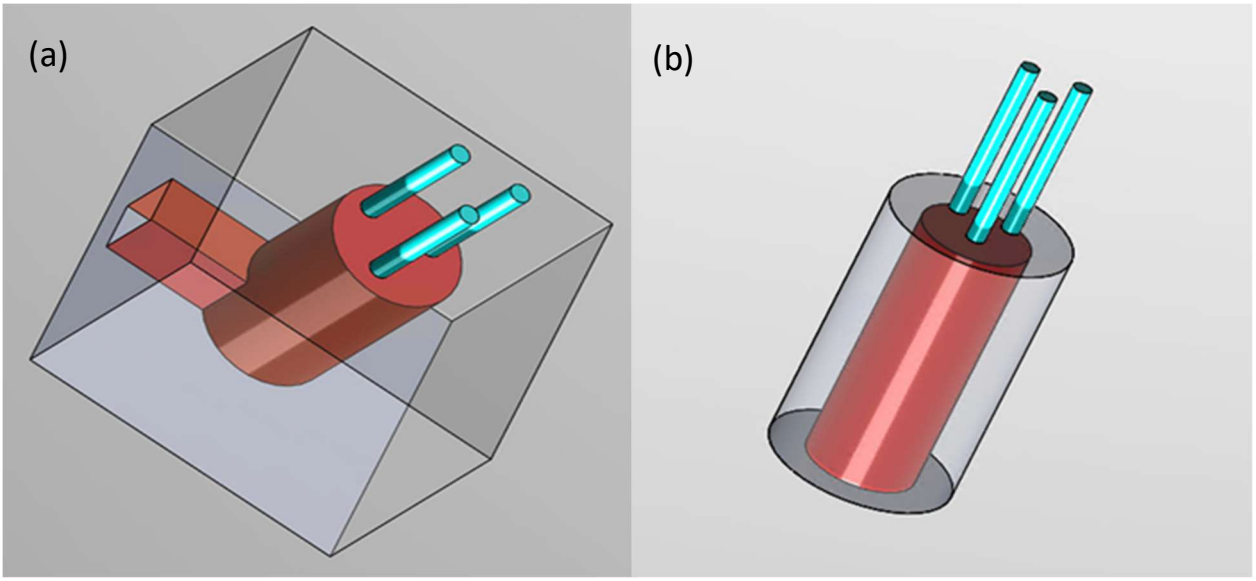

Figure 1. **The designed microhand grippers.** (a) Square shape device matched with microfluidics. The channel connected to the central void can be seen in this image. (b) The cylindrical device is designed to be placed on a syringe (requires an extra assembling step).

membrane geometries. An approximate for maximum displacement at the center of a circular membrane with the radius of $a=L_X/2$ is[45]:

$$W_0=(p(a)^4)/(64D_{flex}) \quad (2.1)$$

This equation can give a very good insight about the membrane deflection and show the effects of static force (p), dimensions and geometry (a) and material rigidity (D_{flex}). By changing the membrane thickness or material stiffness, it is possible to have devices with different functional features. In equation 2, the deflection at (r) can be calculated[45].

$$W(r)=[(p(a)^4)/(64D_{flex})](1-(r)^2/(a)^2) \quad (2.2)$$

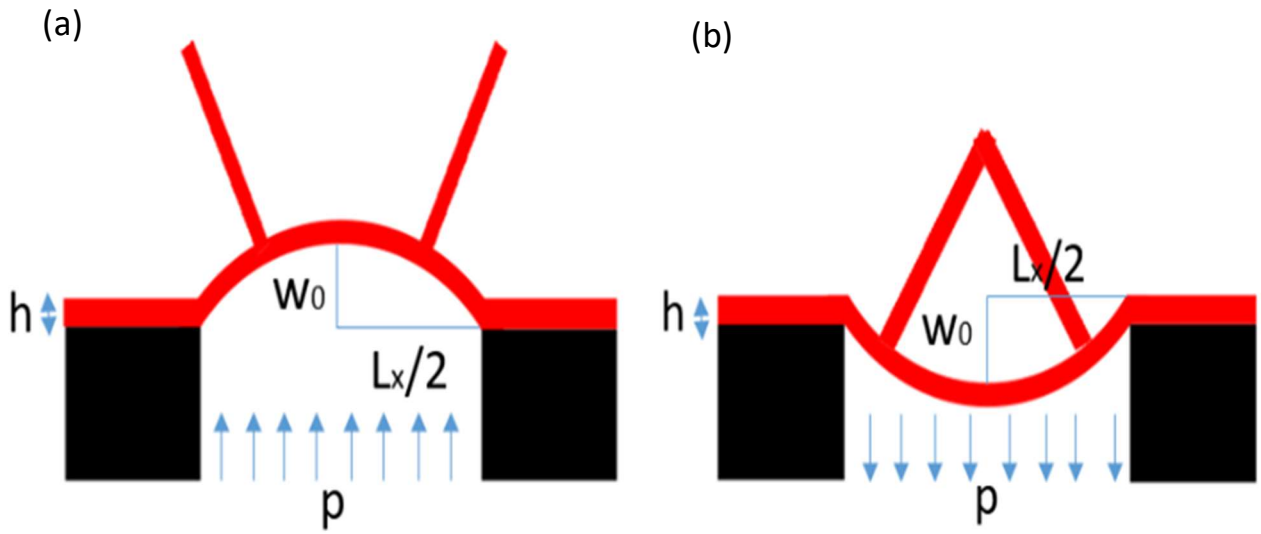

Figure 2. **The fingers are placed on the membrane and the opening/closing mechanism.** (a) opening the fingers. (b) closing the fingers.

2-2-2-Fabrication

The micro-hand structure is fabricated from polydimethylsiloxane (PDMS) through soft material molding [46,47]. The required molds for this process were fabricated using a stereolithography 3D printer. The 3D printing was done using a Perfactory Micro 3D printer developed by EnvisionTEC. The HTM 140 V2 M photopolymer, made and distributed by

EnvisionTEC was used as the liquid photopolymer in the Perfactory Micro 3D printer. This photopolymer is usually used for printing devices with small feature sizes like small holes and small grooves. After finishing the 3D printing, all the residue liquid photopolymer must be washed away carefully. The washing process should be done using IPA as the solvent. Sonication in the IPA may be essential when the mold contains deep holes and grooves. In figure 3, the photo image of the Perfactory Micro 3D printer can be seen. A photo image of the bottle of liquid photopolymer, the photopolymer itself in the 3D printer's tray, and the empty tray are shown in figure 4. To finalize the fabrication of 3D printed molds, they were exposed to light curing, thermal curing for 72 hours at 65°C in the oven, and the silane gas as the surface treatment, respectively. Siliconization can make the surface more hydrophobic through the inclusion of silane gas[48,49]. The method for this is detailed in APPENDIX B. The two parts of the 3D printed molds are illustrated in figure 5. In figure 5(a,b) the molds for the cylindrical device are displayed, while in figure 5(c,d) the molds for the square shape device are shown. For both kinds of devices, the first part of molds (shown in 5 (a,c)) were designed with three holes to form the three fingers, while the second part of molds (shown in 5.b,d) was responsible to form the central void as cavity and the membrane where the fingers are placed on. The two parts of molds for each device form an encapsulated closed volume. The 3D printed molds and their parts are shown in figure 6. In figure 6(a,b) the molds for cylindrical microhand are shown, while in figure 6(c,d) the molds for square-shaped microhand are illustrated. In figure 7, a photo image of the formation of the 3D printed holes is shown. Because the holes have 300 μm diameter and 1.5-2 mm of depth, their fabrication is difficult and needs process optimization. To achieve this structure the exposure time was optimized several times to reach the proper exposure time for each layer of 3D printing.

Just with this optimized exposure time, it was possible to form the holes. Longer exposure times were led to a total hole blockade, while shorter exposures not forming any structure. For PDMS the polymer and initiator were mixed with the (10:1) ratio to achieve a very soft and deformable material. The curing of PDMS was executed in one week at 25°C. The combination of the hydrophobic surface of the molds and a very flexible soft material made it possible to remove the cured PDMS from the molds.

Figure.3**.** Perfactory Micro 3D Printer developed by EnvisionTEC**.**

Figure.4. **Photopolymer and how it looks like.** (a) A bottle of HTM 140 V2 M photopolymer (b) The empty tray of 3D printer. (c) The tray contains a green HTM 140 V2 M photopolymer.

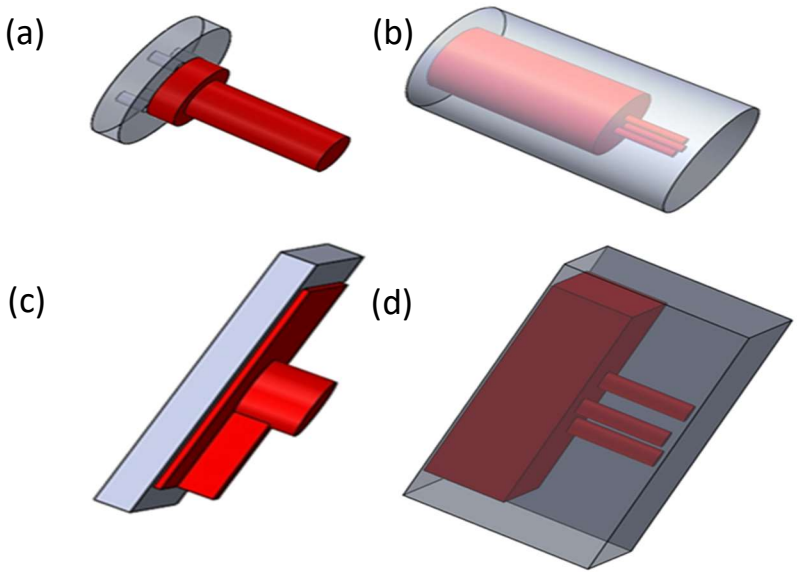

Figure. 5. **The schematic model for 3D Printed Molds.** (a,b) The mold cap and mold for cylindrical microhand. (c,d) The mold cap and mold for square shape device.

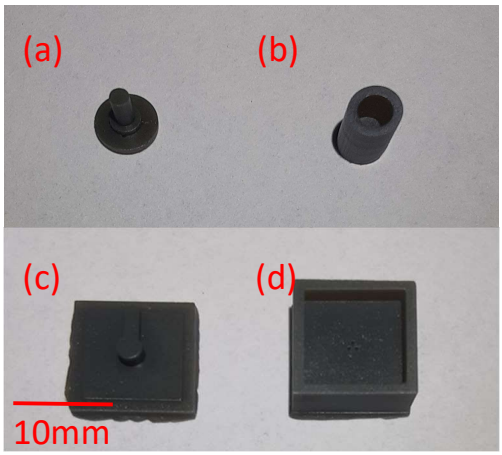

Figure.6. **3D printed molds.** (a,b) The 3D printed molds for cylindrical device (c,d) 3D printed mold for the square-shaped device.

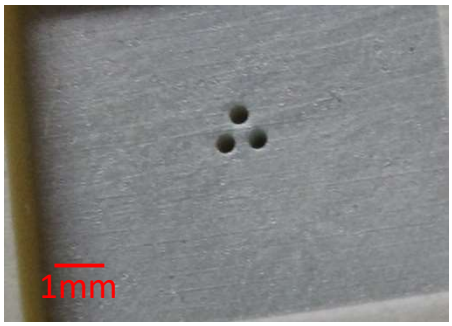

Figure. 7. **Photo image of 3D Printed Holes**. The 3D printed holes with the diameter of 300 µm and 600 µm center-to-center distance. The holes have the same diameter for cylindrical and square-shaped microhands. While the depth is 1.5 mm for the square-shaped device, it is 2mm for a cylindrical one.

The fabrication steps for the microhand are pictured in figure 8. To form the devices, the mixed liquid PDMS was poured into the first part of the molds, which contain three holes. The second part of the molds was covered by liquid PDMS(figure 8 (a,b)). Then they were placed in a vacuum to remove all the bubbles from the liquid. The two parts of the molds were closed (figure

8(c)), and the whole structure was immersed in liquid PDMS(figure 8(d)). Finally, the container of liquid PDMS that contains the molds with encapsulated liquid PDMS inside of them was placed in the vacuum to remove all the residual entrapped bubbles. After leaving the molds for one week at room temperature (25°C), the two pieces opened, and the cured PDMS was removed slowly (fig 8.e). Because the cured PDMS was very soft with 1MPa young modulus, it was possible to remove it from the molds without damages. The SEM image of the fabricated three-fingered microhand is illustrated in figure 9. The steps for mold casting of PDMS are described in APPENDIX A.

The final step of the fabrication was to assemble the microhand's parts and finalize the device. For the square shape device, the previously fabricated structure was bonded on a plate of cured PDMS by using oxygen plasma treatment and water as the bonding liquid[48,49]. When the water evaporated eventually, the strong hermetic bond formed between two pieces of cured PDMS, and the whole cavity and device formed successfully. For the cylindrical structure, a special connector was designed, and 3D printed that was matched with the standard syringe tips, and the cured PDMS-based microhand was attached to the 3D printed piece to finalize the device. The parts and finalized devices are shown in figure 10.

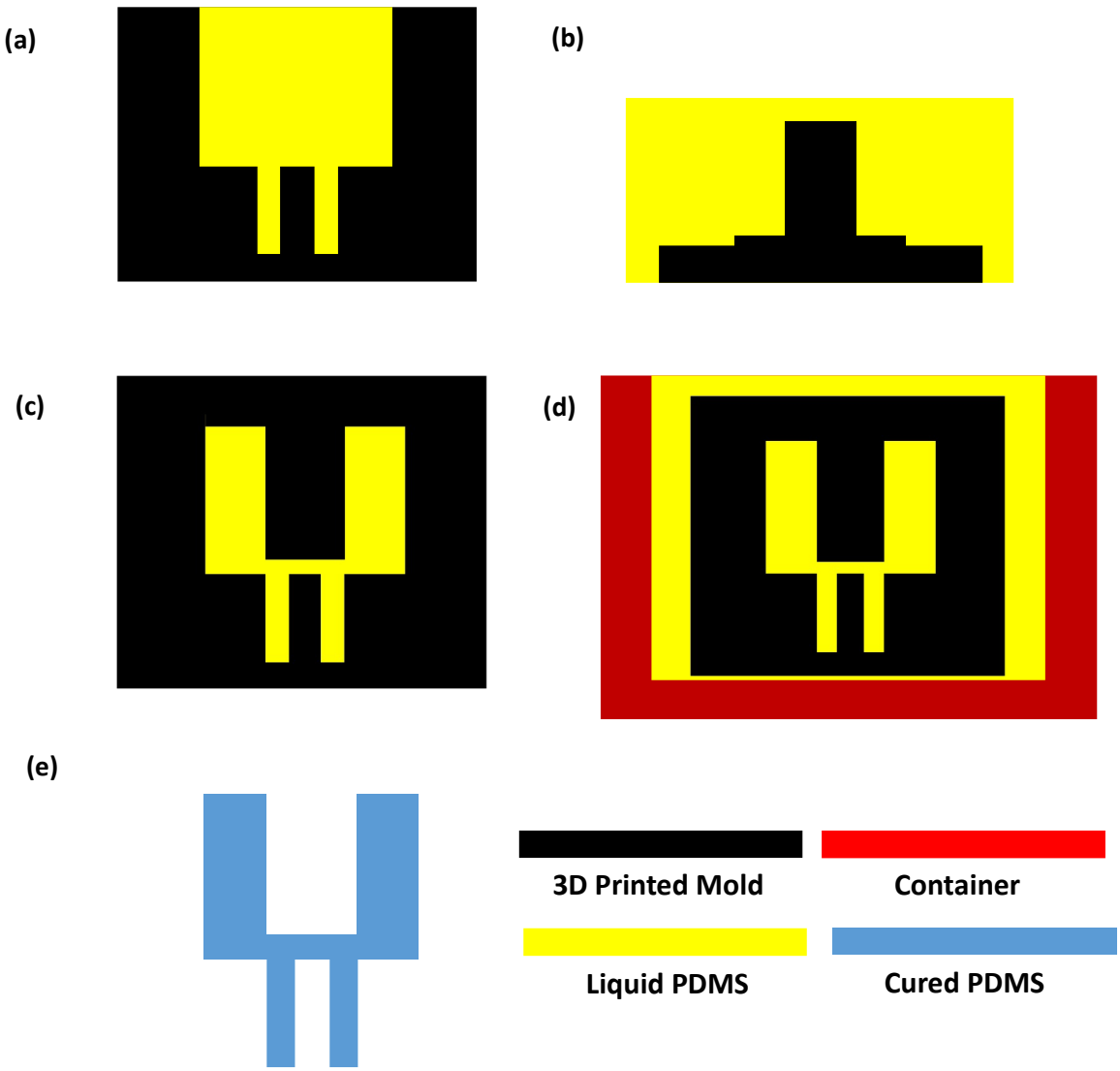

Figure.8. **Microhand Fabrication Steps. (**a,b) The 3D printed mold was filled with liquid and debubbled PDMS, and the mold cap was covered with the same PDMS. (c) Closing the mold and the mold cap. The liquid and debubbled PDMS were encapsulated in the 3D printed parts. (d) Immerse the 3D printed parts into the liquid, debubbled PDMS. The whole container should be placed in the vacuum and debubbled again. The unwanted bubbles that were trapped in the mold during the process can be removed in this step. (e) PDMS was cured at 25°C in one week. The cured PDMS should be removed from the 3D printed molds. The functional part of the microhand device was formed.

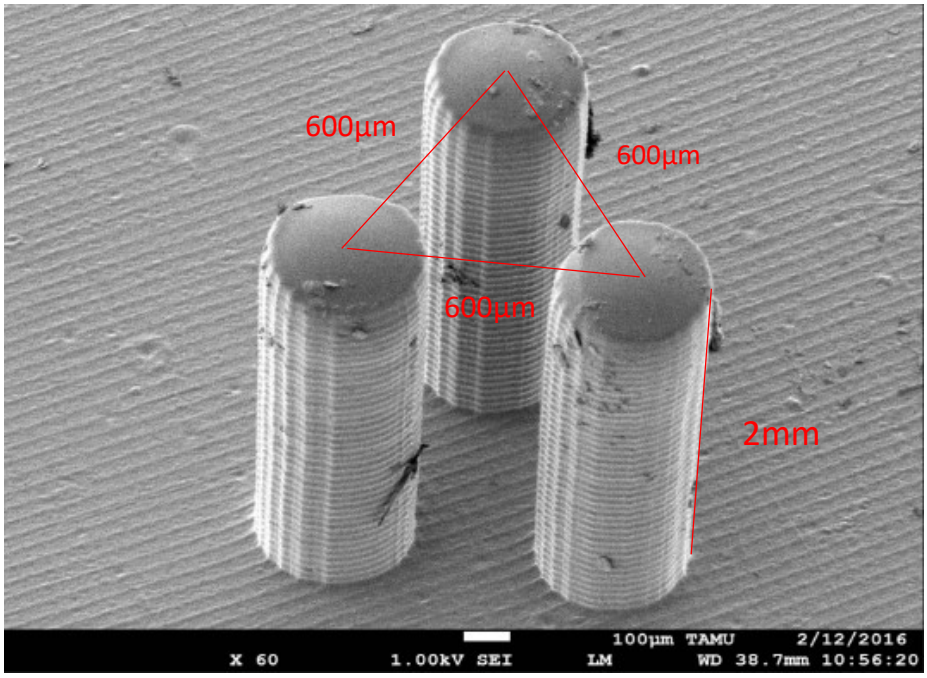

Figure.9.**SEM image of three fingers.** The diameter of each finger is 300µm and the center-to-center distance between each two fingers is 600µm. The Triangle in the image shows the center-to-center distances between fingers.

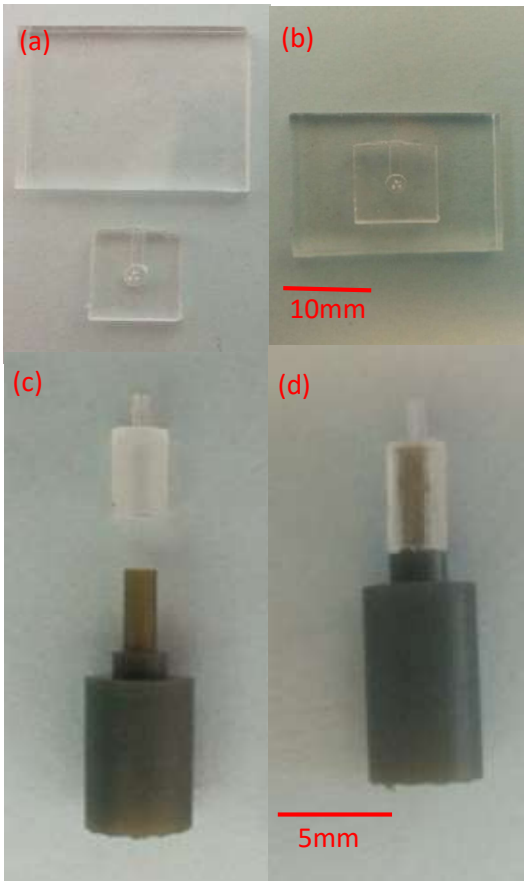

Figure.10. **Assembling and finalizing the microhands.** (a) Square-shape microhand's elements (b) Finalized Square-shape microhand. (c) Cylindrical microhand's elements. (d) Finalized cylindrical microhand.

2-2-3-Characterization

2-2-3-1-Deflection Characterization

The deflection characterization of microhands was done using precise microliter syringes under an optical microscope. A Nikon microscope was used to perform characterization. To characterize the amount of deflection, the samples of micro-hand were placed under the Nikon microscope. In figure 11 the Microscope and the placement of a microhand over it are illustrated. The deflection-volume graphs were obtained by changing the injected water volume into the

microhand's cavity. This injected water volume was precisely controlled by using accurate and precise microlitter syringes fabricated by Hamilton. A Photo Image of the microliter syringes is shown in figure 12. The deflection measurements were performed on optical images by using the software of Nikon Microscope. The side view of the fingers and the measured angle in a deflected one are depicted in figures 13(a,b).

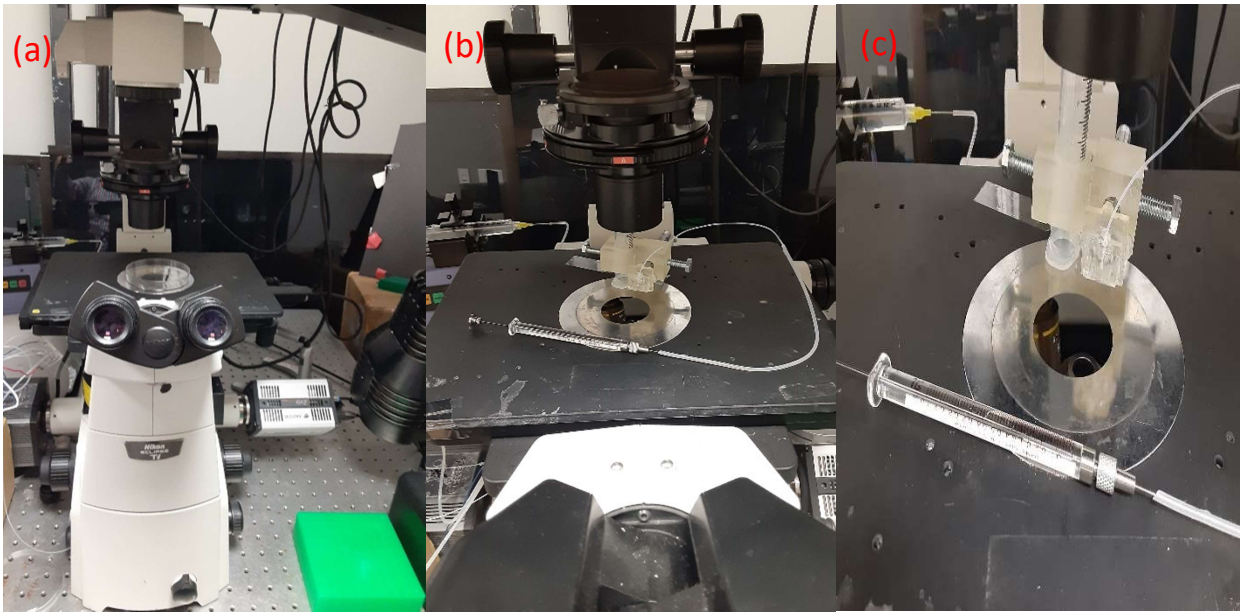

Figure.11. **Nikon microscope and microhand placement over it.** (a) Nikon metallurgical microscope. The camera can be seen (b) The holder of microhand, the tube, and the microliter syringe can be seen. (c) Placement of the microhand over the objective lens.

Figure. 12. **Microliter syringes.** Microliter syringes that were used to characterize microhands are shown in this image. The microliter syringes are developed by Hamilton. The volume of syringes are 50 µl, 5 µl, 2 µl, and 1 µl from top to bottom in the image.

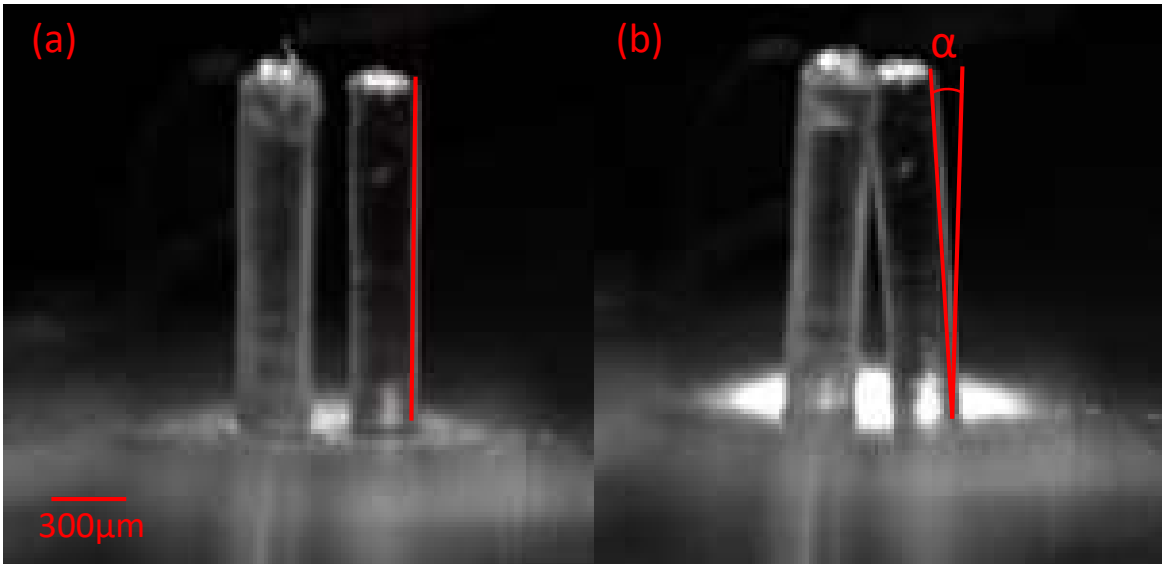

Figure.13. **The side view of the device and the side view of the device with bending fingers**. **(**a) The side view of the microhand's fingers. (b) The side view of the bending finger and the measured angle of bending(α).

The bending-volume experimental measurements for the square-shaped devices are shown in figure 14. The bending-volume experimental measurements for the cylindrical-shaped devices are depicted in figures 15 and 16. While figure 15 contains the values for both opening and closing regimes, figure 16 only contains the data of the opening regime on a broader range of injected volume changes.

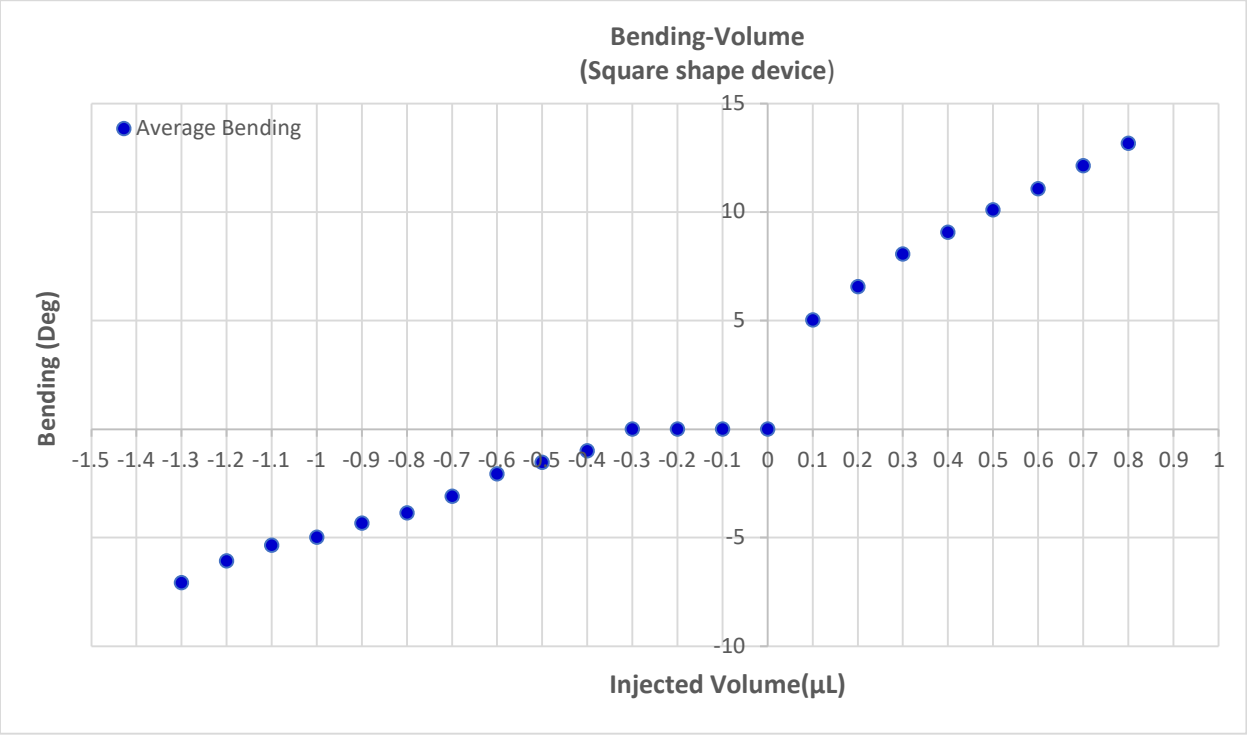

Figure.14. **The square-shaped device bending characterization**. The bending of the finger is measured under an optical microscope. The angle (α) changes are shown versus the change of injected volume of water in the cavity.

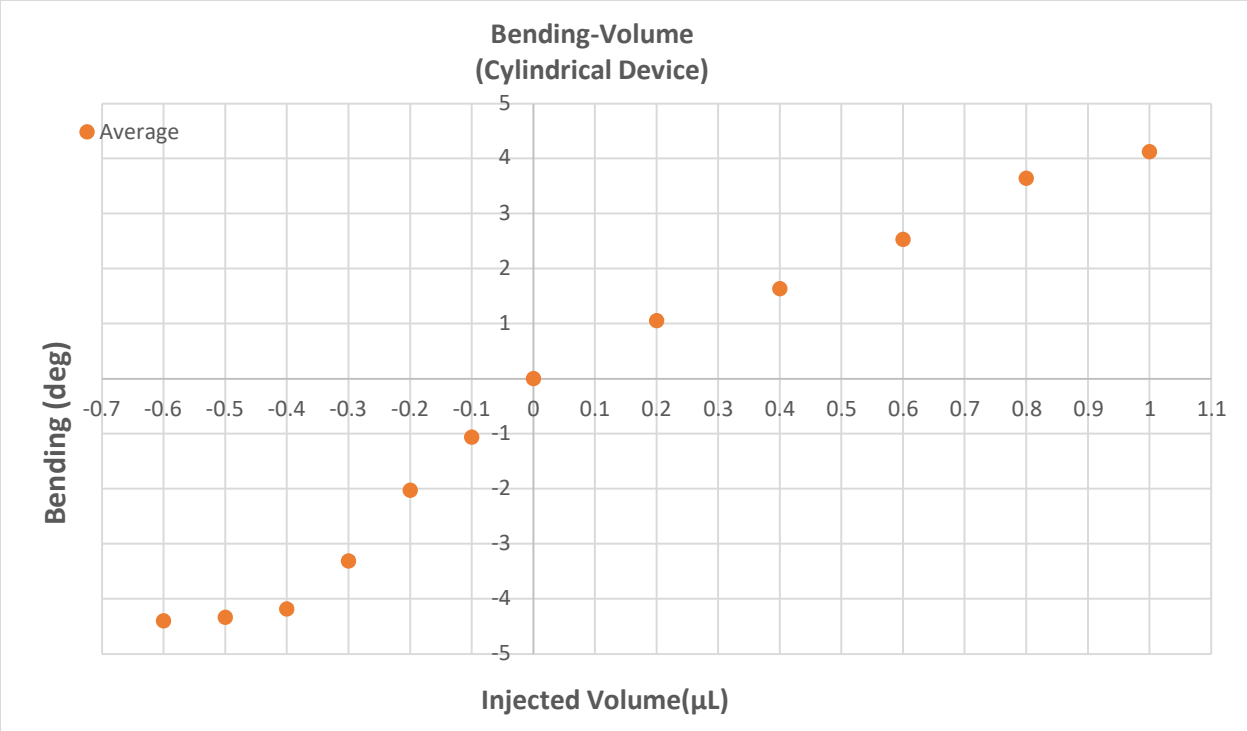

Figure.15. **The cylindrical-shaped device bending characterization**. The bending of the finger was measured under an optical microscope. The angle (α) changes are shown versus the changes of injected volume of water in the cavity.

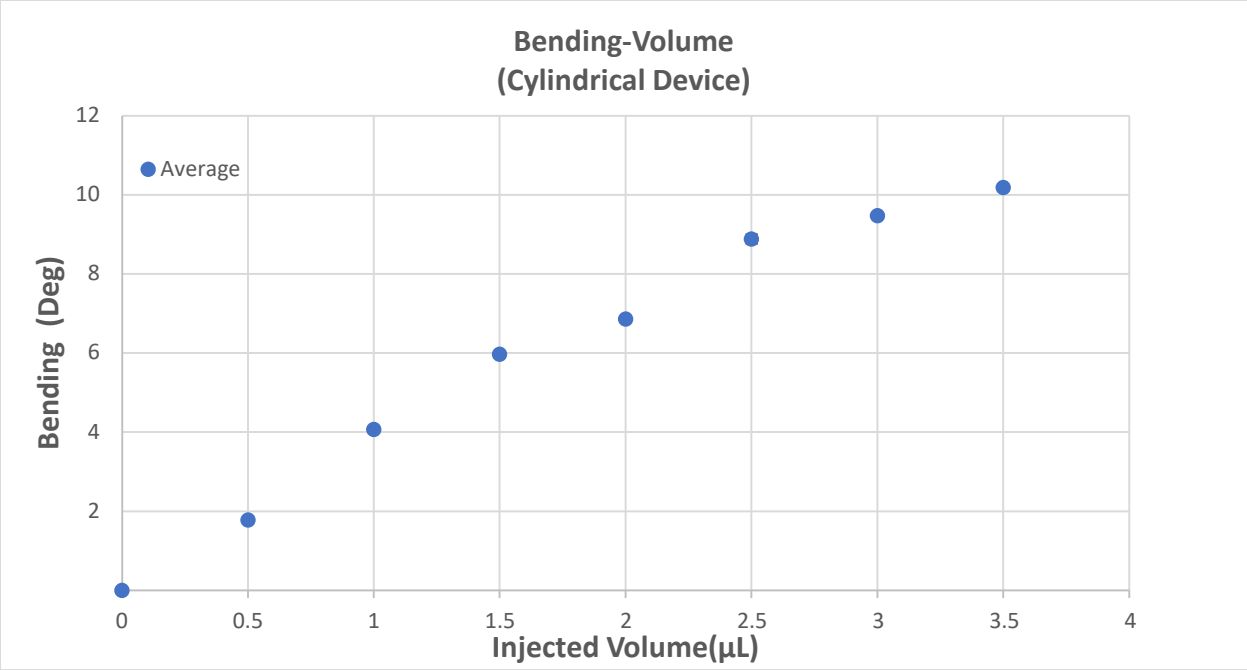

Figure.16. **The cylindrical-shaped device bending characterization in just opening regime**. The bending of the finger was measured under an optical microscope. The angle (α) changes are shown versus the change of the injected volume of water in the cavity just for the opening regime.

2-2-3-2-Force Characterization

To measure the produced forces of the two types of microhands, the AE-801, developed by Kronex, microforce sensor was used successfully. This cantilever-like microforce sensor works based on a piezoresistive mechanism that is fabricated as an implanted resistor on silicon. AE-801 is an easy-to-use and general-purpose sensor that can be used to measure the mechanical properties of materials and tools. The precision of this sensor is proved after many years of application in various fields. Figure 17 shows an AE-801 sensor, and the implanted resistor is shown on the cantilever in this figure. For effective measurement to avoid any unwanted misplacement during the force measurement, the sensor and the microhand were placed under

a Nikon stereoscope. The whole force measurement setup is shown in figure 18. To ensure the proper measurement, the gap between the microhand's finger and the sensor's cantilever should be zero. Also, the overlap between the finger and the cantilever should be adjusted precisely to a specific 300 μm and should be the same for all the experiments. In figure 19, the optical images of the microhand's finger and the sensor's cantilever can be seen.

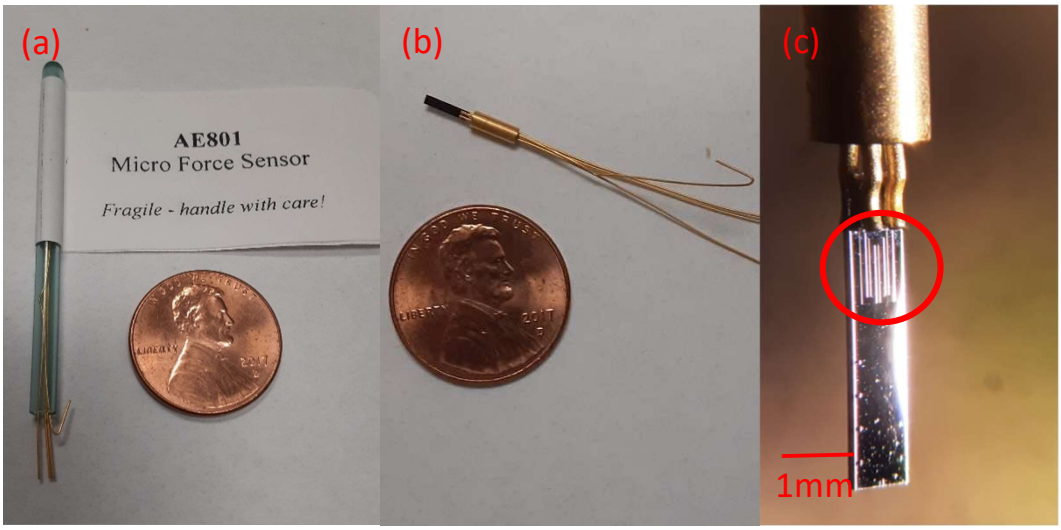

Figure.17. **AE-801 microforce sensor.** (a) the sensor in the package(b) the cantilever of the sensor, and its wires for connection to the circuit (c) The silicon cantilever of the microforce sensor bonded to the metallic connectors can be seen. The implanted resistor on one side of the cantilever is shown inside the red circle. At the other side of the cantilever is also another same resistor.

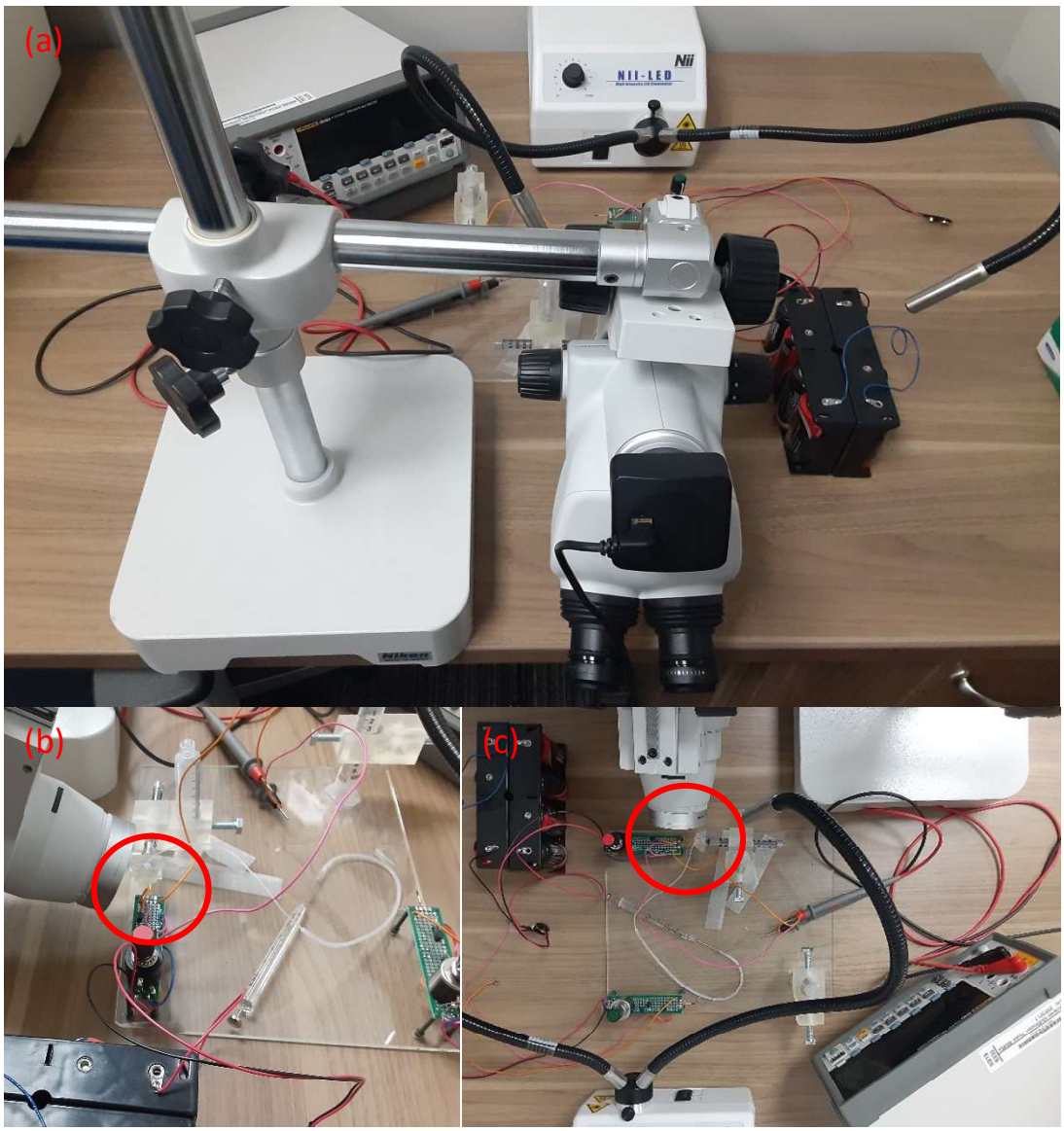

Figure.18. **Force measurement setup.** (a) The whole setup of force measurement. The Nikon stereoscope, the voltmeter, the light source, and batteries empower the measurement sensor and its related circuit. (b) Tilted placement of the stereoscope can be seen. The location of the sensor and the microhand is inside the red circle. The syringe and the tube can be seen in this photo. (c) The PCB of the sensor, the sensor, the microhand, the stereoscope, the syringe, the tube, and the voltmeter can be seen. The sensor and the microhand are in the red circle.

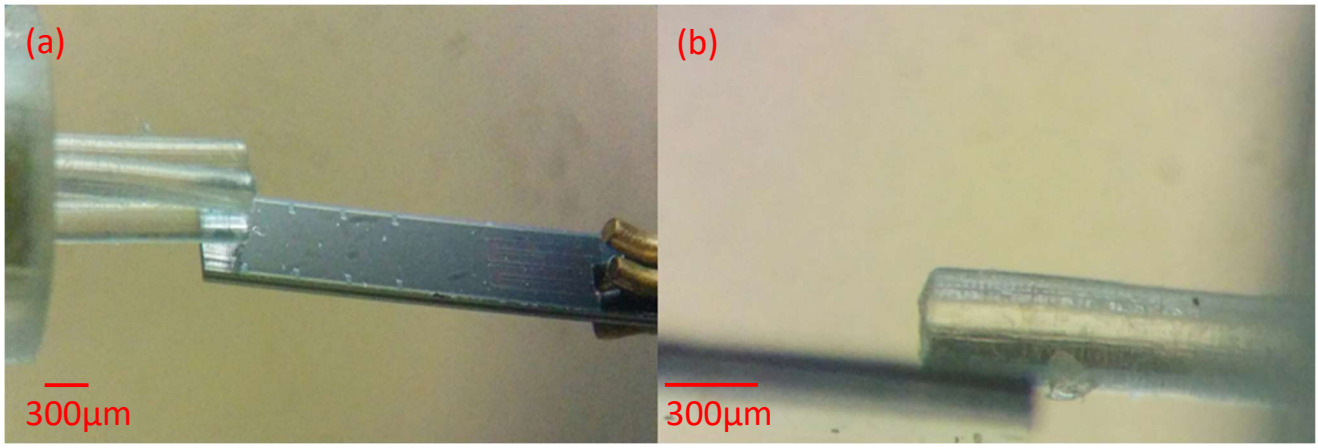

Figure.19. **Force measurement by using the AE-800 sensor**. (a) An optical image of the microhand and the force sensor. The suggested placement of the microhand and the sensor. (b) The side view of a finger and the cantilever of the sensor.

It is shown in figure 19 that the gap between the microforce sensor and the microhand's finger is adjusted to be zero. The overlap between the finger and cantilever is 300 µm.

It can be seen in figure 18 that the AE-801 sensor is placed on a PCB and is connected to the driving circuit. The schematic circuit diagram of the circuit for driving the sensor is shown in figure 20. As it is shown in figure 20, the circuit is a Wheatstone bridge. A photo image of the circuit is shown in figure 21. The reason to use batteries as the power supply for this sensor is to eliminate the chance of the power supply's noise influence on the force measurements. The measurements were done by using an accurate voltmeter. The output signal as voltage translated to the force through analytical calculations. All the required equations were provided in the datasheet of AE-801 by Kronex.

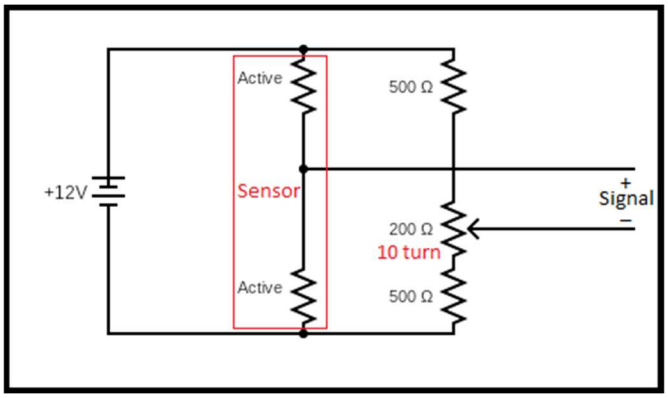

Figure.20. **Circuit diagram of the Wheatstone bridge**. The schematic circuit diagram for driving AE-801 sensor. The circuit is working based on a Wheatstone bridge.

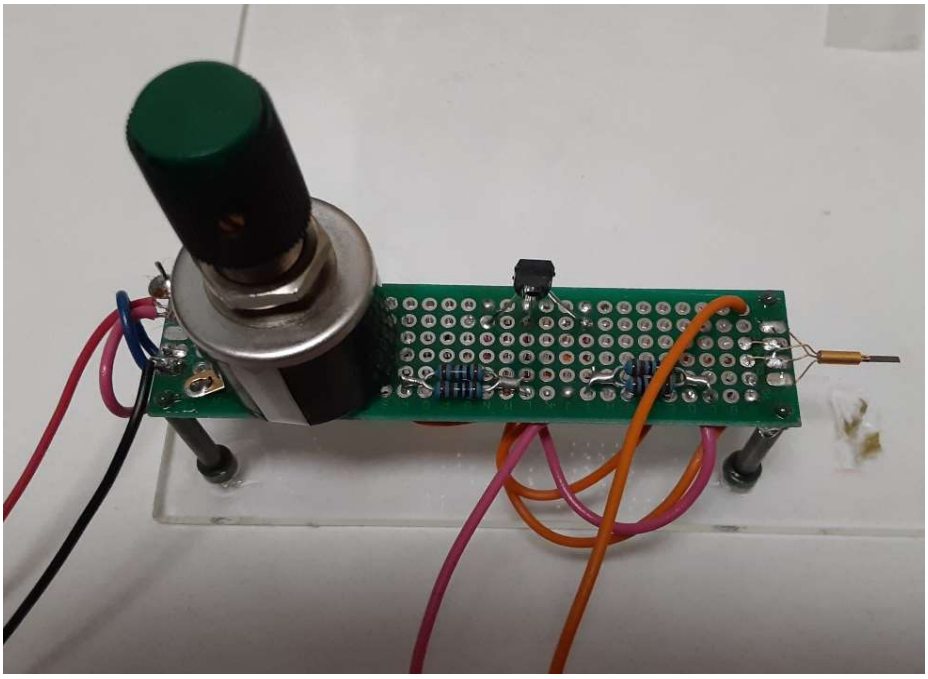

Figure. 21. **Photo Image of the circuit.** The photo image of the circuit is shown here. The sensor can be seen at the right side of the image at the edge of the PCB.

The force-volume measurements for the square-shaped devices, which is microfluidics compatible, are shown in figure 22.

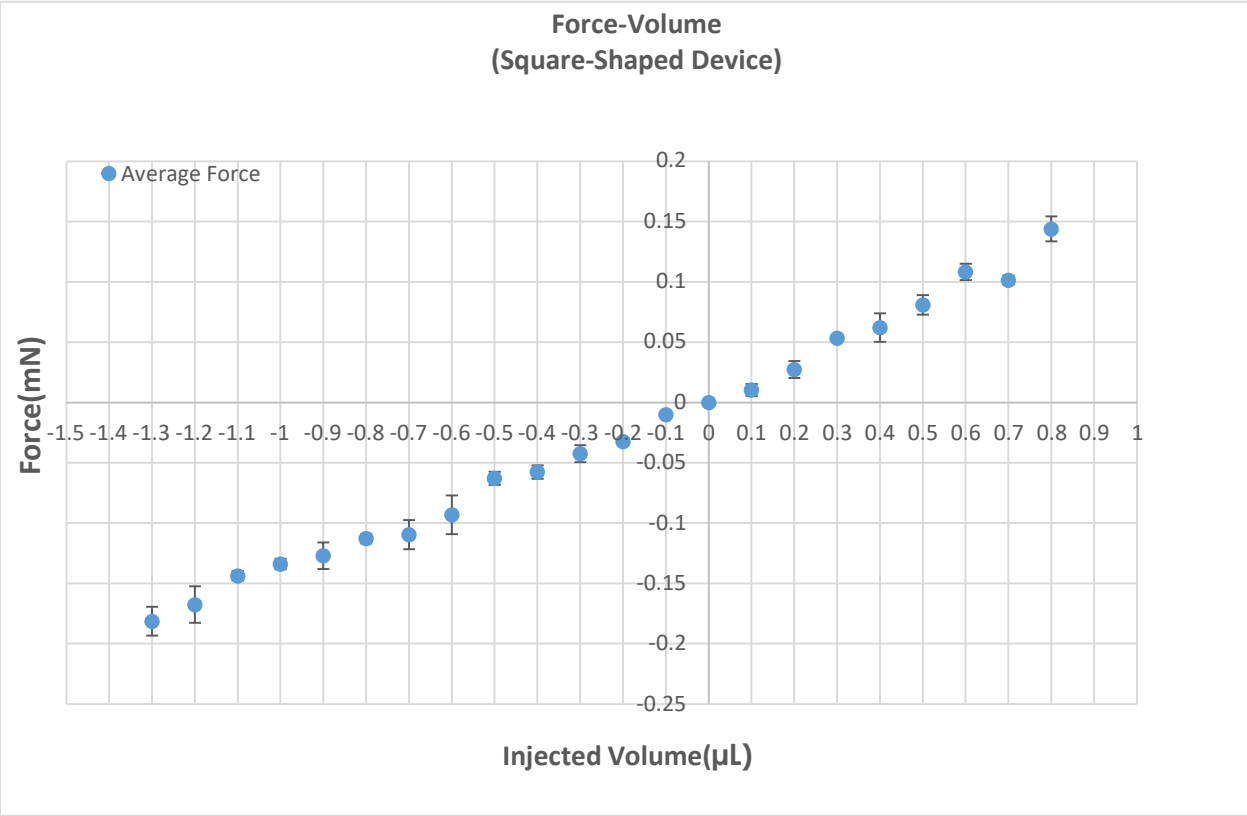

Figure.22. **The square-shaped device force characterization**. The force produced by one finger of the square-shaped microhand is measured under an optical microscope by using an AE-800 piezoresistive force sensor. The produced force changes are shown versus the changes of injected volume of water in the cavity. The negative forces are representing the produced forces during the closing regime.

The force-volume measurements for the cylindrical-shaped devices are depicted in figures 23 and 24. While figure 23, contains the force values in both opening and closing regimes, figure 24 just contains the data for the opening regime on a broader range of volume changes.

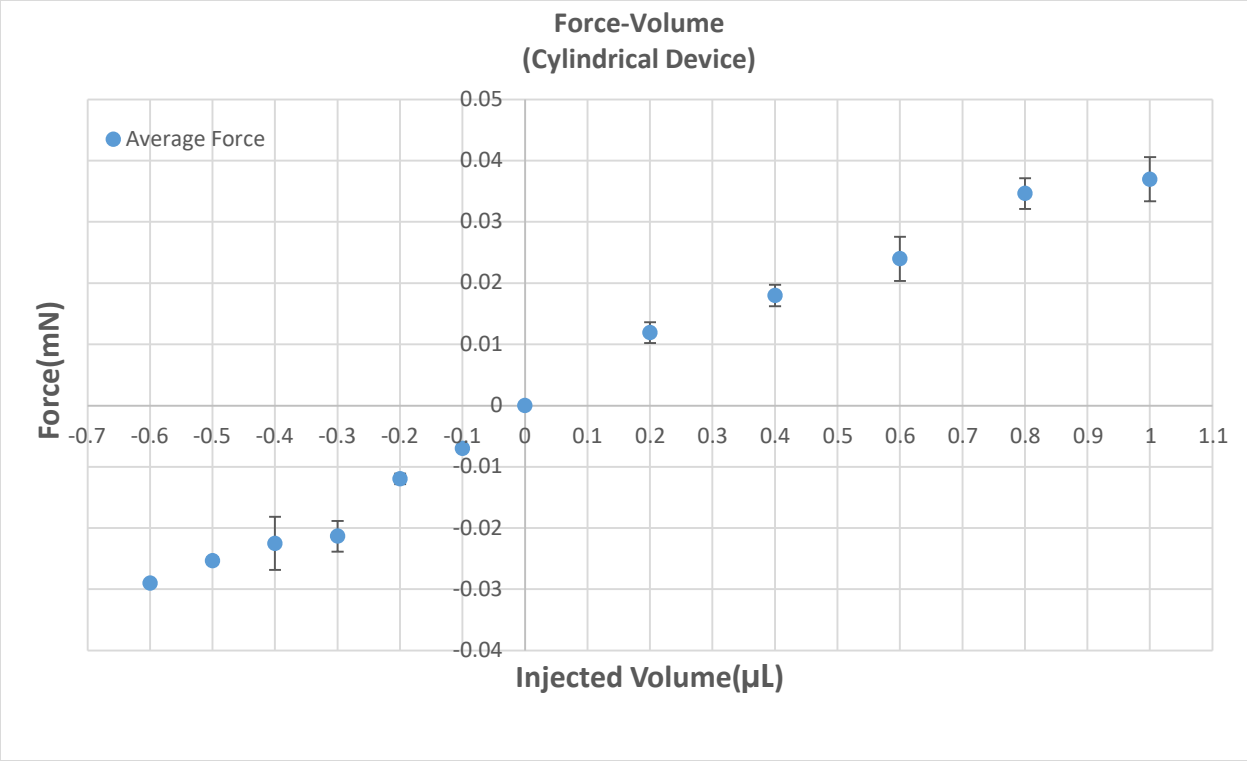

Figure.23. **The cylindrical-shaped device force characterization**. The force produced by one finger of the cylindrical-shaped microhand is measured under an optical microscope by using an AE-800 piezoresistive sensor. The produced force changes are shown versus the changes of injected volume of water in the cavity. The negative forces are representing the produced force during the closing regime.

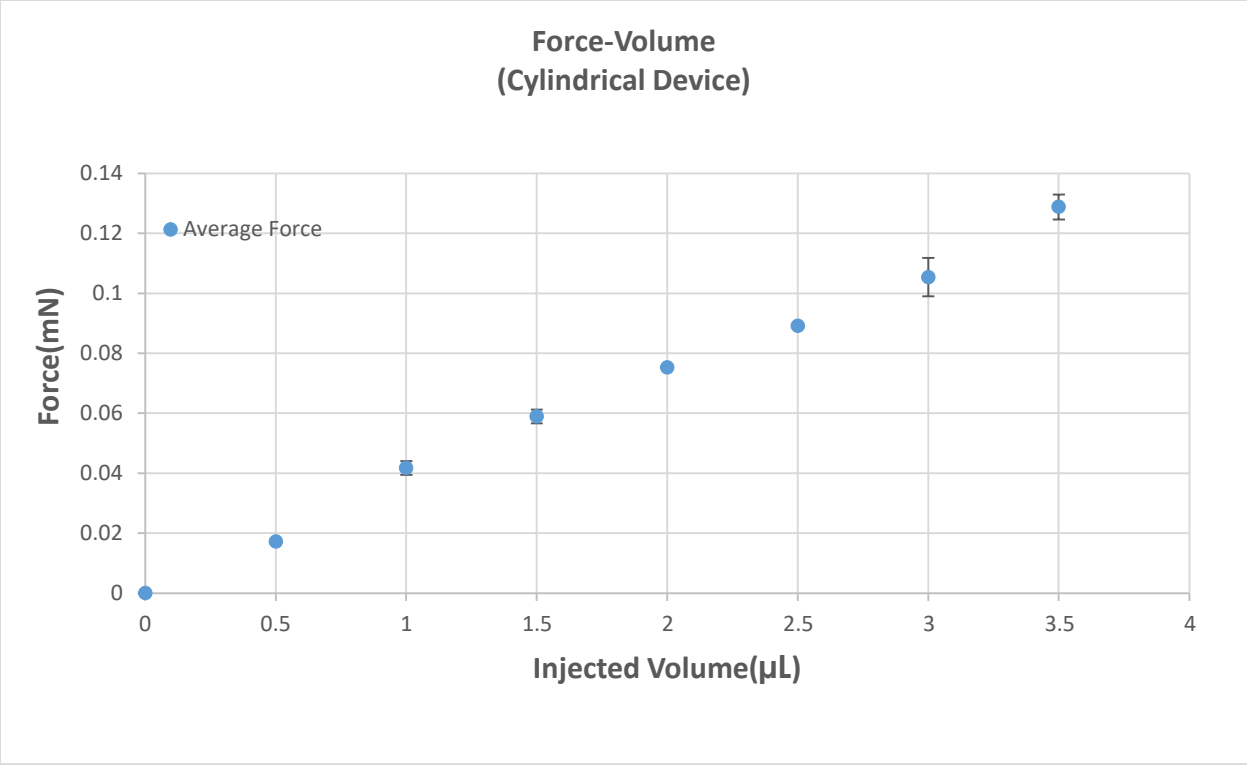

Figure.24. **The cylindrical-shaped device force characterization in just opening regime.** The force produced by one finger of the cylindrical-shaped microhand is measured under an optical microscope by using an AE-800 piezoresistive sensor. The produced force changes are shown versus the changes of injected volume of water in the cavity.

2-2-4-Simulation and Modelling

finite-element software ABAQUS 6.12 was utilized to build a 3D model for simulating the hydraulic actuation of microhand devices. A slightly compressible Gent hyperelastic free energy, having two parameters empirical constitutive model, was used for the hyperelastic volumetric and isochoric isotropic terms of the isotropic part of the constitutive model. The advantage of the model is to capture strain-stiffing at large strains, which are experimentally observed in soft materials. The volumetric and deviatoric parts of the constitutive equation for the finite element

implementation were separated to avoid numerical problems such as element locking. $W_V(J)$ denotes a purely volumetric and $W_D(\overline{I_1})$ represents its deviatoric contribution represented by the slightly compressible Gent hyperelastic model given by,

$$W_D(\overline{I_1}) = -\frac{\mu J_m}{2}\ln\left(\frac{J_m - \overline{I_1} + 3}{J_m}\right),$$

$$W_V(J) = -\frac{K}{2}\ln(J) + \frac{K}{2}\frac{J^2 - 1}{2}. \quad (2.3)$$

μ is the shear modulus, $J_m$is material constant, and $K$is the bulk modulus. The uniaxial experimental data was fitted, and the material properties were $\mu = 0.4MPa$, $J_m = 5.5$ and $\mathrm{K} = 2000$.

The model used 376,938 tetrahedral elements and was consisted of 10-node modified hybrid tetrahedral elements (ABAQUS C3D10MH). Modified tetrahedral elements provided a good convergence rate and prevented volumetric locking. Hyperelastic material models were highly capable of describing the nonlinear response of complex materials.

The deformation results from simulations are shown in figure 25. The displacement of the bottom surface of the model was constrained since the model was bonded horizontally on a plate of PDMS. Applied hydraulic pressures were set as pressure load which acts in the normal direction on the hydraulic channel. General surface-to-surface contacts were set up for the three fingers of the models in figure 25.

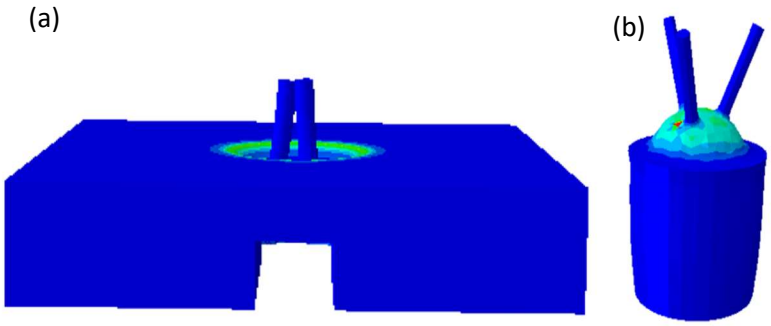

Figure 25. **3D model and simulation results.** a) simulation of deformation of the fingers in the closing regime, in a square-shaped device b) simulation of deformation of the fingers in the opening regime, in a cylindrical-shaped device.

While the material parameters were obtained from the uniaxial experiment, other parameters of the microhand-like dimensions of the fingers and membrane came from the developed devices. The comparison results of the simulation and experimental measurements are depicted in figures 26 and 27. As it is obvious from these graphs the simulation and experimental results are in very good agreement, which means the 3D model is appropriately developed. The code is provided in APPENDIX C.

Further development of this simulation can provide a powerful tool for the design and optimization of the parameters of required microhands in the future.

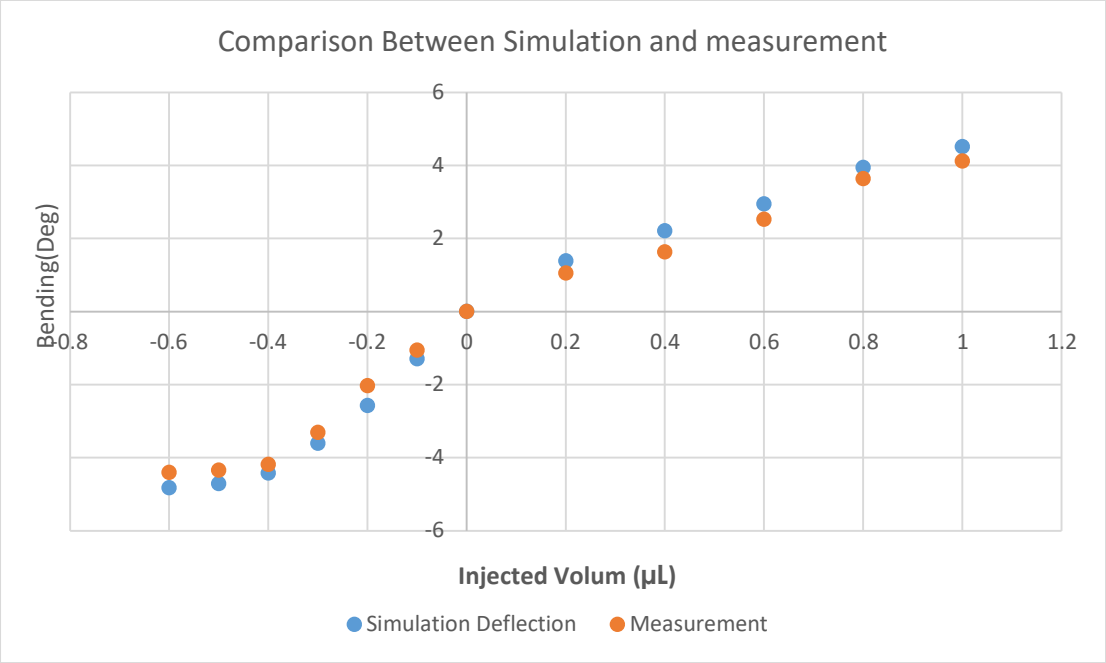

Figure.26. **Comparison of the simulation and experimental measurement.** The comparison between simulation and measurement for the square-shaped device in opening and closing regimes. The simulation and experimental measurement show almost the same slope as depicted in the figure.

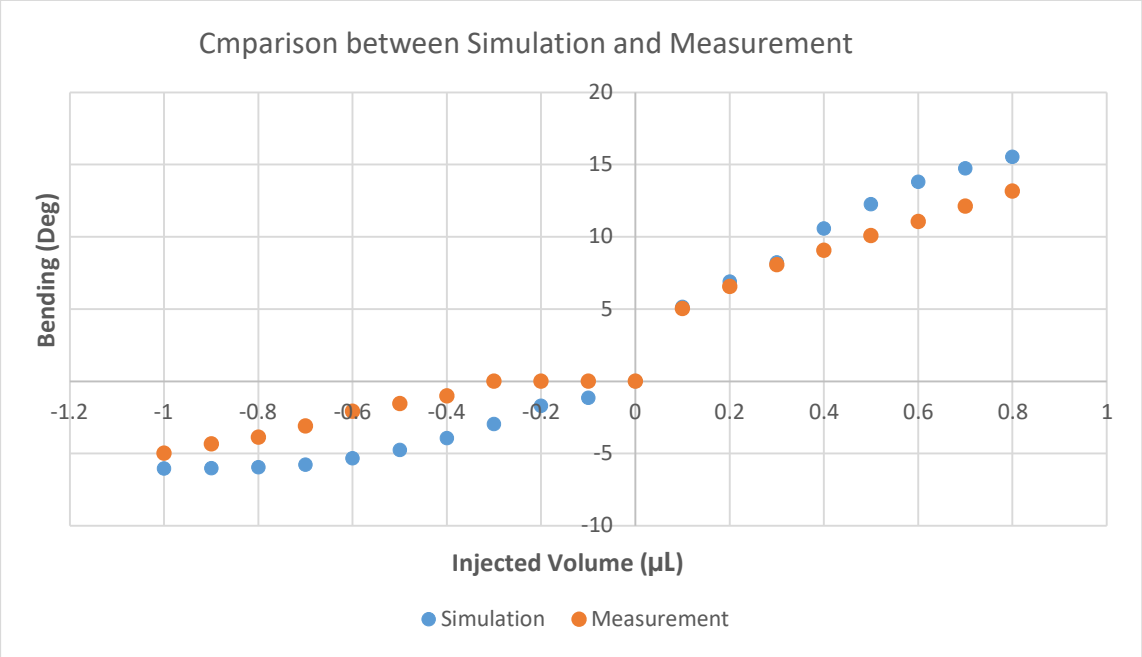

Figure.27. **Comparison of the simulation and experimental measurement.** The comparison between simulation and measurement for the cylindrical-shaped device in opening and closing regimes. The simulation and measurement show almost the same slope as depicted in the figure.

2-2-5-Biospecimen manipulation

To prove the hypothesis that these microhands can hold and manipulate a biological fragile sample precisely, the manipulation of an ant was performed under a microscope. The microhand was able to grab, hold, and release a live ant without physically damaging it. So, by adjusting the pressure and the finger location, the manipulating of the fragile specimen was performed successfully. The manipulation of an ant is shown in figure 28.

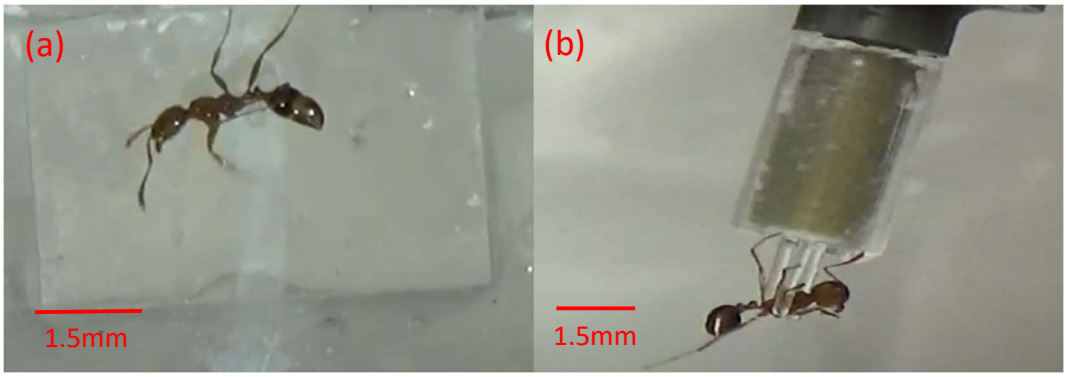

Figure.28. **Manipulation of a live insect. (**a) Successful handling of a live ant by using a square-shaped device. (b) Successful handling of the same live ant with a cylindrical-shaped device.

For this purpose, the ant was placed on an ice pack and halted due to low temperature. This made it easier to grab the insect. The grabbing of the biospecimen was performed under a Nikon Stereoscope. After grabbing the ant, it was separated from the ice pack in the way it warmed up and started to move again. After 1 minute of holding the moving insect, it was released, and no injuries were observed. The grabbing and manipulation of the ant were performed with both kinds of devices that were developed and reported in this article.

To show the ability of the developed microhands to grab fragile biospecimen in the aqueous medium, an embryo of a goat was successfully manipulated in water. For this purpose, a special holder was designed and fabricated by using a Form-2 3D printer developed by Formlabs. The square-shaped microhand was placed on the fabricated holder and the whole structure was used to grab the embryo on a microscope. In figure 29, the whole setup and the manipulation of the biospecimen are shown.

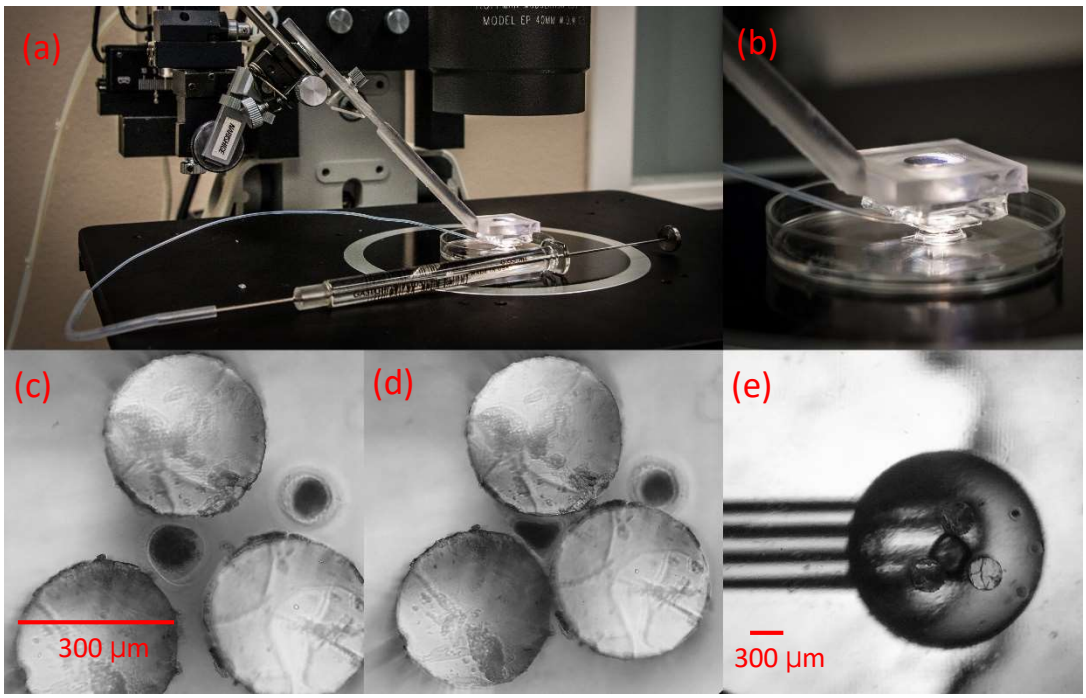

Figure.29. **Biospecimen manipulation in aqueous medium**. (a) the whole setup on the microscope. The holder and the syringe can be seen in this image (b) The square-shaped device, the holder, and the petri dish contains the embryos are shown in this photo (c) Three fingers and the embryos can be seen. The embryo is grabbed successfully without any deformation. (d) Embryo is deformed because of bigger force from fingers (e) The embryo is released.

2-3-Hybrid Hand-like Device

2-3-1-Redesign Requirements

In the former section, the fabrication of two types of monolithic microhands was described in detail. Increasing the produced force of the hand-like structure can lead to a device that can be used for manipulation of heavier objects like bigger pieces of tissues or heavier biospecimen. Body organs and tissues can be samples of heavier biospecimen. Changes in the design are essential to increase the produced force of the hand-like devices. A cylindrical hand-

like structure, similar to the cylindrical microhand can be developed in a proper way to address the demands to manipulate heavier tissues and as a surgical tool. Making the hand-like structures with a bigger size that is matched with standard trocars is one of the options to increase the produced force. In figure 30, a schematic design of the cylindrical device can be seen.

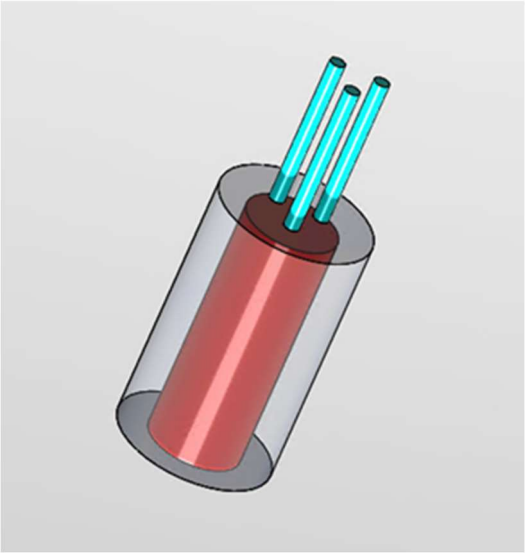

Figure.30. **Cylindrical hand-like device.** This schematic illustration was used for cylindrical microhand devices as shown earlier in this chapter. This design is scalable and can be developed in a bigger size based on the application and requirement.

To modify the hand-like structure for surgical purposes, scaling up the microhand is one approach. The limit of scaling up was determined by the sizes of the proper standard trocar. In figure 31, a photo image of a standard trocar, provided by Xcel, can be seen. The internal diameter of the trocar is 1cm so that a surgical device can pass through it and enter the abdominal space. The diameter of the hole of the trocar determines the maximum diameter of

the designed surgical tool. In the hand-like structure design, the maximum diameter of the device is 1cm.

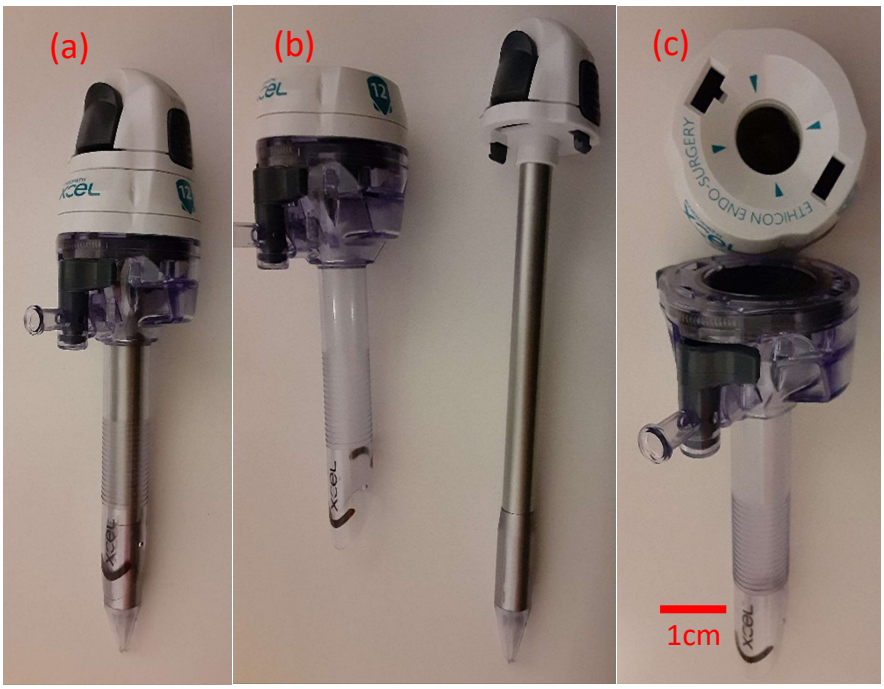

Figure.31. **A standard trocar and its parts** (a) A trocar and its parts. The cannula, the seal, and the obturator can be seen in this photo image(b) The obturator is separated from the cannula sleeve. It can be seen that the seal system is a double seal (c) The central hole on the seal can be seen. This 1cm hole is also the diameter of the cannula sleeve.

Another way of modification of the microhand, to achieve a hand-like device with the ability to produce enough force that is useful for laparoscopic surgery, is to make a hybrid structure that contains both soft and hard materials. Changing the fingers from soft to hard material can be one option to increase the produced force. To achieve such a structure, hard plastic tubes or hard 3D printed fingers can be placed over the flexible membrane to form the hybrid structure.

One of the common tools that is usually used in laparoscopic abdominal surgeries is forceps. In figure 32, commercially available forceps used in laparoscopic abdominal surgery is shown. This typical MIS tool provides a useful platform that is compatible with laparoscopic surgery. Developing a tool that can be combined with these forceps and pass through the trocar can pave the way for developing user-friendly surgical devices.

Figure. 32**. Commercial Forceps.** In this photo, commercially available forceps are shown.

2-3-2-Fabrication

The first step of the fabrication of the hybrid hand-like devices is exactly like the microhand fabrication. The steps of microhand fabrication are described in monolithic microhand fabrication part in (2-2-2). Similar to the microhand, the soft part of the hand-like structure has to be fabricated from PDMS. For the fabrication of a hand-like surgical device, it is essential to have a mold for PDMS casting. The size of the mold should be matched with the size of the final device. In figure 33, the photo image of the mold for hand-like device fabrication is shown. The

mold has a main part with three holes and a cover of mold that is responsible for forming the void and the membrane. Each hole on the main mold, to form each soft finger, has a diameter of 1 mm.

Figure.33. **Mold for hand-like device fabrication**. The mold with three holes can be seen on the left and the mold cover can be seen on the right. The Mold cover is responsible for forming the membrane and the void of the hand-like structure.

The mold that is shown in figure 33 and was used to fabricate the hand-like structure has the same fabrication and preparation steps as the mold for the fabrication of the microhand structure.

The PDMS mold casting was executed like the PDMS mold casting for the microhand. In figure 34, the fabricated hand-like PDMS-based device can be seen.

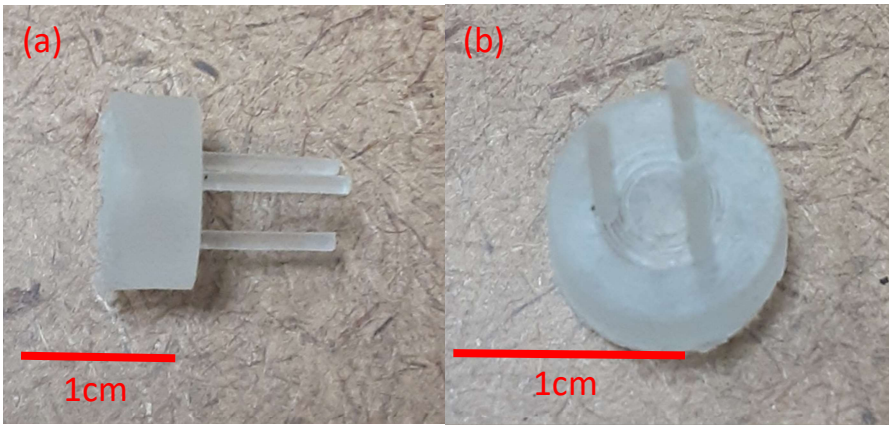

Figure.34. **Hand-like structure.** (a) The side view of the fabricated PDMS-based hand-like structure. (b) The bird-view of the same device.

To finalize the fabrication of the hand-like device, the fabricated soft membrane and fingers should be assembled on the proper 3D printed syringe tip connector. The assembling method is exactly like the one that was used for the cylindrical microhand. The final hand-like device's elements and the final product can be seen in figure 35.

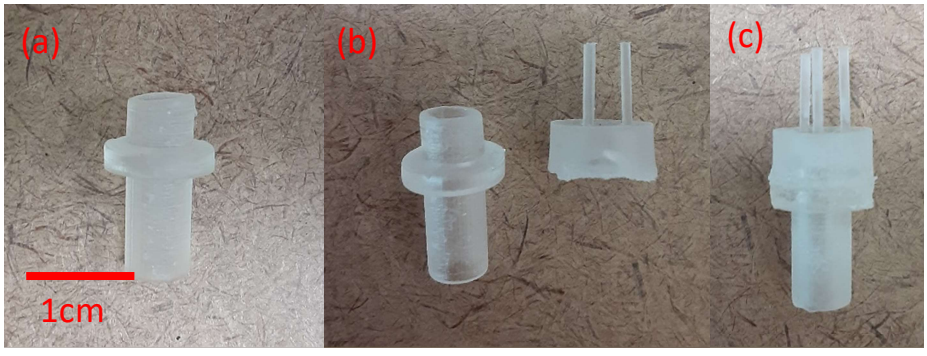

Figure.35. **The hand-like device elements and assembling.** (a) The 3D printed connector. (b) The 3D printed connector and the soft membrane. (c) The assembled hand-like device.

As it is mentioned earlier, another approach to increase the produced force of the hand-like structure is to make a hybrid device by integrating hard 3D printed fingers with the soft membrane. For this purpose, two different types of 3D printed fingers were developed. The fingers in each type were fabricated in two different lengths. Designing the fingers with various lengths is a strategy to have hand-like devices with various force production abilities. The longer the finger, the less produced force but a bigger sample grabbing ability. These fingers have to be glued to the membrane by using liquid PDMS.

In figure 36, the first design of fingers for 3D printing and the photo image of the fabricated fingers are shown. In figure 36(a,b) the simple design in two different lengths is shown. In figure 36(c,d) the photo image of the 3D printed fingers is shown. In figure 37, the assembled hand-like device with two lengths of fingers can be seen.

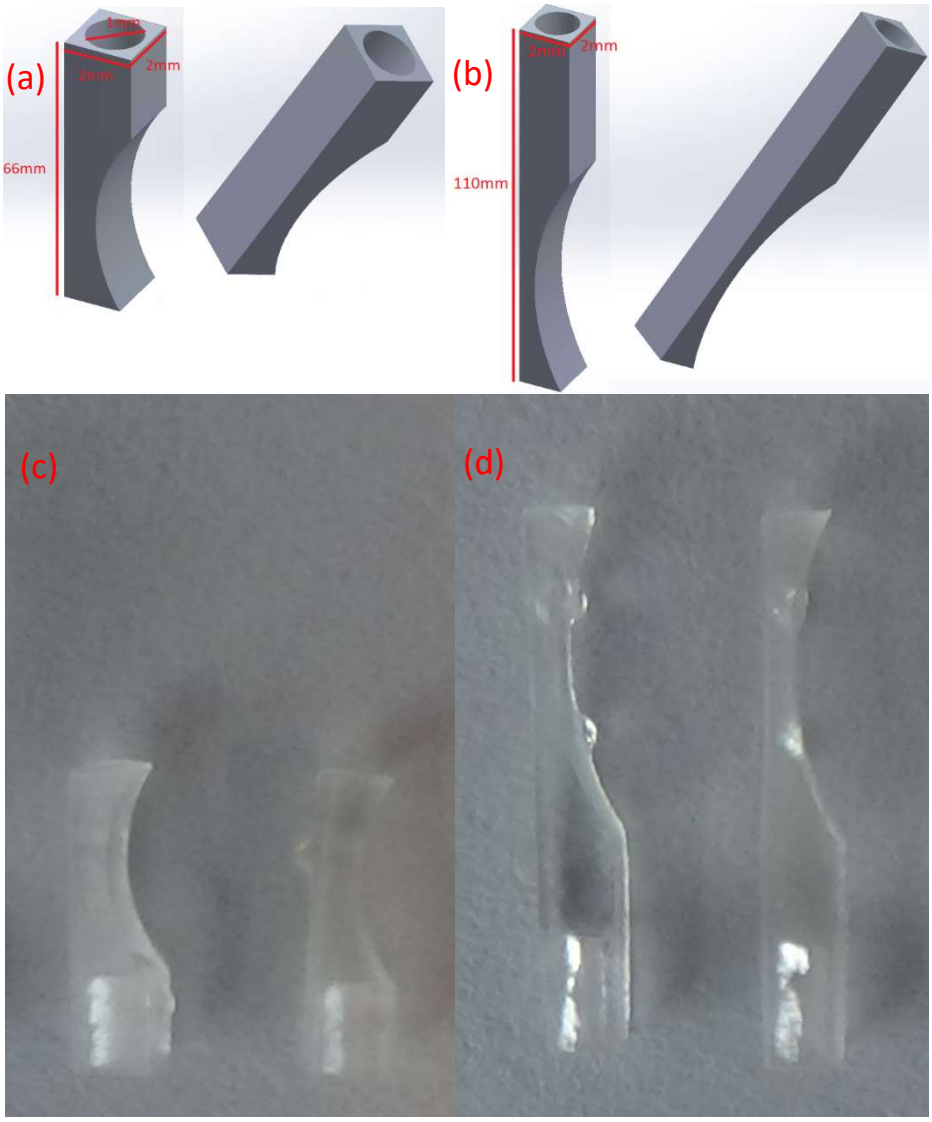

Figure.36. **3D design of fingers with Solidworks and the real 3D printed ones**. (a) Short finger schematic design and its dimensions. (b) Long finger schematic design and its dimensions. (c) 3D printed short fingers printed by Form-2 3D printer developed by Formlabs. (d) 3D printed long fingers printed by Form-2 3D printer developed by Formlabs.

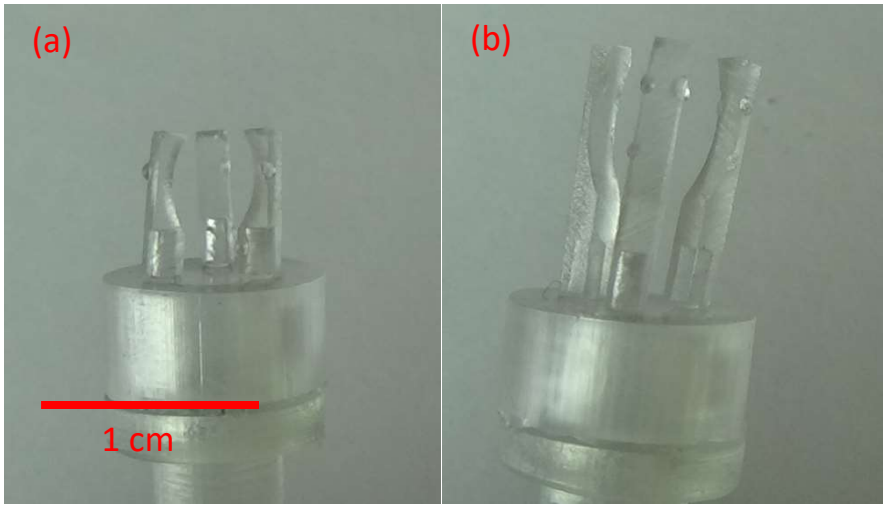

Figure.37. **Assembled hand-like device with simple 3D printed fingers.** (a) Assembled hand-like device with short fingers. (b) Assembled hand-like device with long fingers.

The other style of 3D printed finger is an improved version of the first style with a polygon-shaped connector to the soft and flexible membrane. The fingers with the new design have the same length as the aforementioned first style. The polygon-shaped connector of the fingers was designed to transfer more force from the membrane to the 3D printed fingers. To improve the attachment of the fingers to the membrane, the polygon-shaped connector has an extra five small holes in it. In figure 38, the 3D design of the improved design and the photo image of the 3D printed improved fingers can be seen. By using these improved 3D printed fingers and liquid PDMS as the glue, the fingers were glued to the flexible membrane and the improved hand-like device was formed. In figure 39, the improved hand-like device can be seen.

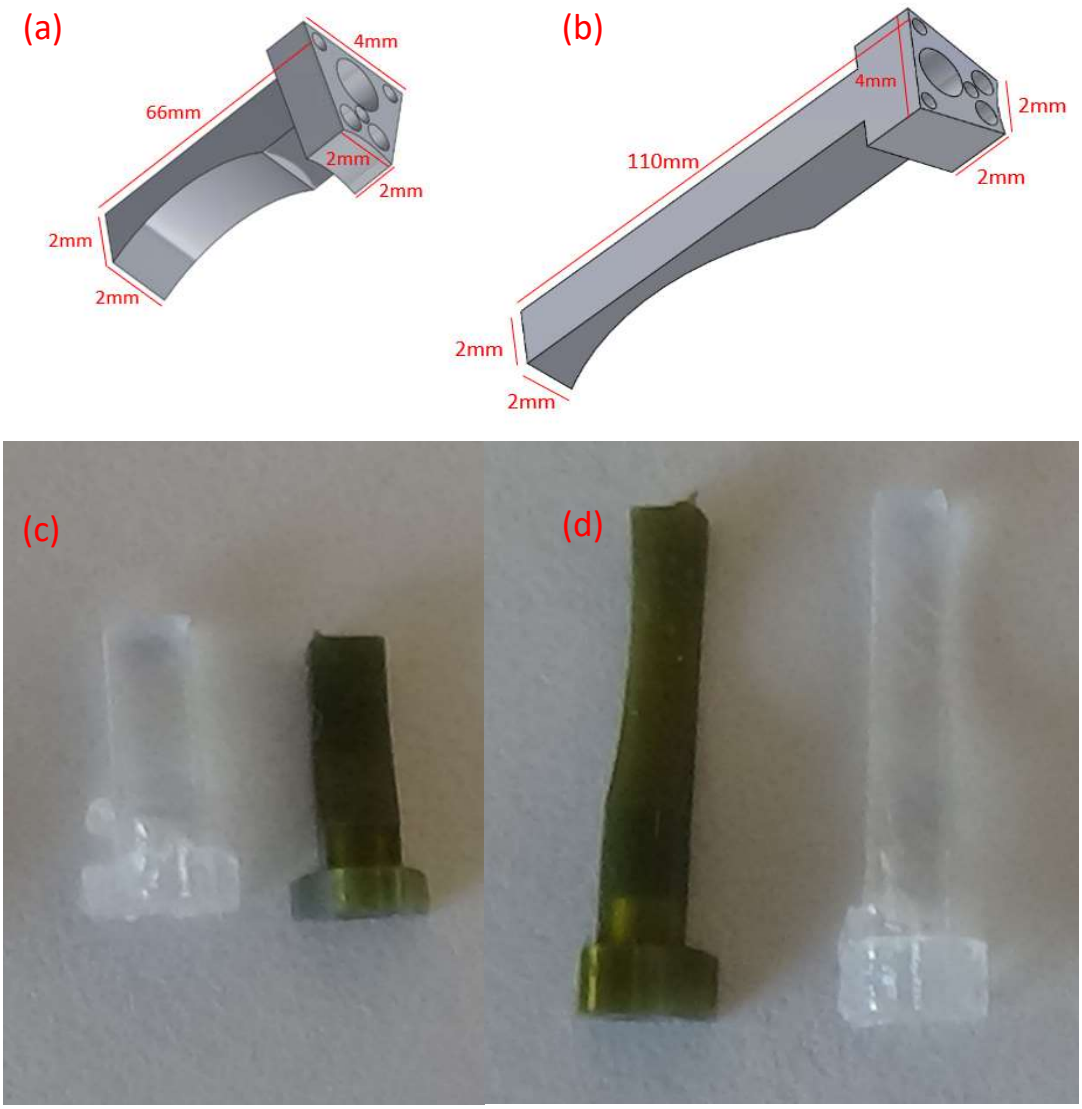

Figure.38. **3D design of fingers with Solidworks and the real 3D printed ones.** (a) Short finger schematic design and its dimensions. (b) Long finger schematic design and its dimensions. (c) 3D printed short fingers printed by Form-2 3D printer developed by Formlabs. (d) 3D printed long fingers printed by Form-2 3D printer developed by Formlabs.

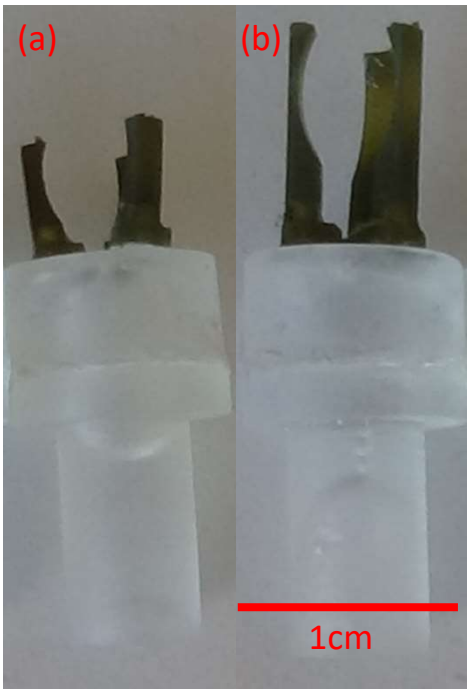

Figure.39. **Assembled hand-like device with the improved 3D printed fingers.** (a) Assembled hand-like device with short 3D printed fingers. (b) Assembled hand-like device with long 3D printed fingers.

The developed hand-like devices can be placed on the tip of standard laparoscopy forceps holders to form new soft material-based forceps. In this way, the surgeons can work with a gadget that they have experience of working with. They can handle the new gadget in the same way they handle standard forceps. As mentioned earlier, the opening and closing of the newly designed soft-material-based hand-like device are based on the hydraulic pressure variation. So, the surgeon can control the new forceps by using a syringe or a MEMS mechanical pump to change the hydraulic pressure behind the flexible membrane to open or close the hand-like device. In figure 40, the finalized forceps that are made from the combination of the developed hand-like device and the body of standard forceps for laparoscopy are shown.

Figure. 40. **Developed forceps by using the hand-like device and standard laparoscopy forceps.** (a) The whole developed forceps based on the hand-like device, trocar, and the syringe. (b) Close-up photo image of the hand-like device passed through a standard trocar. The hand-like device has a 1cm diameter.

2-3-3- Characterization

2-3-3-1-Deflection Characterization

Before utilizing any device for real-world scenarios, a proper characterization is essential. Similar to microhand bending characterization, the hand-like device was placed over the same Nikon optical microscope and characterized by using the Nikon microscope's software. For bending characterization, a normal syringe was used to inject the proper volume of water into the central void of the hand-like device. In figure 41, the injection-bending diagram is shown. This

diagram is valid for all kinds of developed hand-like devices. The injection-bending diagram is the same for the hand-like devices with short and long fingers. Also, it is similar for the devices with simple 3D printed fingers and improved 3D printed fingers.

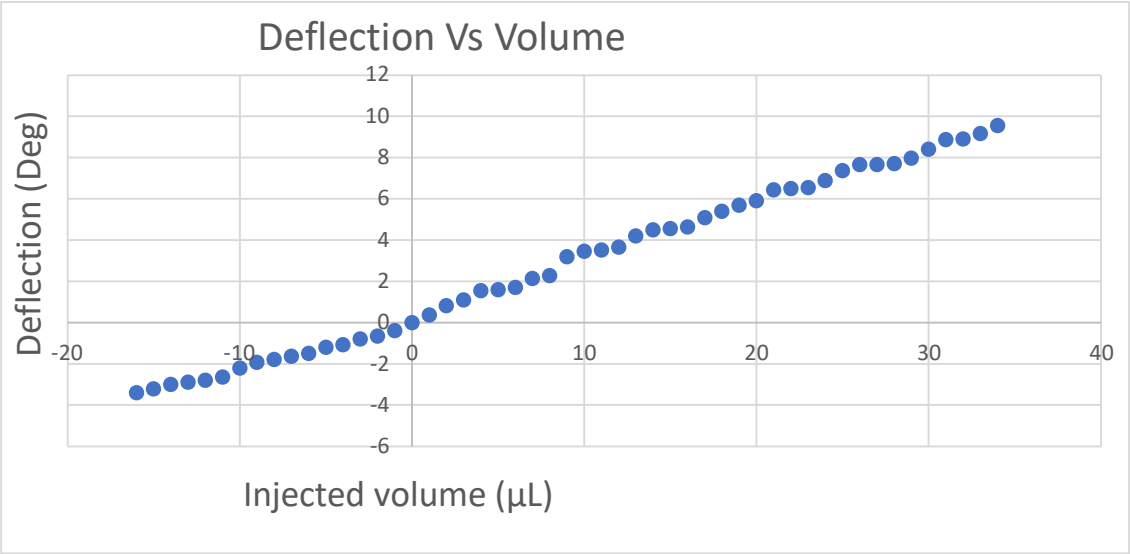

Figure. 41. **Bending characterization of the hand-like devices**. Injected volume was measured by the syringe and injected by the syringe in the device. The bending of the fingers was measured by using the Nikon optical microscope and its software. For a precise measurement, a 50µL microliter syringe was used for this characterization.

2-3-3-2-Force Characterization

A qualitative characterization was performed to evaluate the ability of the developed hand-like devices to handle specimens with various weights. For this purpose, the devices were held horizontally in front of a camera, and the weights were hung from one finger as is shown in figure 42. The suspended weights gradually increased to measure the endurance of the designed finger's ability to hold the horizontal position. As it is obvious in figure 42(a), the hand-like devices

with the simple 3D printed fingers could not tolerate even 1 gr of wires, while as it is shown in figure 42(b), the devices that were developed with the use of modified 3D printed fingers were able to hold 16 gr of suspended weight.

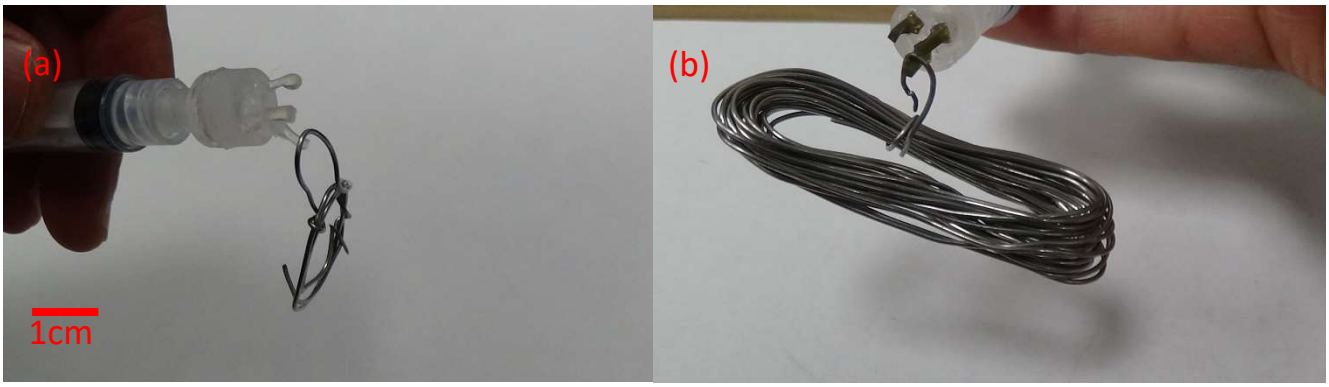

Figure.42. **Qualitative produced force characterization.** (a) Hand-like structure with simple 3D printed fingers that cannot hold 1gr of weight properly. (b) hand-like structure with improved 3D printed fingers that can hold 16 gr of weight horizontally.

This experiment can show the qualitative increase in the produced force of hand-like devices by switching from simple fingers to improved 3D printed fingers.

2-3-4-Handling Tissue

A piece of chicken breast was used to mimic internal organ tissues in this research. In figure 43, a piece of chicken breast is used to mimic internal organs, and it is manipulated by the use of an improved hand-like device placed on the tip of a standard syringe.

Figure.43. **A piece of chicken breast is manipulated to mimic internal organ manipulation.** As it can be seen, the hand-like device is holding a piece of chicken breast.

It is described before and showed in figure 40 that forceps were developed by combining an improved hand-like device and standard forceps holder. The reason that these kinds of forceps were developed was to combine the benefits of the newly designed hand-like devices with standard forceps structure that make it easier for surgeons to handle the new one. To mimic a real abdominal laparoscopic surgery by using the newly developed device, at first a trocar was placed over a Styrofoam box to mimic the abdominal area. Then, the handling of the chicken breast was performed by using the new device inside the box. In figure 44, the manipulation of the piece of the chicken breast by using newly developed forceps is shown. It proves that it can be used for abdominal laparoscopic surgery.

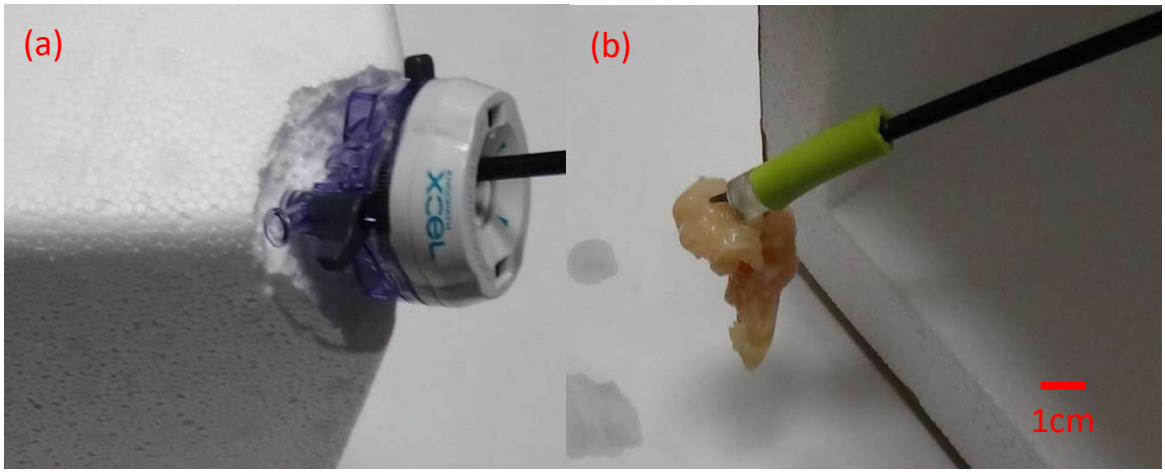

Figure.44. **Abdominal laparoscopic surgery is mimicked** (a) The trocar is placed on the Styrofoam box and the forceps are inserted into the box through the trocar. (b) The piece of chicken is manipulated by using the new forceps inside the box.

2-4-Discussion

The innovative hand-like devices were developed by using soft material molding, 3D printed molds, and 3D printed fingers. The microhands made from PDMS, with their produced force and motion precisely controllable, made this innovative manipulator a practical option for biospecimen handling. Also, hand-like hybrid devices can be used for abdominal laparoscopic surgeries.

As mentioned in the fabrication parts, the proposed microhand can be fabricated in a single-step molding of PDMS. The innovative, encapsulated, molding technique was used to fabricate two different types of microhands introduced in this dissertation. The actuation mechanism is the bending of a flexible membrane due to pressure difference on two surfaces of the membrane. As it can be concluded from equation (1) the higher-pressure difference or a

wider membrane will cause more deformation. At the same time, a thicker membrane or a stiffer material can limit the deformation of the membrane. The fingers of the microhand were placed on this flexible membrane. The hand-like surgical device works with the same mechanism. The fabrication of this surgical device has an extra step. To increase the produced force, 3D printed fingers were placed and glued to the membrane and the hybrid hand-like device was formed from the combination of the PDMS soft material and 3D printed hard material.

The same optical method was used to characterize the bending of fingers in both microhands and hand-like hybrid devices. The precision in the bending of the fingers is revealed from characterization. The wide range of the bending of the fingers, alongside the precise controllability of this bending, confirms the ability of the developed devices to manipulate a wide range of fragile objects. The bending angle for each finger was ranged from 8 degrees of closing to 13 degrees of opening for square-shaped devices, and from 4.4 degrees of closing to 10.2 degrees of opening for cylindrical-shaped devices. The precision of the fingers' deflection highly depends on the microliter syringes' precision and the precision in controlling the syringes. Each step of the injected volume into the cavity of a microhand was 0.1 µL. The minimum step of the measured bending angle was 0.4 of a degree for the square-shaped devices and 0.1 of a degree for the cylindrical-shaped devices. The characterization of the hand-like hybrid device was performed, and the bending angle was ranged from 3.41 degrees of closing to 9.56 degrees of opening. Each step of the injected volume into the cavity of the hand-like device was 1 µL, and the minimum step of the measured bending angle was 0.01 degree.

The force measurement revealed that the maximum produced force of the microhands is smaller than 1mN, which means they are suitable for biospecimen handling [50]. The maximum

absolute produced force of a single finger in a square-shaped device is around 181 μN, which means three fingers can impose around 543 μN on a specimen. Similarly, the experiments revealed the absolute maximum force a finger can produce in a cylindrical-shaped device is 30 μN, which is equal to 90 μN for three fingers. The force-volume ratio, which can be described as the absolute force divided by the volume of the gripper and actuator, for the square-shaped microhand is 1.13 mN/mm^3, and for the cylindrical-shaped device is 0.141 mN/mm^3. According to other researchers, other soft grippers have a maximum absolute produced force of 50mN, 3mN, and 2.2 mN, and when the size of the grippers are taken into account, the force-volume ratio is 0.78, 3.3, and 0.047 mN/mm^3, respectively [51-53]. Both the produced force and force-volume ratio are higher or comparable with other soft manipulators [54]. Additionally, a qualitative force characterization was performed to characterize hand-like hybrid devices. The results of this qualitative characterization showed that making a hybrid hand-like structure based on the improved 3D printed fingers can remarkably increase the produced force by the device.

The simulation of the microhand revealed that the 3D model in the finite-element software ABAQUS 6.12 can be used successfully to predict the actuation of the fingers. The results of this simulation can be used as a design tool to optimize the required parameters of the device. Disagreements between the simulation and experimental measurements are mainly because of microscale variation of used PDMS in the membrane, soft material variations during the fabrication, or fabrication method resolutions. Additionally, absorption of the hydraulic pressure by different parts, like soft tubes that were used for transferring pressure from the syringes to the device or soft surfaces other than the membrane, caused differences between simulations and experimental measurements. While more development of simulation models can cause a

better prediction of a microhand's moving manner, it can cause a proper prediction of the produced force of the fingers.

The manipulation of the biospecimen was the last experiment for all the hand-like developed devices in this chapter. Manipulation of an ant was performed successfully by using microhands in the air. Goat embryo manipulation also was performed in an aqueous medium with the square-shaped microhand successfully. These experiments proved the ability of microhands to manipulate fragile biospecimen. To test the ability of the hybrid hand-like device to manipulate a biospecimen, a piece of chicken was chosen as the sample and manipulated successfully. The piece of chicken was an option to mimic the internal abdominal organs, and successful manipulation of it proved the developed device can be used in minimally invasive surgery.

2-5-Bibliography

1) A. M. Okamura, "Haptic Feedback in Robot-Assisted Minimally Invasive Surgery," *NIH Public Access*, vol. 19, no. 1, pp. 102–107, 2009, doi: 10.1097/MOU.0b013e32831a478c.

2) M. J. Mack, "Minimally Invasive and Robotic Surgery," *Oppor. Med. Res.*, vol. 285, no. 5, pp. 568–572, 2001, doi: 10.1001/jama.285.5.568.

3) N. R. Sinatra, C. B. Teeple, D. M. Vogt, K. K. Parker, D. F. Gruber, and R. J. Wood, "Ultragentle manipulation of delicate structures using a soft robotic gripper," *Sci. Robot.*, vol. 4, no. 33, pp. 1–12, 2019, doi: 10.1126/SCIROBOTICS.AAX5425.

4) D. M. Vogt *et al.*, "Shipboard design and fabrication of custom 3D-printed soft robotic

manipulators for the investigation of delicate deep-sea organisms," *PLoS One*, vol. 13, no. 8, pp. 1–16, 2018, doi: 10.1371/journal. pone.0200386.

5) K. T. Andrzejewski, M. P. Cooper, C. A. Griffiths, and C. Giannetti, "Optimisation process for robotic assembly of electronic components," *Int. J. Adv. Manuf. Technol.*, vol. 99, pp. 2523–2535, 2018, doi: 10.1007/s00170-018-2645-y.

6) B. J. Schroer and E. F. Stafford, "Issues in Using Robots for Electronics Assembly," *Robotics*, vol. 2, no. 3, pp. 225–235, 1986, doi: 10.1016/0167-8493(86)90031-8.

7) V. Vitiello, S. Lee, T. P. Cundy, and G. Yang, "Emerging Robotic Platforms for Minimally Invasive Surgery," *IEEE Rev. Biomed. Eng.*, vol. 6, pp. 111–126, 2013, doi: 10.1109/RBME.2012.2236311.

8) C. Bergeles and G. Z. Yang, "From passive tool holders to microsurgeons: Safer, smaller, smarter surgical robots," *IEEE Trans. Biomed. Eng.*, vol. 61, no. 5, pp. 1565–1576, 2014, doi: 10.1109/TBME.2013.2293815.

9) K. C. Galloway *et al.*, "Soft Robotic Grippers for Biological Sampling on Deep Reefs," *Soft Robot.*, vol. 3, no. 1, pp. 23–46, 2016, doi: 10.1089/soro.2015.0019.

10) J. Zhou, S. Chen, and Z. Wang, "A Soft-Robotic Gripper With Enhanced Object Adaptation and Grasping Reliability," *IEEE Robot. Autom. Lett.*, vol. 2, no. 4, pp. 2287–2293, 2017, doi: 10.1109/LRA.2017.2716445.

11) D. T. Pham and S. H. Yeo, "Strategies for gripper design and selection in robotic assembly," *Int. J. Prod. Res.*, vol. 29, no. 2, pp. 303–316, 1991, doi: 10.1080/00207549108930072.

12) M. Verotti, A. Dochshanov, and N. P. Belfiore, "Compliance Synthesis of CSFH MEMS-Based

Microgrippers," *J. Mech. Des. Trans. ASME*, vol. 139, no. 2, pp. 1–10, 2017, doi: 10.1115/1.4035053.

13) M. Honarpardaz, M. Tarkian, J. Ölvander, and X. Feng, "Finger design automation for industrial robot grippers : A review," *Rob. Auton. Syst.*, vol. 87, pp. 104–119, 2017, doi: 10.1016/j.robot.2016.10.003.

14) M. Garcés-schröder, L. Hecht, A. Vierheller, M. Leester-schädel, M. Böl, and A. Dietzel, "Micro-Grippers with Femtosecond-Laser Machined In-Plane Agonist-Antagonist SMA Actuators Integrated on Wafer-Level by Galvanic Riveting," in *Eurosensors*, 2017, pp. 1–5, doi: 10.3390/proceedings1040385.

15) Y. Yang, J. Lou, G. Wu, Y. Wei, and L. Fu, "Design and position / force control of an S-shaped MFC microgripper," *Sensors Actuators A Phys.*, vol. 282, pp. 63–78, 2018, doi: 10.1016/j.sna.2018.09.021.

16) S. Bütefisch, V. Seidemann, and S. Büttgenbach, "Novel Micro-pneumatic actuator for MEMS," *Sensors Actuators A Phys.*, vol. 97–98, pp. 638–645, 2002, doi: 10.1016/S0924-4247(01)00843-3.

17) P. Moseley, J. M. Florez, H. A. Sonar, G. Agarwal, W. Curtin, and J. Paik, "Modeling, Design, and Development of Soft Pneumatic Actuators with Finite Element Method," *Adv. Eng. Mater.*, vol. 18, no. 6, pp. 978–988, 2016, doi: 10.1002/adem.201500503.

18) S. Chopra and N. Gravish, "Piezoelectric actuators with on-board sensing for micro-robotic applications," *Smart Mater. Struct.*, vol. 28, no. 11, p. 10pp, 2019, doi: 10.1088/1361-

665X/ab43fe.

19) F. Filhol, E. Defaÿ, C. Divoux, C. Zinck, and M.-T. Delaye, “Resonance Micro-mirror excited by a thin-film piezoelectric actuator for fast optical beam scanning,” *Sensors Actuators A Phys.*, vol. 123–124, pp. 483–489, 2005, doi: 10.1016/j.sna.2005.04.029.

20) Q. Xu, “Precision Position/Force Interaction Control of a Piezoelectric Multimorph Microgripper for Microassembly,” *IEEE Trans. Autom. Sci. Eng.*, vol. 10, no. 3, pp. 503–514, 2013, doi: 10.1109/TASE.2013.2239288.

21) N. T. Jafferis, M. Lok, N. Winey, G. Y. Wei, and R. J. Wood, “Multilayer laminated piezoelectric bending actuators: Design and manufacturing for optimum power density and efficiency,” *Smart Mater. Struct.*, vol. 25, no. 5, 2016, p.13pp, doi: 10.1088/0964-1726/25/5/055033.

22) D. H. Wang, Q. Yang, and H. M. Dong, “A Monolithic Compliant Piezoelectric-Driven Microgripper: Design, Modeling, and Testing,” *IEEE/ASME Trans. Mechatronics*, vol. 18, no. 1, pp. 138–147, 2013, doi: 10.1109/TMECH.2011.2163200.

23) M. Karpelson, G.-Y. Wei, and R. J. Wood, “Driving high voltage piezoelectric actuators in microrobotic applications,” *Sensors Actuators A Phys.*, vol. 176, pp. 78–89, 2012, doi: 10.1016/j.sna.2011.11.035.

24) C. Calhoun, R. Wheeler, T. Baxevanis, and D. . Lagoudas, “Actuation fatigue life prediction of shape memory alloys under the constant-stress loading condition,” *Scr. Mater.*, vol. 95, pp. 58–61, 2015, doi: 10.1016/j.scriptamat.2014.10.005.

25) A. Nespoli, S. Besseghini, S. Pittaccio, E. Villa, and S. Viscuso, “The high potential of shape

memory alloys in developing miniature mechanical devices : A review on shape memory alloy mini-actuators," *Sensors Actuators A Phys.*, vol. 158, pp. 149–160, 2010, doi: 10.1016/j.sna.2009.12.020.

26) J. W. Sohn, G.-W. Kim, and S.-B. Choi, "A State-of-the-Art Review on Robots and Medical Devices Using Smart Fluids and Shape Memory Alloys," *Appl. Sci.*, vol. 8, no. 1928, pp. 1–21, 2018, doi: 10.3390/app8101928.

27) C. R. Knick, D. J. Sharar, A. A. Wilson, G. L. Smith, C. J. Morris, and H. A. Bruck, "High frequency , low power , electrically actuated shape memory alloy MEMS bimorph thermal actuators," *J. Micromechanics Microengineering*, vol. 29, no. 7, pp. 1–8, 2019, doi: 10.1088/1361-6439/ab1633.

28) Z. Wang, G. Hang, J. Li, Y. Wang, and K. Xiao, "A micro-robot fish with embeded SMA wire actuaed flexible biomimetic fin," *Sensors Actuators A Phys.*, vol. 144, no. 2, pp. 354–360, 2008, doi: 10.1016/j.sna.2008.02.013.

29) H. Asadi, M. Eynbeygi, and Q. Wang, "Nonlinear thermal stability of geometrically imperfect shape memory alloy hybrid laminated composite plates," *Smart Mater. Struct.*, vol. 23, no. 7, pp. 1–13, 2014, doi: 10.1088/0964-1726/23/7/075012.

30) S. Szykowny and M. H. Elahinia, "Heat Transfer Analysis of Shape Memory Alloy Actuators," in *IMECE*, 2006, pp. 105–112, doi: 10.1115/IMECE2006-13788.

31) Z. Liu, K. Xiao, Z. Hou, F. Yan, Y. Chen, and L. Cai, "Multifunctional Coating with Both Thermal Insulation and Antibacterial Properties Applied to Nickel-Titanium Alloy," *Int. J. Nanomedicine*,

vol. 15, pp. 7215–7234, 2020, doi: 10.2147/IJN.S266247.

32) S. Yang and Q. Xu, “A review on actuation and sensing techniques for MEMS-based microgrippers,” *J. Micro-Bio Robot*, vol. 13, pp. 1–14, 2017, doi: 10.1007/s12213-017-0098-2.

33) Z. Qiu and W. Piyawattanamatha, “New Endoscopic Imaging Technology Based on MEMS Sensors and Actuators,” *Micromachines*, vol. 8, no. 210, pp. 1–27, 2017, doi: 10.3390/mi8070210.

34) R. Ramesham and R. Ghaffarian, “Challenges in Interconnection and Packaging of Microelectromechanical Systems (MEMS),” in *2000 Electronic Components and Technology Conference*, 2000, no. Ic, pp. 666–675, doi: 10.1109/ECTC.2000.853230.

35) H. Yang, M. Xu, W. Li, and S. Zhang, “Design and Implementation of a Soft Robotic Arm Driven by SMA Coils,” *IEEE Trans. Ind. Electron.*, vol. 66, no. 8, pp. 6108–6116, 2019, doi: 10.1109/TIE.2018.2872005.

36) S. Baghbani Kordmahale and J. Kameoka, “Smart Soft Actuation System,” *Ann. Mater. Sci. Eng.*, vol. 2, no. c, pp. 2–3, 2015, [Online]. Available: https://austinpublishinggroup.com/material-science-engineering/fulltext/amse-v2-id1021.php.

37) B. Gorissen, D. Reynaerts, S. Konishi, K. Yoshida, J. W. Kim, and M. De Volder, “Elastic Inflatable Actuators for Soft Robotic Applications,” *Adv. Mater.*, vol. 29, no. 43, pp. 1–14, 2017, doi: 10.1002/adma.201604977.

38) M. De Volder and D. Reynaerts, “Pneumatic and hydraulic microactuators: A review,” *J. Micromechanics Microengineering*, vol. 20, no. 4, pp. 1–18, 2010, doi: 10.1088/0960-1317/20/4/043001.

39) S. Ozbek, E. Foo, J. W. Lee, N. Schleif, and B. Holschuh, “Low-power, minimal-heat exposure shape memory alloy (SMA) actuators for on-body soft robotics,” in *Proceedings of the 2019 Design of Medical Devices Conference*, 2019, pp. 1–5, doi: 10.1115/DMD2019-3287.

40) A. Miriyev, K. Stack, and H. Lipson, “Soft material for soft actuators,” *Nat. Commun.*, vol. 8, no. 1, pp. 1–8, 2017, doi: 10.1038/s41467-017-00685-3.

41) D. Rus and M. T. Tolley, “Design, Fabrication and control of soft robots,” *Nature*, vol. 521, pp. 467–475, 2015, doi: 10.1038/nature14543.

42) D. Steck, J. Qu, S. B.Kordmahale, D. Tscharnuter, A. Muliana, and J. Kameoka, “Mechanical responses of Ecoflex silicone rubber : Compressible and incompressible behaviors,” *J. Appl. Polym. Sci.*, vol. 136, no. 5, pp. 1–11, 2019, doi: 10.1002/app.47025.

43) F. Hartmann, M. Baumgartner, and M. Kaltenbrunner, “Becoming Sustainable, The New Frontier in Soft Robotics,” *Adv. Mater.*, vol. 2004413, pp. 1–32, 2020, doi: 10.1002/adma.202004413.

44) Z. Samadikhoshkho, K. Zareinia, and F. Janabi-Sharifi, “A Brief Review on Robotic Grippers Classifications,” in *2019 IEEE Canadian Conference of Electrical and Computer Engineering*, 2019, pp. 10–13, doi: 10.1109/CCECE.2019.8861780.

45) M. Bao, “Chapter 2-Mechanics of Beam and Diaphragm Structures,” in *Analysis and Design Principles of MEMS Devices*, 2005, pp. 33–114, doi: 10.1016/B978-044451616-9/50003-5.

46) S. B. Kordmahale, J. Do, K. A. Chang, and J. Kameoka, “Low Cost and Piezoelectric based Soft Wave Energy Harvester,” in *MRS Advances*, 2019, vol. 4, no. 15, pp. 889–895, doi:

10.1557/adv.2018.675.

47) P.-J. Huang, S. Baghbani Kordmahale, C.-K. Chou, H. Yamaguchi, M.-C. Hung, and J. Kameoka, "Development of automated high throughput single molecular microfluidic detection platform for signal transduction analysis," in *SPIE 9705, Microfluidics, BioMEMS, and Medical Microsystems XIV*, vol. 9705, pp. 1–5, doi: 10.1117/12.2213259.

48) A. P. Saghati, S. B. Kordmahale, A. P. Saghati, J. Kameoka, and K. Entesari, "Reconfigurable quarter-mode SIW antenna employing a fluidically switchable via," in *2016 IEEE Antennas and Propagation Society International Symposium, APSURSI 2016 - Proceedings*, 2016, pp. 845–846, doi: 10.1109/APS.2016.7696131.

49) A. P. Saghati, S. B. Kordmahale, J. Kameoka, and K. Entesari, "Reconfigurable Quarter-Mode Substrate Integrated Waveguide Cavity Filter Employing Liquid-Metal Capacitive Loading," in *2015 IEEE MTT-S International Microwave Symposium*, 2015, pp. 20–22, doi: 10.1109/MWSYM.2015.7166885.

50) S. Shimomura, Y. Teramachi, Y. Muramatsu, S. Tajima, Y. Tabata, and S. Konishi, "Pinching and releasing of cellular aggregate by microfingers using PDMS pneumatic balloon actuators," *Proc. IEEE Int. Conf. Micro Electro Mech. Syst.*, no. 3, pp. 925–926, 2014, doi: 10.1109/MEMSYS.2014.6765793.

51) S. Konishi, F. Kawai, and P. Cusin, "Thin flexible end-effector using pneumatic balloon actuator," *Sensors Actuators, A Phys.*, vol. 89, no. 1–2, pp. 28–35, 2001, doi: 10.1016/S0924-4247(00)00533-1.

52) Y. Watanabe *et al.*, “SMALL, SOFT, AND SAFE MICROACTUATOR FOR RETINAL PIGMENT EPITHELIUM TRANSPLANTATION,” in *20th IEEE International Conference on Micro Electro Mechanical Systems, MEMS 2007*, 2007, no. January, pp. 659–662.

53) S. Wakimoto, K. Suzumori, and K. Ogura, “Miniature pneumatic curling rubber actuator generating bidirectional motion with one air-supply tube,” *Adv. Robot.*, vol. 25, no. 9–10, pp. 1311–1330, 2011, doi: 10.1163/016918611X574731.

54) J. Paek, I. Cho, and J. Kim, “Microrobotic tentacles with spiral bending capability based on shape-engineered elastomeric microtubes,” *Scientific Reports*, vol. 5. pp. 1–12, 2015, doi: 10.1038/srep10768.

CHAPTER III

SOFT MATERIALS AND DEVELOPMENT OF HYBRID STRUCTURE OF PIEZOELECTRIC TRANSDUCERS AND SOFT MATERIALS AS WAVE ENERGY CONVERTER*

3-1- Introduction

Renewable energy has been a highly demanded instrument for economic and social growth, supply infrastructures in remote areas, and climate change mitigation [1-3]. However, there are roadblocks for the development and investment for renewable energy-based technologies because of policymaking, lack of financial incentive, mainstream energy firms' interests, and lack of skilled specialists in the field [4-6]. The growth in the use of renewable energy sources has become increasingly important in the current high energy consumption world. The main reasons to attract renewable energies are harvesting energy from nature with less environmental impacts and the positive effects on the countries' GDP [6-7]. For instance, using solar energy to power remote mines and oil extraction facilities, or demand for electricity for remote sensing are some of the examples of using renewable energy in the modern era. These are examples of energizing applications far from a power distribution network that can reduce the negative environmental effects [5, 8-10].

A proper strategy for using renewable energy sources can be chosen based on the distribution of renewable energy sources on the planet and the energy demand [11]. The abundance of vibrational kinetic energy on earth makes its conversion to electricity for use in

*Part of this chapter is reprinted with permission from "Low Cost and Piezoelectric based Soft Wave Energy Harvester" by S.B.Kordmahale, J.Do, K.A.Chang, J.Kameoka, 2019, MRS Advances, Volume 4, Issue 15: energy-transfer, storage and conversion, Copyright 2019 by SpringerLink.

modern applications [12-14]. Water wave energy is one of the most abundant sources that can be used as a source of sustainable vibration energy [15]. To harvest electrical energy from water waves, four different transducers have been investigated. These are electromagnetic, electrostatic, triboelectric, and piezoelectric transducers [16-19]. These transducers can be integrated into buoys or surface attenuators floating on the surface of the ocean to convert water wave vibration into electricity. The main drawbacks of these floaters are their gigantic size to increase energy conversion efficiency up to practical level, as a result, the costs for platform parts, components, deployment, and maintenance are extraordinarily increased that reduce the attractiveness of wave energy harvesters [20-22]. Additionally, loud noise from these platforms, as well as problems caused by anchoring on the seabed, change the marine ecosystem near the harvester and on the seafloor alongside the hazardous effect of chemicals used in the gigantic harvester impacted negatively on the environment [23,24].

Electromagnetic-based energy conversion platforms have some advantages such as low impedance and are suited for large-scale energy production. Electromagnetic-based transducers in their conventional form need a resonance mechanical system to provide proper actuation of the magnet and coil. To harvest energy from low-frequency vibrations, these harvesters rely on a frequency up-conversion mechanism. Resonance-based mechanical systems lead to high complexities and cost in design, bulky structures, and high cost in maintenance. So, this mechanical structure and its negative effects are the main drawbacks of using electromagnetic transducers for large-scale energy conversion. For small-scale energy harvesting, the fabrication of coils and magnets for micro-scale devices is expensive and difficult, which is the drawback of this conversion method [25]. The electrostatic mechanical energy harvesters are working based

on the charged variable capacitors. They can be used for small-scale energy harvesting because they are compatible with MEMS technology. The main drawbacks of this type of harvesters are their low power output and their dependency on an external voltage supply or electrets. The main problem of electret-based devices is also the low durability of charges in electrets [25-27].

The triboelectric-based harvesters use two mechanisms simultaneously: triboelectric effect and electrostatic induction. The main issues with this complicated mechanism are the use of nanostructures in triboelectric nano-generators, complex design requirements, complications in finding the right pairs of materials, high level of wear and tear and low durability, and alongside packaging and isolating complexities [28,29]. The piezoelectric-based energy harvester has an issue of material limitations [30]. However, the main advantages of piezoelectric-based devices are the simple nature of piezoelectric transducers, which enable designers to use a simple mechanism in the harvester, in addition to their durability, high voltage, and high impedance of output [31-33].

To maximize the electric power production with piezoelectric-based harvesters, several methods have been investigated. Using the force increasing and focusing systems [34], use of resonance frequency [35], adjusting the resonance frequency to achieve a broader harvesting frequency range [36], using better piezoelectric materials [37], using a non-resonance and non-linear vibrating system [38-40], and rotational harvesters [41] are the most important techniques to achieve maximum power production. There are limitations to choosing proper piezoelectric material from the limited list of these materials [42], while rotational piezo harvesters have their complicated and expensive structure [41,43]. Other technics also need complicated mechanics

and should still be placed on or connected to buoys and attenuators, thus increase their costs and complexities without solving the aforementioned problems.

Based on the required scale of energy and operation environment, the most optimal power generation system must be selected [44-47]. In this research, piezoelectric transducers and soft material were integrated to produce WECs and they were deployed and tested in a wave flume successfully. The commercially available Macro Fiber Composites (MFCs) in the proper configuration, alongside bubble wrap and encapsulation in the Ecoflex 030 biocompatible soft polymeric material, conformed a WEC of a flexible structure to no mechanical complexities and minimum environmental negative effects [48]. This innovative design uses the low-cost elements in a new composition, and for a new application. The scalability of the harvester along with its wideband working frequency makes the design compatible with large-scale energy harvesting. The Ecoflex 030 which was used to encapsulate the structure's elements, is an environmentally friendly material that led to a structure without toxic emission. The performance of the wave energy converter, vertically in the curtain-like configuration, was investigated in the wave flume tank. Then, the fabricated WECs with different numbers of MFCs were placed horizontally and investigated their power performance in a floating configuration in the wave flume.

3-2-Design and Fabrication

A flexible and floatable structure, made from biofriendly soft material and containing a flexible piezoelectric transducer, is a good option to act as a WEC with minimum negative environmental effects, and with an efficient and cost-effective design. Piezoelectric transducers have a high energy density production capability, which makes them an alluring option for this

purpose [49]. It helped to reduce the size of the WEC and minimize the deployment cost. Moreover, to reduce the environmental drawbacks of conventional WECs, a proper structural shape, and environmentally friendly materials have been selected to avoid acoustic noise influences [50-52]. Also, the piezoelectric conversion mechanism can be useful to reduce the number of additional moving parts and consequent acoustic noises, and lower maintenance costs [52-54].

The proper piezoelectric converter should be matched with a flexible structure. The MFC units can provide a high energy density as a piezoelectric transducer and a flexible structure [55]. M17007-P2, which is manufactured by Smart-materials, is chosen to be used in the proposed WEC. This P2-type MFC uses the d_{31} piezoelectric index, which is smaller than d_{33} for PZT fibers. While $d_{31}<d_{33}$, the aluminum-based bottom-top electrode topology that is used in P2-types MFCs increases the electric charge gathering and output current [56]. The PZT fibers are sandwiched between electrodes and Kapton films by epoxy. The average shear modulus of MFCs is 5.515 Gpa, and the average capacitance is 98.5 nF for this model [57]. The photo Image and structure of the MFC are depicted in figure 45. In figure 45(a) the photo image of M17007-P2 MFC is depicted. Figure 45(b) shows a magnified part of the red square box in Figure 1.a; the electrodes can be seen in this image. Figure 1.c shows the schematic 3D diagram of the M17007-P2 MFC. The bottom-top electrodes of P2-type MFCs are depicted in this schematic diagram.

Ecoflex 030 with a shear modulus of 22.081Kpa has been chosen as an encapsulation platform because of its light, flexible, and cost-effective properties, and resistance to highly corrosive saltwater [58]. Moreover, it is possible to shape this elastomer by using a soft-material casting method, which is cost-effective in comparison to other methods like standard lithography

[59-61]. The mold for this purpose can be fabricated by 3D printer [62]. To guarantee the buoyancy of the structure, a piece of bubble wrap was integrated into the Ecoflex as a flexible filler that reduces the overall density of the structure. Using these materials in a sheet-like form can create a floatable, bendable, and durable structure. This structure can then be used as an ideal platform and integrated with the proper piezoelectric elements to form the desired WEC.

Figure 46 demonstrates the schematic diagram of the fabrication process, as shown previously [62]. In figure 46(a), the schematic diagram of empty mold is depicted. This mold is made by bonding individually 3D printed parts on a Plexiglas plate. As a first step, the liquid Ecoflex 030 was dispensed on this mold until it was half-filled. Bubble wrap and MFCs were placed on the top of the Ecoflex 030 successively as shown in figure 46(b). To finalize the fabrication of the OWEC, another portion of Ecoflex 030 solutions was dispensed on top of the bubble wrap and MFCs as shown in figure 46(c). After curing the Ecoflex for four hours at 25°C, the elastomer is crosslinked, and the OWEC fabrication process is completed as shown in figure 46(d,e). A photo image of the OWEC with four MFCs and dimensions of 25cmX25cmX0.4cm is depicted in figure 46(f). As can be seen in the figure. 1g, the MFCs are connected in parallel for the energy harvesting experiment. To produce maximum electrical energy from the same harvester, it is essential to choose the proper connecting configuration for the MFCs and the optimum number of transducers at the same time. Previous experiments for MFCs have concluded that the same number of MFCs will produce more electrical energy if they are connected in parallel rather than in series, so the same approach was chosen in this research [63, 64].

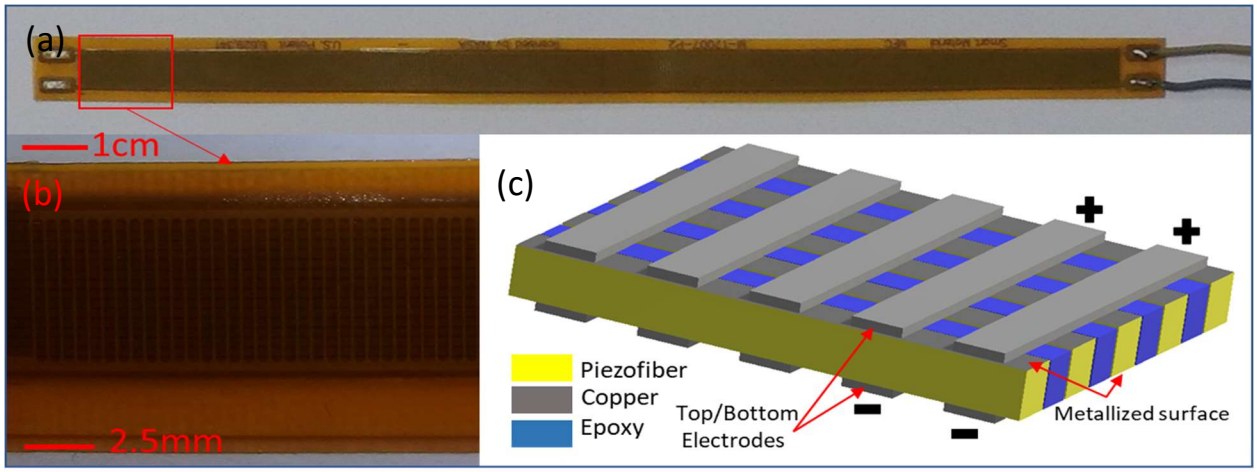

Figure.45. **The proposed OWEC with The P2-Type MFC, M17007-P2 Model.** (a) The P2-Type MFC module, which uses the d_{31} piezo index. (b) The magnified image of MFC. The top electrode and the fibers can be seen clearly. (c) The schematic details of MFC are depicted. The bottom-top electrodes, together with top/bottom surface metallization of the Piezofibers, form the internal connections of the MFC. The bottom-top electrodes configuration helps the P2-type MFCs to collect more charges in comparison with the P1-type MFCs, which have interdigital electrodes.

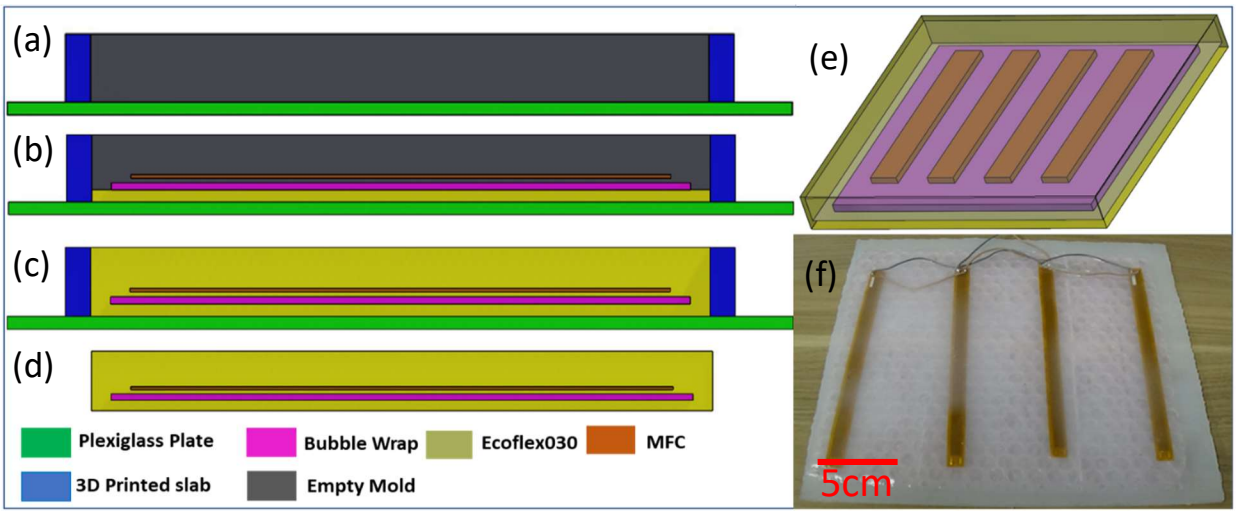

Figure.46. **The Fabrication steps, the schematic, and the photo image of OWEC**. (a) The empty mold. (b) Dispensed a thin layer of Ecoflex in the mold and place the bubble wrap and MFC on this layer. (c) Dispensing Ecoflex on the MFCs and bubble wrap and fill the mold. (d) The cured Ecoflex and the finalized OWEC. (e) The 3D schematic of OWEC. The bubble wrap and the MFCs can be seen clearly. (f) The photo image of the final OWEC.

3-3-Experiment

3-3-1- Rectifier Circuit and Measurement

Wave energy converters had to be connected to a full-wave rectifier to convert their output voltage to a DC voltage, which is easily measurable and comparable [65]. 1N4001 diodes alongside a tantalum 4.7µF capacitor shaped the full-wave rectifier, and a 100 kΩ resistor with a nominal resistivity of 99.3kΩ was used as a load for power measurements as shown in figure 47(a). The resistor had to be switched in the circuit when the loaded energy converters had to be studied. Moreover, figure 47(b) shows the photo image of the power measurement circuit. The output DC voltages were measured by using the Texas Instrument Data Acquisition (DAQ) unit and analyzed.

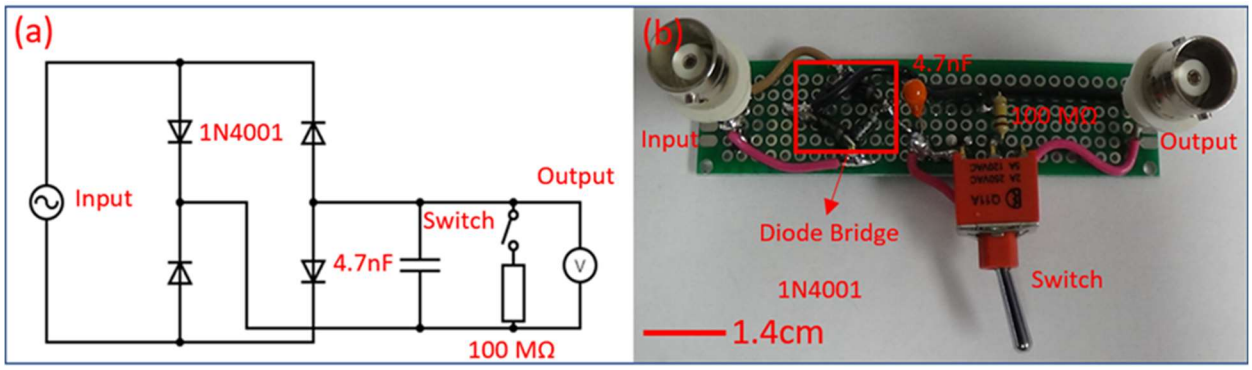

Figure.47. **The schematic diagram of the rectifier circuit and the photo image of the real circuit.** (a) The schematic diagram of the rectifier circuit and the values of the elements. (b) The photo image of the real circuit.

3-3-2-Vertical Anchoring Configuration

In this step, WECs were studied after vertical placement in a wave flume tank. This step was performed to validate the ability of the WECs to convert water wave vibration to electrical energy. In this research, clamps have been used to hold the WEC in a vertical curtain-like position and easily adjust its submerging depth. In figure 48, the clamping situation for curtain-like configuration and a real sample is shown. Also, the bending degree of the device is depicted in this figure. By using the side view, camera recording, and graphical analyses the bendability of the WECs can be determined.

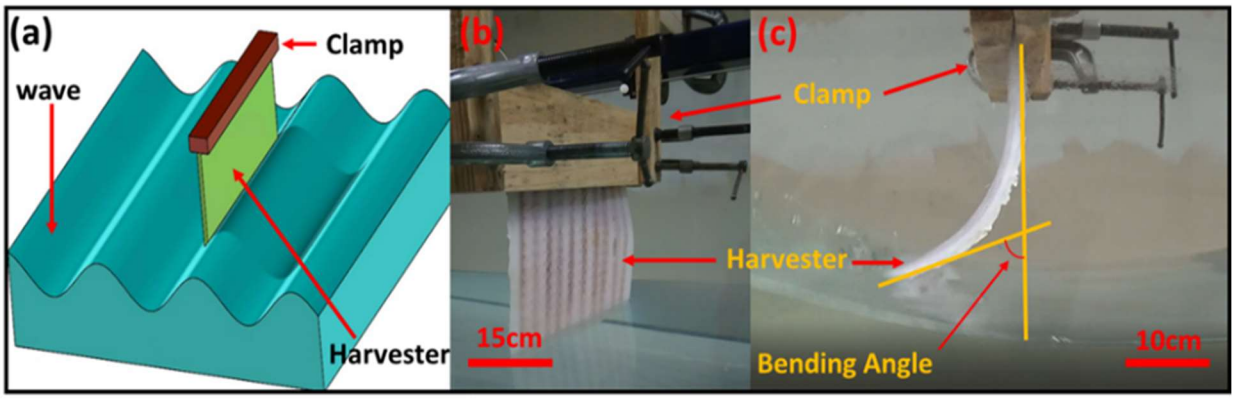

Figure.48. **Placing an OWEC in the flume in a curtain-like (Vertical) configuration** (a) The schematic of the WEC (harvester) placed in a curtain-like configuration and the clamp. (b) The bird view of the clamp and the WEC (harvester) (c) The side view of the WEC in the curtain-like position. The bending angle is also depicted.

The wave amplitude was kept as 8cm with an 80cm wavelength and a 0.7sec period. The submerged depths of harvesters in this experiment were 2, 5, 6.5, 9.2, 12.5, and 14 cm. Also, harvesters with 3 and 10MFCs were prepared for the same incoming water wave conditions. As can be seen in figure 49(a), the range of open-circuit voltage is varied from 1.2 V to 1.75 V DC for 3MFC-based harvesters and 1V to 2.93 V DC for 10MFC-based harvesters. To measure the average delivered power to the resistive load, the voltage on the load measured with the same equipment and the power was calculated from the equation (1) here:

$$P=V^2/R \qquad (3.1)$$

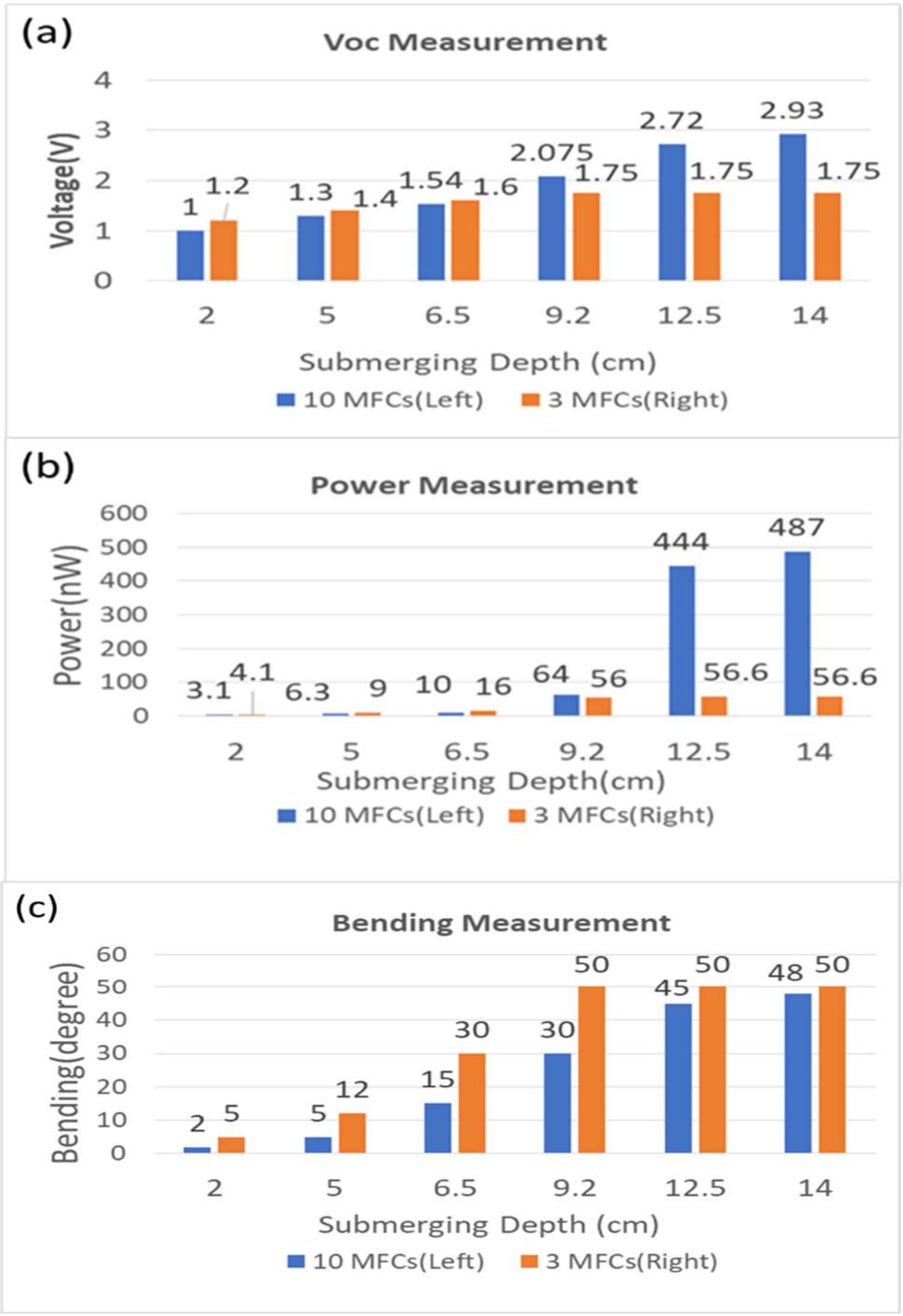

Figure.49. **Vertical OWECs Measurement Results**. The experiments were done under varying submerging depth in the range of 2-14cm. The open-circuit voltage was measured with the TI DAQ system directly after the capacitor. For power measurement, a 99.3kΩ load was added to the output. The bending angle was measured by using a camera. (a)The power measurement. (b)The Voc measurement. (c)The bending angle measurement. Reprinted from[66].

The range of average delivered power to the resistor was 2.4 nW to 56.6 nW for 3MFCs and 3.1 nW to 487nW for 10MFCs is depicted in Fig. 49(b). In addition, results for bending angles of OWECs with different depths are observed by video camera and shown in figure 4(c). It can be seen here that the bending angle of the harvesters are higher with fewer MFCs.

The data shows in figure 49(a,b) that the OWECs with 3MFCs can produce more Voc and power at the depths of 2, 5 and 6.5 cm, while harvesters with 10MFCs can provide more Voc and power at 9.2, 12.5, and 14 cm depths. As mentioned previously, more MFCs in parallel have more capacity to harvest energy and should provide more harvested energy at the same bending angle. At the same time, the higher number of MFCs makes it more difficult for the designed harvester to be bent. While the shear modulus of Ecoflex 030 is 22.081 KPa, it is 5.515 GPa for MFC structures that are made from various elements like Kapton films, aluminum electrodes, and PZT fibers as shown in figure 45 [52-54]. More MFCs in the harvester will increase the rigidity, and it will need higher force to be bent as much as one with fewer MFCs.

The overall capacitance of the connected MFCs was measured before and after the experiments. The capacitance for 10MFCs in parallel stayed at 850nF while the total capacitance for 3MFCs was fixed at 270nF. Also, the proposed WEC could produce power continuously for more than 170 hours in the water, did around 300 successive tests, and had more than 27000 cycles; no measurable deterioration was observed. So, it can be considered a stable OWEC with durable and reliable encapsulation of the electrical components in a soft material structure for vertical OWEC experiment[66].

3-3-3-Horizontal Floating Configuration

The OWECs were placed horizontally on the surface of water in the wave flume as shown in figure 50. In this floating configuration, OWECs were connected with the suspended ropes to the walls of the flume to avoid drifting by waves. In figure 6, the schematic diagram of a wave energy converter, its qualitative response to the wave, and photo images of a floating device are depicted. Figure 50(a) shows the schematic diagram of a horizontally floating OWEC in the wave flume in a still water condition. Figure 50(d) shows the photo image of this situation. In figure 50(b), the schematic diagram of the floating OWEC is depicted on the convex surface of the wave, while figure 50(e) shows the equivalent photo image. Similarly, figure 50(c) shows the schematic diagram of the OWEC on the concave surface of water, while figure 50(f) is an equivalent photo image.

In the flume tests, the tested wave periods of the monochromatic waves were 0.75, 1, 1.25, and 1.5 seconds while the nominal wave heights for each period were 20, 15, 10, and 5 centimeters. The detailed real and nominal wave conditions were detailed in table 1. This table also depicts the steepness of each wave condition (the ratio of the wave height H to the wavelength L). In figure 51, the steepness variation of the incoming waves is shown for each wave period and each nominal wave height. As shown in figure 51(a), the steepness of the wave is increased by increasing wave height for each wave period. While in figure 51(b), it is shown that the steepness is decreased by increasing the wave period. Some wave conditions were avoided in the experiment, as shown in figure 51 and table 1, to prevent wave breaking in the flume. Wave breaking could cause harmonics and standing wave production in the flume, rendering

different wave heights and frequencies. These breaking wave occurrences and their production of unwanted waves can contaminate the results and cause invalid tests.

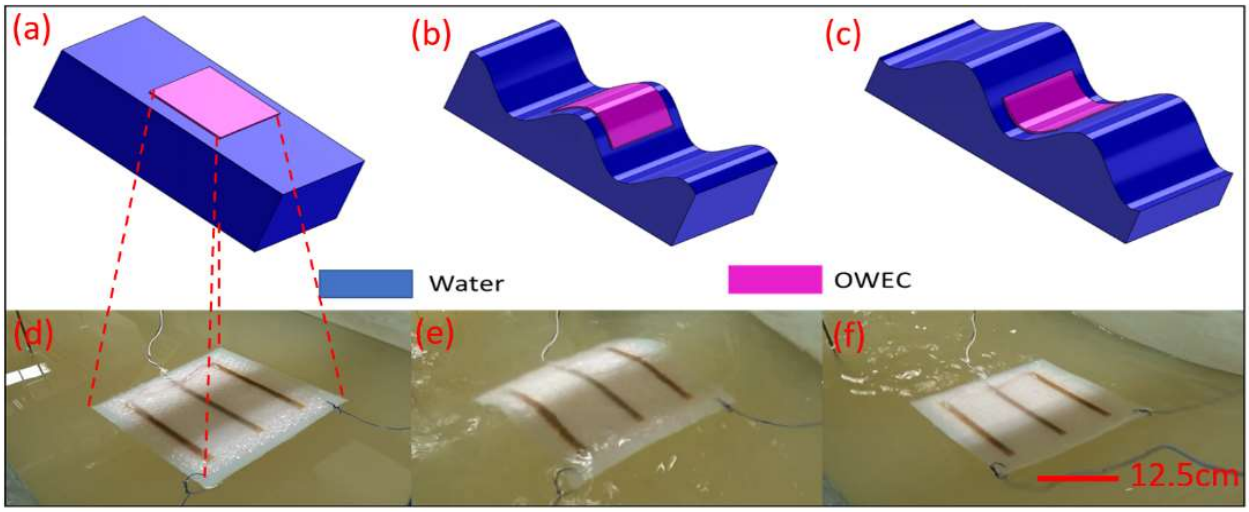

Figure.50. **The wave energy converter and its mechanical behavior**. (a,b,c) Schematics of the OWEC on the water surface following the surface profile of the water waves. (d,e,f) Photo images of the OWEC on the water surface and its responses to the wave motion by following the surface profile.

Table 1**. The details of wave conditions**. The nominal and measured parameters of waves are depicted in this table. The water depth was fixed at h = 97 cm throughout the tests. (a) The Wave Periods are determined precisely by the period of the paddle in the wave flume. (b) Nominal wave heights are chosen and entered as the required heights to the LabVIEW program. (c) The measured wave height H is the real wave height measured by wave probes. (d) The wavelength L is determined by the wave dispersion relationship [67]. (e) The wave steepness (H/L) is the quotient of measured wave height to wavelength. Note that "NA" indicates the wave parameter is not well defined because of wave breaking and the subsequent harmonics generation.

(a) Wave's Period (Sec)	(b) Nominal Wave's Height (cm)	(c) Measured Wave's Height H (cm)	(d) Wave's length L (cm)	(e) Wave's Steepness (H/L)
0.75	20	20	88	0.227
0.75	15	15	88	0.170
0.75	10	11.1	88	0.130
0.75	5	6.1	88	0.068
1.0	20	30.6	156	0.192
1.0	15	24.6	156	0.160
1.0	10	16.8	156	0.109
1.0	5	8.6	156	0.057
1.25	20	NA	NA	NA
1.25	15	30.3	241	0.125
1.25	10	20.5	241	0.085
1.25	5	10.5	241	0.044
1.5	20	NA	NA	NA
1.5	15	NA	NA	NA
1.5	10	23.3	335	0.070
1.5	5	11.8	335	0.035

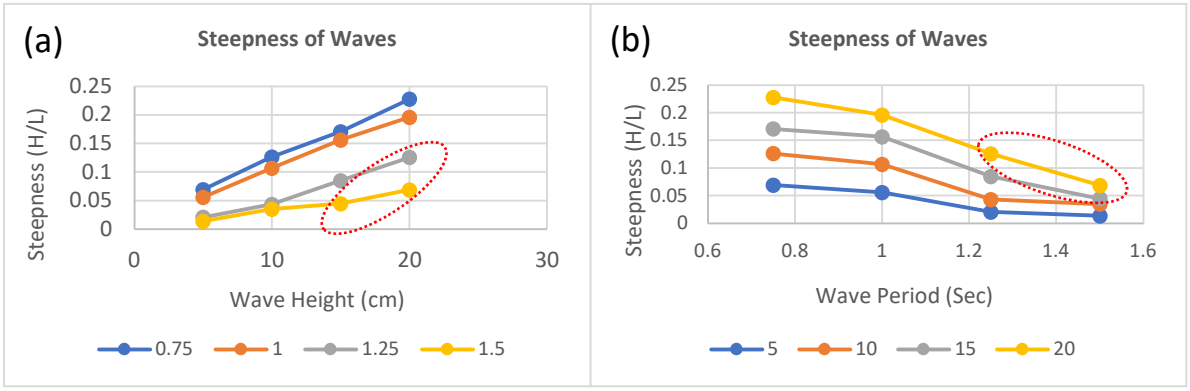

Figure.51. **The steepness of water waves.** (a) The diagram shows the steepness variation versus wave height for a given wave period. (b) The diagram shows the steepness variation versus wave period for a given wave height. Note that the conditions in the elliptical contours are neglected because of waves breaking.

The open-circuit voltage (V_{OC}) and the power delivered to the resistive load (P_{OUT}) are analyzed and investigated. We have investigated the output powers and experimental parameters such as the number of MFCs inside the OWECs, the wave period, the wave height, and the wave steepness in the flume.

As discussed in [66], the output voltage and power from the combined MFCs are proportional to the bending angle, speed, and acceleration. The shear modulus of Ecoflex and M17007-P2 MFC are 22.081 kPa and 5.515 GPa, respectively. The stiffness of the OWECs varies by the number of the integrated MFCs, which is a critical parameter to determine the vibration modes and bendability of OWEC. Based on this discovery, there is always a trade-off between the bendability of the OWEC and its competence for energy harvesting. Because OWECs in this study follow the surface profile of the waves, higher output voltage and power are expected from a steeper wave.

In figure 52, each graph shows the variation of the V_{OC} or P_{OUT} as a function of a specific wave period and various wave heights. The number of MFCs is considered as a parameter in each graph. Here's a breakdown of the test conditions represented in each graph: 0.75 Sec wave period and 5, 10, 15, and 20 cm wave heights V_{OC} and P_{OUT}, in figures 52(a) and 52(b); 1 Sec wave period and 5, 10, 15, and 20 cm wave heights V_{OC} and P_{OUT}, in figures 52(c) and 52(d); 1.25 Sec wave period and 5, 10, and 15 wave heights V_{OC} and P_{OUT}, in figures 52(e) and 52(f); and finally, 1.5 Sec wave period and 5, and 10 cm wave heights V_{OC} and P_{OUT} in 52(g) and 52(h), respectively. As shown in figure 51(a), by increasing the wave height for each wave period the steepness of the wave has increased. Similarly, the V_{OC} and P_{OUT} are following the same pattern, when they are classified for a specific wave period and incremental wave heights. Because of the increment in wave steepness, the steeper waves can bend the OWEC more and produce a higher level of output voltage and power. On the other hand, a larger number of MFCs does not produce a higher V_{OC} or P_{OUT} due to its decreased bendability. As shown in the figure, 3 MFCs seem to be optimal in the tests.

In figure 53, each graph shows the variations of the V_{OC} or P_{OUT} as a function of a specific wave height and different periods. Like figure 8, the number of MFCs is considered as a parameter in each graph. The breakdown of the test conditions represented in each graph is here: 20 cm of wave height and 0.75 and 1sec wave periods V_{OC} and P_{OUT} , in figures 53(a) and 53(b); 15 cm of wave height and 0.75, 1, and 1.25 sec wave periods V_{OC} and P_{OUT} , in figures 53(c) and 53(d); 10 cm of wave height and 0.75, 1, 1.25, and 1.5 sec wave periods V_{OC} and P_{OUT} , in figures 53(e) and 53(f); 5 cm of wave height and 0.75, 1, 1.25, and 1.5 sec wave periods V_{OC} and P_{OUT} , in figures

53(g) and 53(h). Same as Figure 51(b)., by increasing the wave period the steepness of the wave decreased, which caused the same pattern of decrement in V_{OC} and P_{OUT} in figure 53.

In figure 54, the open circuit voltage and output power are shown as a function of the wave steepness. In the figure 54(a), the V_{oc} changes are depicted against various wave steepness. In figure 54(b), the P_{out} variations versus steepness are shown. The outputs are almost monotonically increasing by increasing the wave steepness. The distraction of monolithic behavior of outputs can be due to nonlinearity effects that can shift the output values slightly.

From the results of figures 52, 53, and 54, it is concluded that the OWECs with 3 MFCs have the highest power production for all the wave conditions. The maximum power output of the OWECs with 3 MFCs is a compromise between bendability and power production competence of the OWEC. While the OWECs with 5 MFCs and 10 MFCs have a higher capacity to produce electrical energy, they have a stiffer structure with lower bendability.

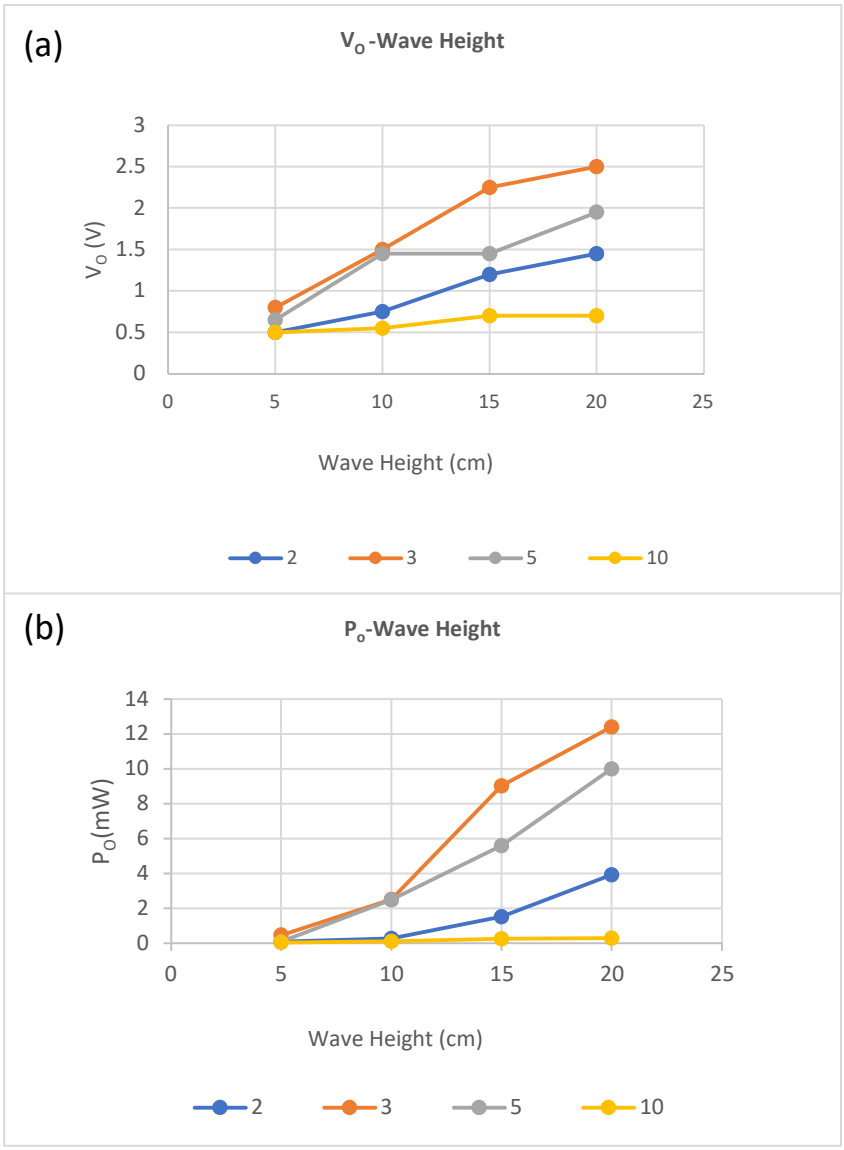

Figure.52. **The graph of V_{OC} and P_{OUT} as a function of a specific wave period and height for a given number of MFCs**. (a,b) V_{OC} and P_{OUT} for 0.75 Sec wave period and 5, 10, 15, and 20 cm wave heights. (c,d) V_{OC} and P_{OUT} for 1 Sec wave period and 5, 10, 15, and 20 cm wave heights (e,f) V_{OC} and P_{OUT} for 1.25 Sec wave period and 5, 10, and 15 cm wave heights (g,h) V_{OC} and P_{OUT} for 1.5 Sec wave period and 5, 10 cm wave heights. The number of MFCs varies from 2, 3, 5, to 10.

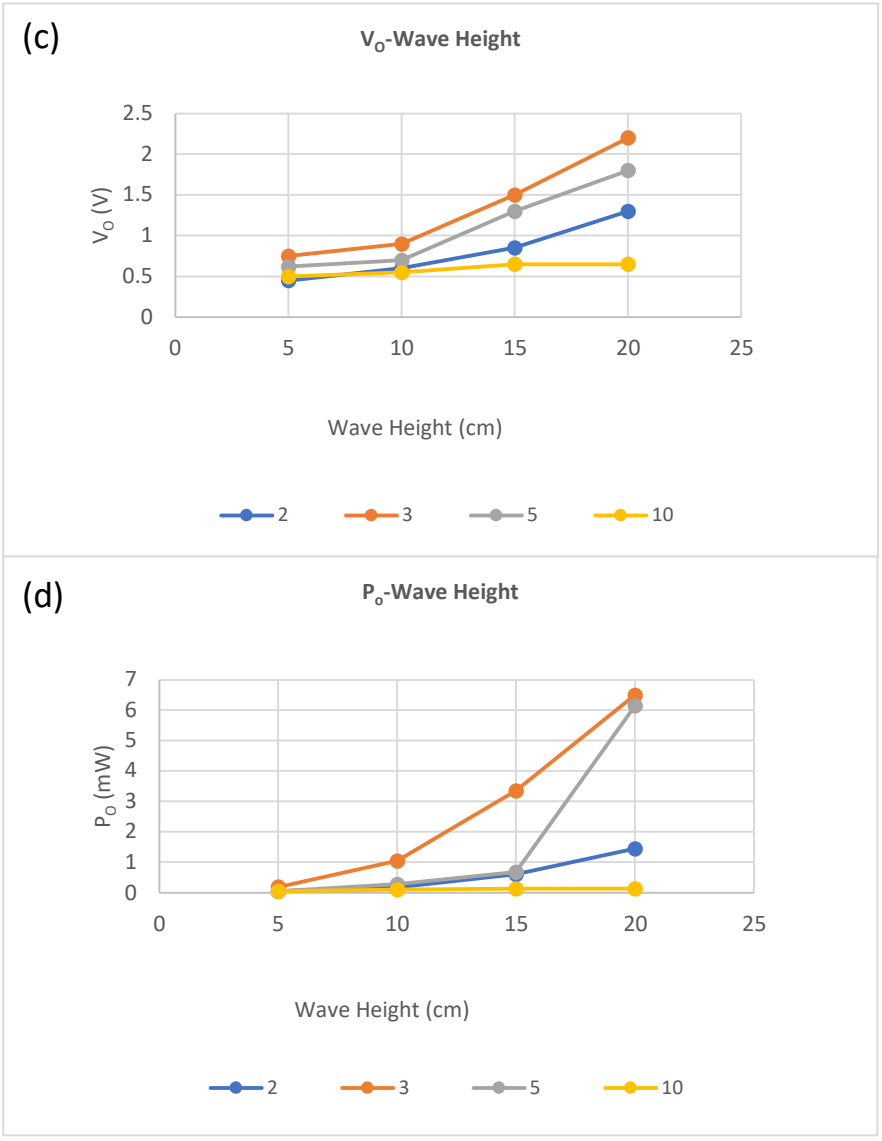

Figure.52. Continued

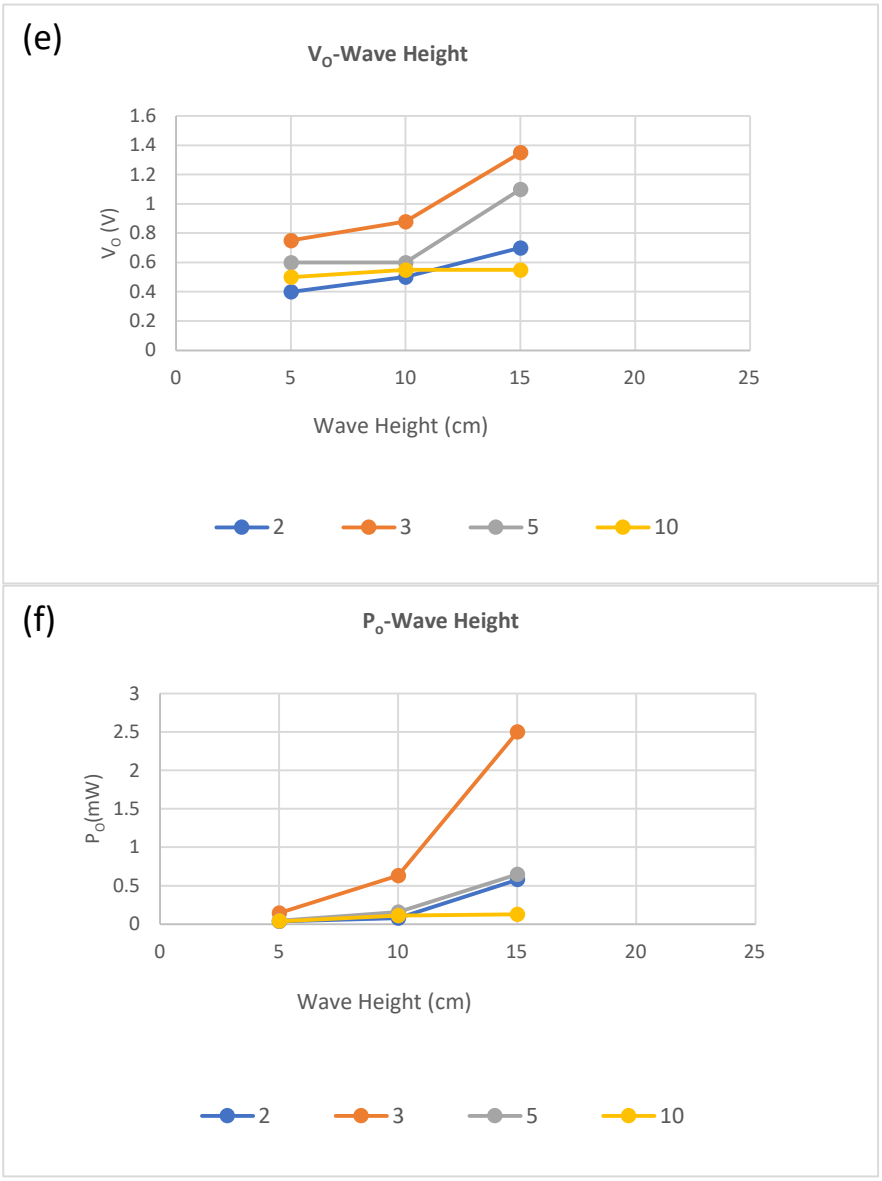

Figure.52. Continued

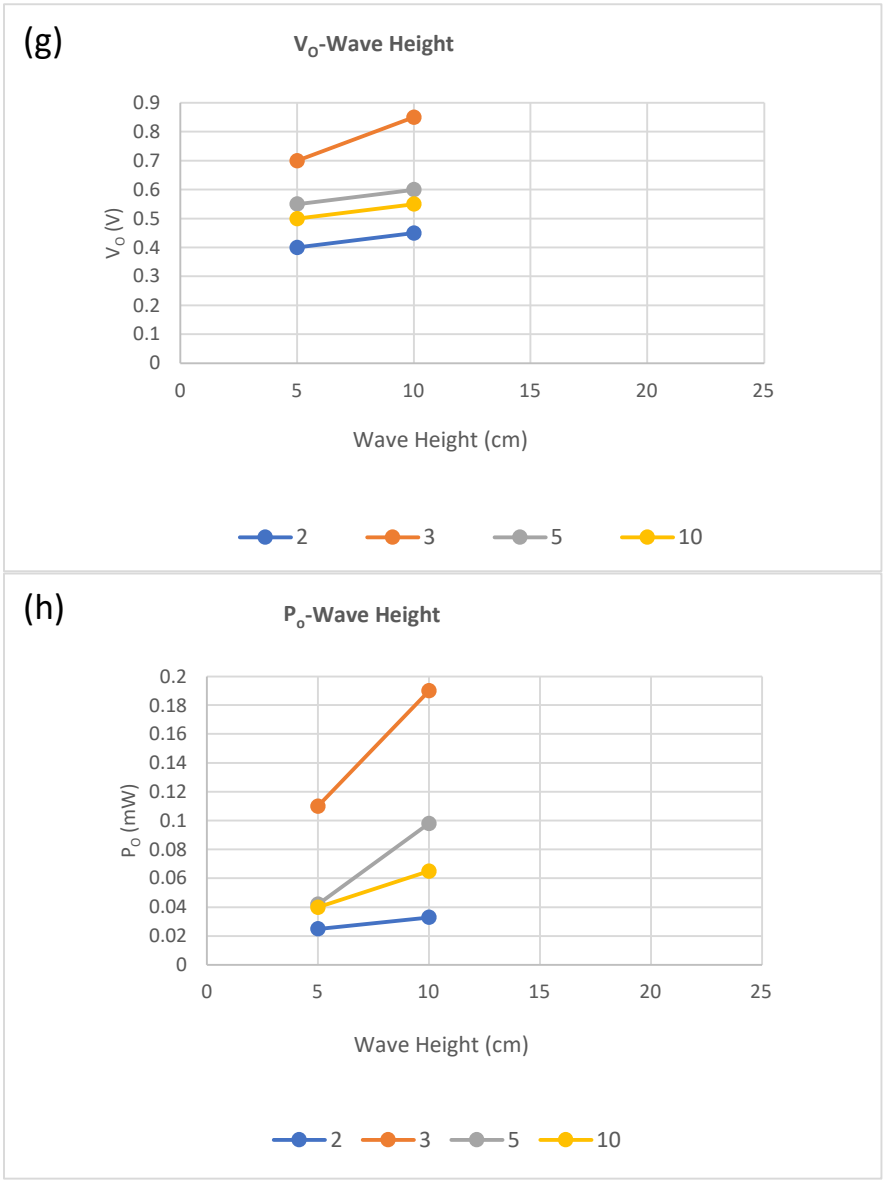

Figure.52. Continued

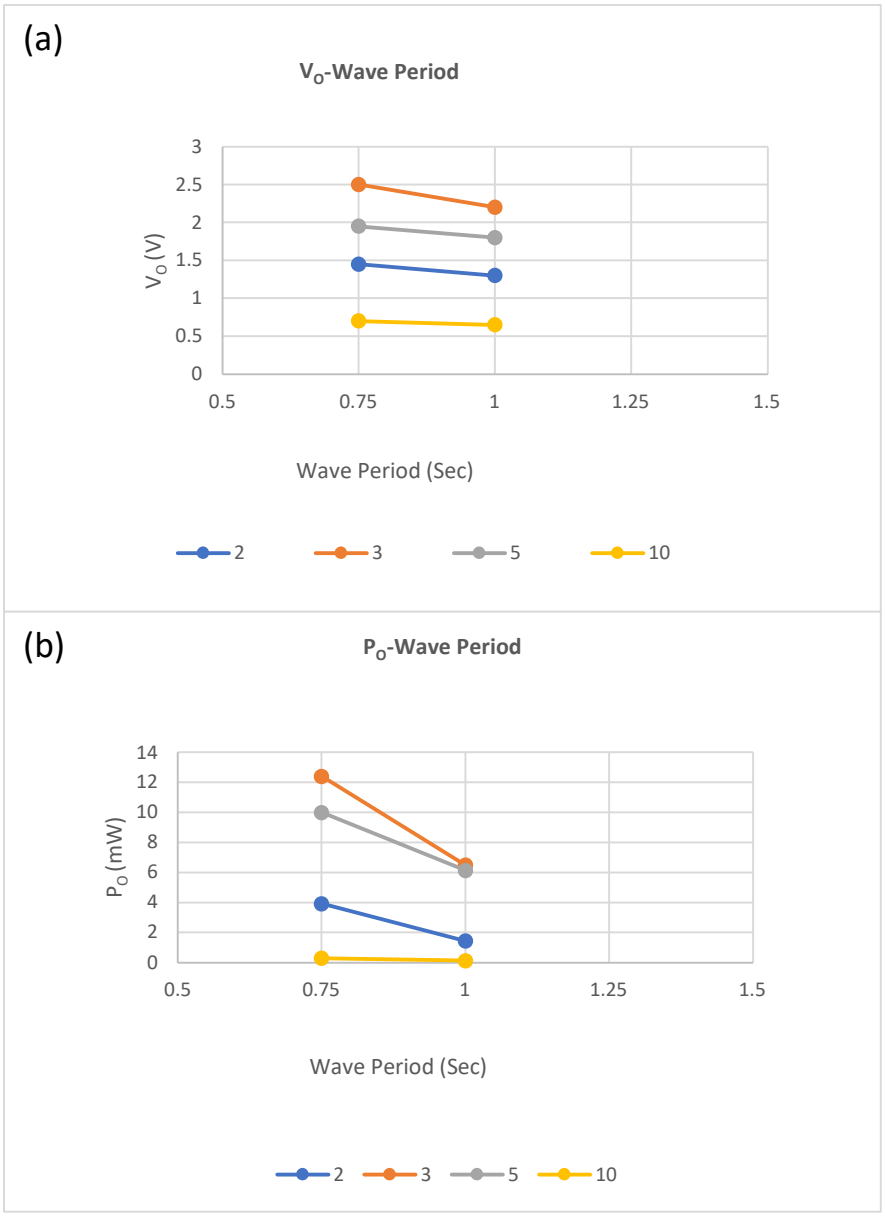

Figure.53. **The graph of V_{OC} and P_{OUT} as a function of a specific wave height and period for a given number of MFCs**. (a,b) Output voltage and power for 20 cm wave height and 0.75 and 1 sec wave periods (c,d) Output voltage and power for 15 cm wave height and 0.75, 1, and 1.25sec wave periods (e,f) Output voltage and power for 10 cm wave height and 0.75, 1, 1.25 and 1.5 sec wave periods (g,h) Output voltage and power for 5 cm wave height and 0.75, 1, 1.25 and 1.5 sec wave periods. The number of MFCs varies from 2, 3, 5, to 10.

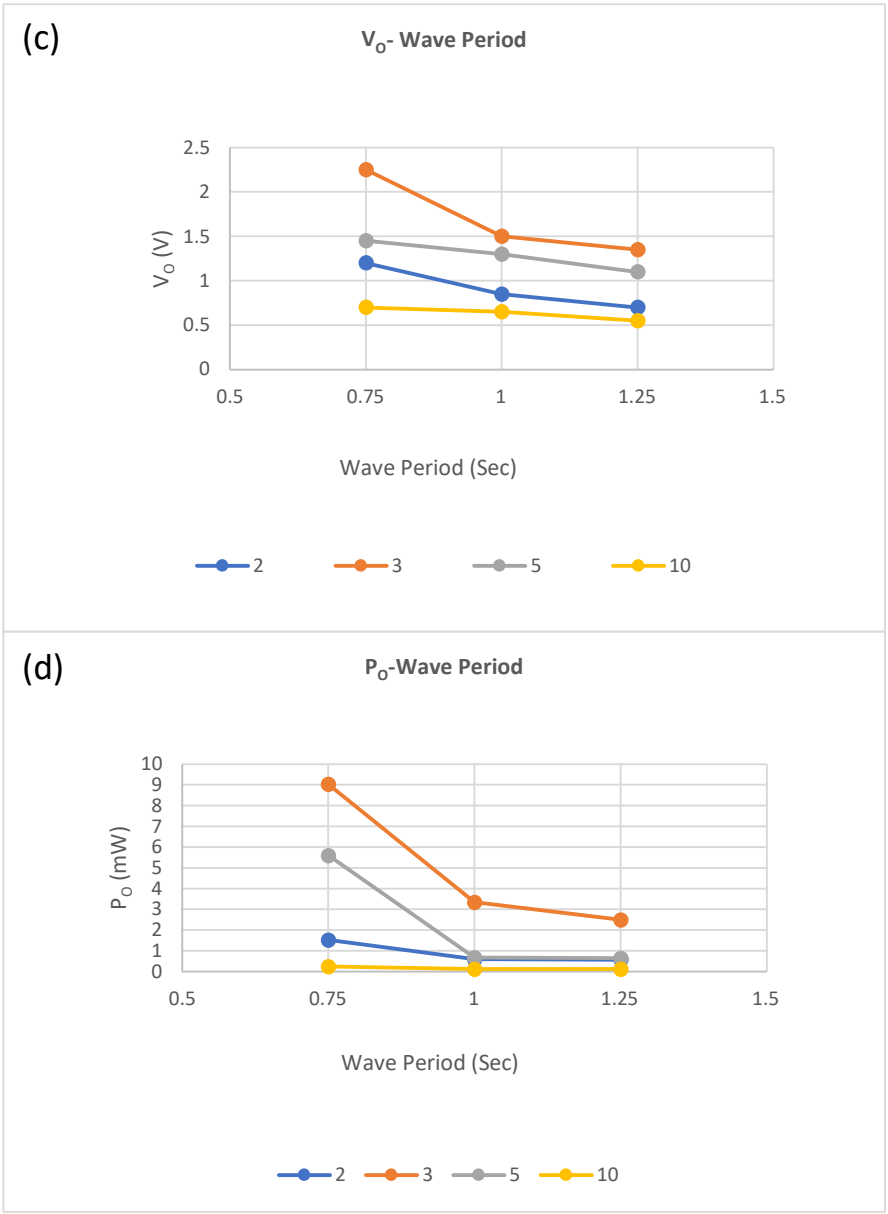

Figure.53. Continued

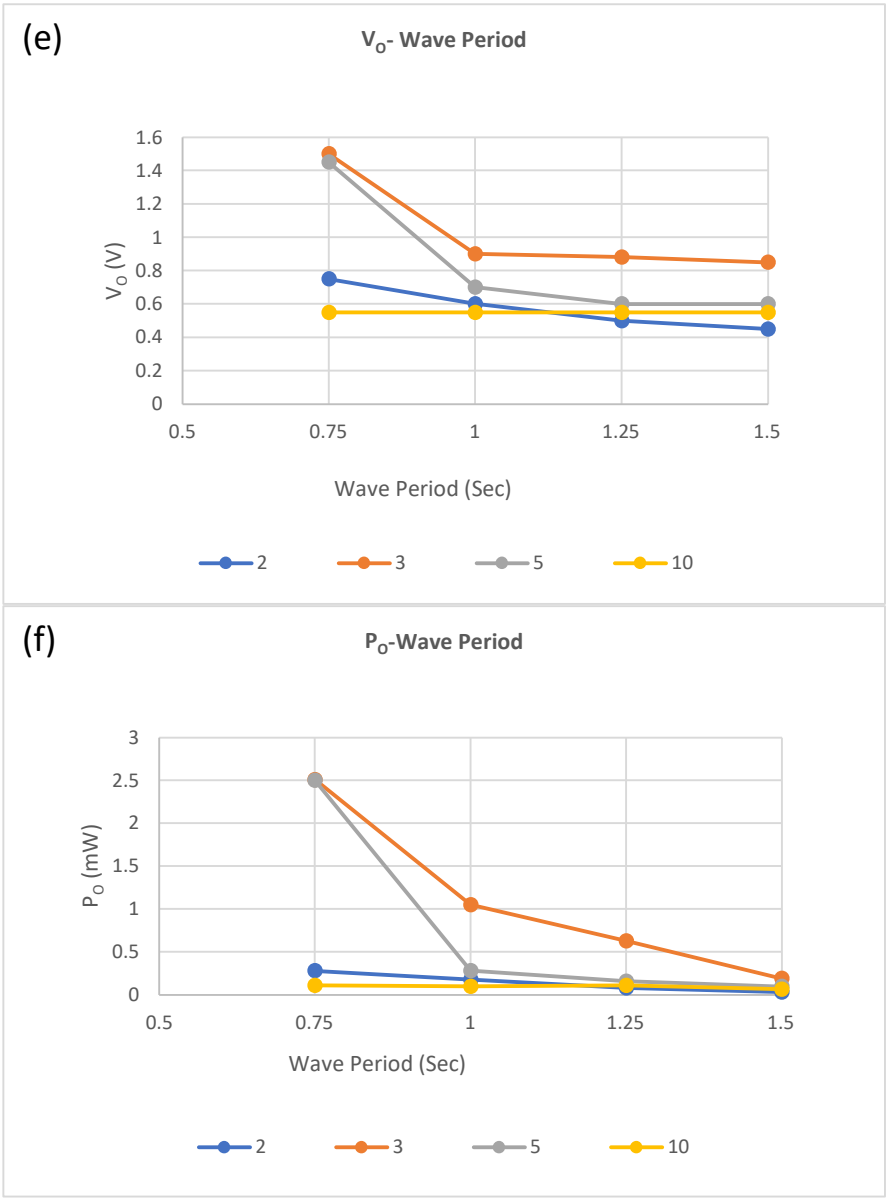

Figure.53. Continued

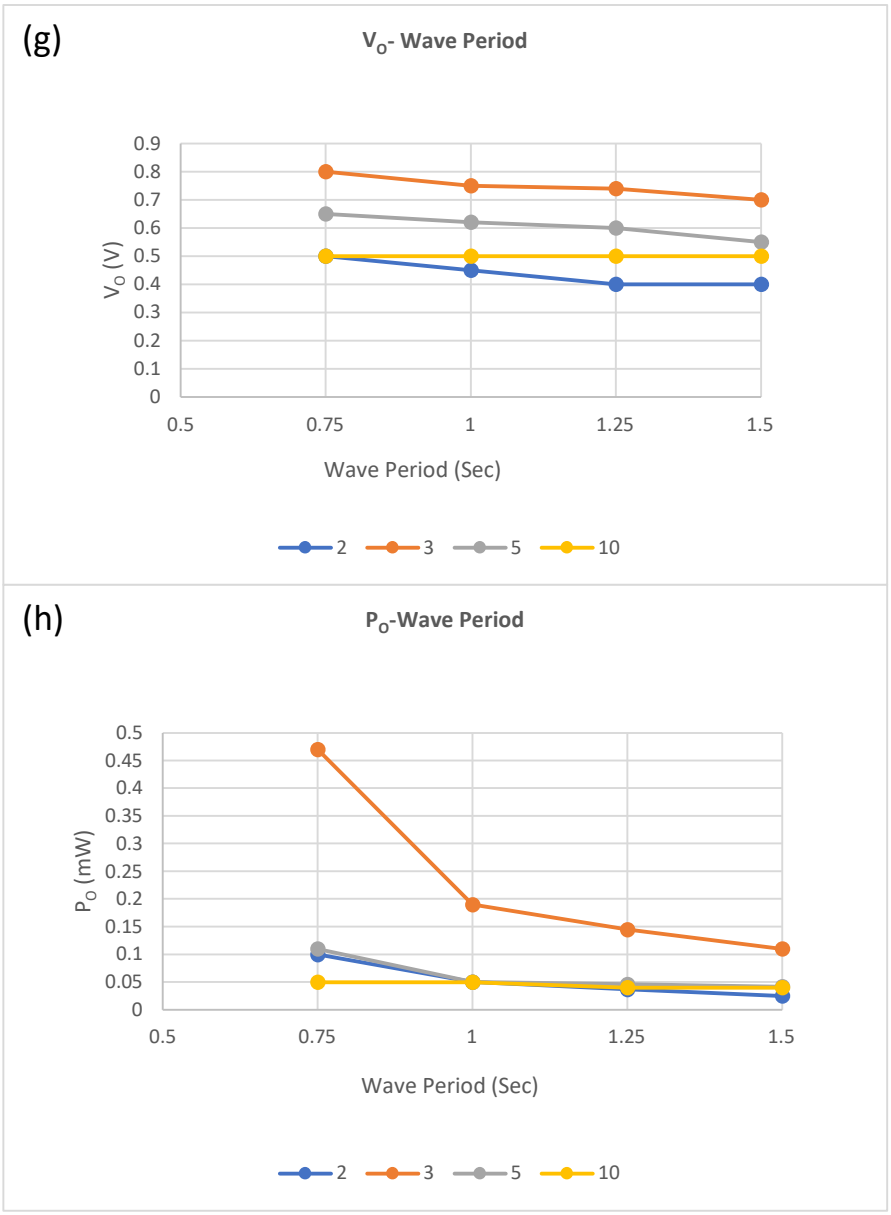

Figure.53. Continued

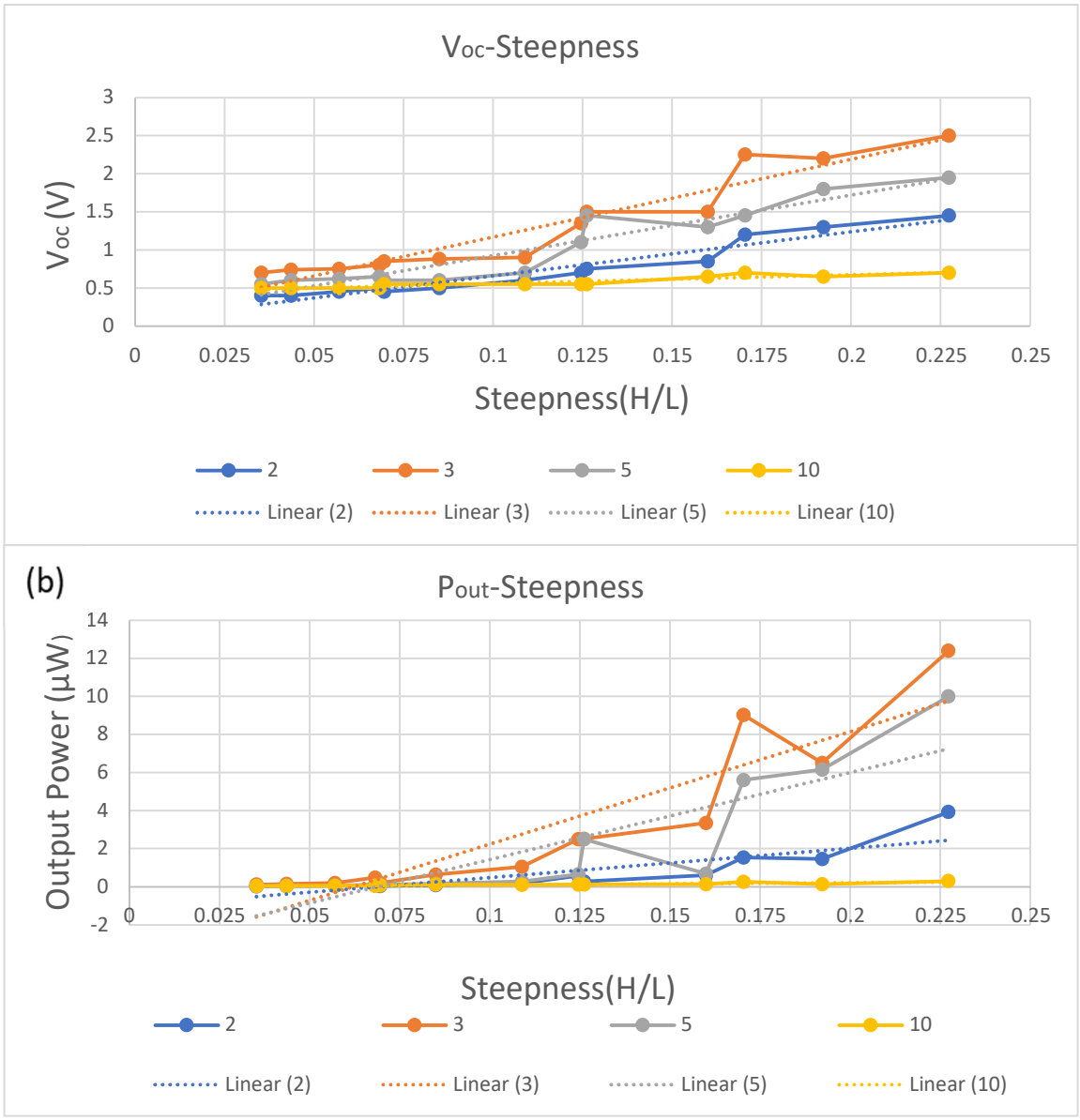

Figure.54. **V_{oc} and P_{out} versus wave steepness for a given number of MFCs**. (a) Output voltage of OWECs with various number of MFCs versus wave steepness (b) Output power of OWECs with various number of MFCs versus wave steepness.

The proper encapsulation of the OWECs is a crucial process to ensure their performance. As the electrical devices working in the highly corrosive saltwater and under the sunshine, the electrical components should be preserved properly to endure the harsh environment. Each MFC

has a capacitance of 93-100nF. The combination of various number of MFCs, internal connections, and wirings can provide different amounts of capacitance for each OWEC. The capacitances are 190 nF, 270 nF, 470 nF, and 850 nF for the OWECs with 2, 3, 5, and 10 MFCs. These capacitances are measured before, during, and after the experiments, and the results of measurements did not show any observable variation. This persisted result proved a stable encapsulation of MFCs in the Ecoflex platform. The output voltage and power also did not have any deterioration which proves the quality of encapsulation and the efficiency of the design. During the tests, the OWECs were exposed to saltwater for 336 hours and tolerated more than 41000 cycles without any negative effect.

3-3-4-One-Sided Anchored Configuration

We have discovered that OWECs with 3 MFCs have the highest power production ability. To study the OWEC anchoring effect on energy production, the OWECs with 3 MFCs were anchored as shown in Figure 55.

The power production was measured for the condition of a wave height of 20 cm and a wave period of 0.75 sec. As shown in figure 52, the OWEC with 3 MFCs in this test condition produced the maximum energy in the free-floating (horizontal unanchored) configuration. Figure 56 depicts the comparison of energy production of OWEC with 3 MFCs in both horizontally unanchored (freely floating) and horizontally one-sided anchored configurations.

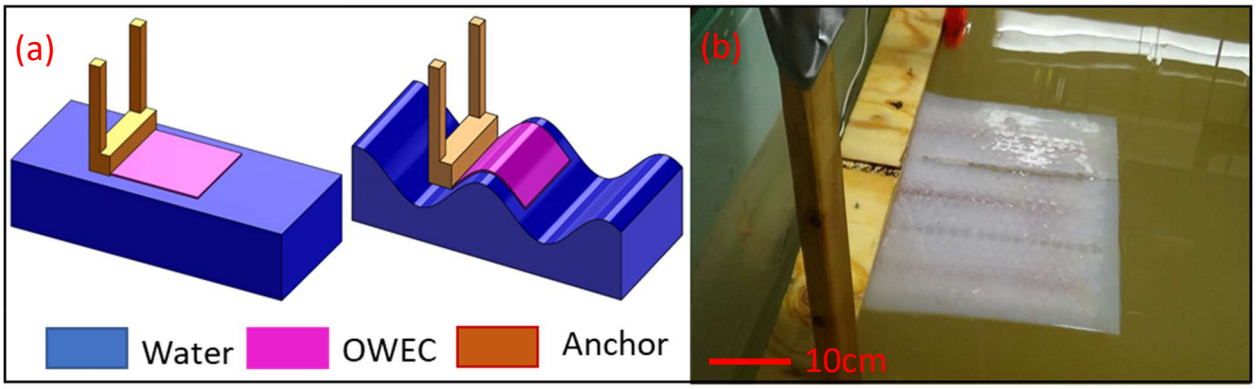

Figure.55. **The horizontal one-sided anchoring**. (a) The schematic of the one-sided anchored OWEC. (b) The photo image of the one-sided anchored OWEC.

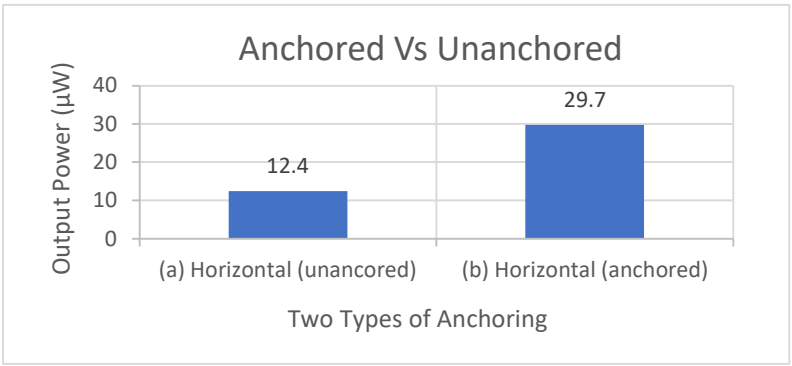

Figure.56. **Comparison of horizontally one-sided anchored OWEC and unanchored free floating OWEC**. (a) The unanchored horizontally placed OWEC. (b) The one-sided horizontally anchored OWEC. It is obvious that the OWEC can harvest remarkably more energy in the one-sided anchored configuration.

As shown in figure 56(a) the maximum output power was 12.4 μW for the free-floating configuration. In the one-side anchoring configuration, figure 56(b) shows the power production increased more than twice to 29.7 μW. So, the one-sided anchoring method remarkably increased the energy harvesting ability of the OWEC. This one-sided anchored configuration may

be especially useful to energize remote sensing applications on offshore structures because it can be anchored on these structures, like what is seen in figure 55.

3-4-Discussion

Energy harvesting from a low-cost and environmentally friendly OWEC has been investigated under various wave conditions in a wave flume. The commercially available MFCs and bubble wrap alongside an uncostly material casting method was used for fabricating the OWEC device. The converter contains multiple MFCs as the piezoelectric conversion element that are encapsulated in a piece of Ecoflex 030 elastomer. This environmental friendly encapsulation, can reduce the hazardous effects of the chemicals in the commercially available water wave conversion systems. Because the designed OWECs do not have any internal moving parts, their maintenance and fabrication cost will be significantly reduced in comparison to other types of OWECs. Furthermore, these OWECs are light-weight and foldable so they may also reduce the deployment cost.

At first, to investigate the conversion performance, OWECs with 3 and 10 MFCs were placed in a vertical curtain-like configuration and studied in the flume. In this step, the relation between bendability, power production ability, and the bending were studied. The harvesters containing 10MFCs in parallel can produce 487nW, while the harvester with 3MFCs can generate 56.6nW under the curtain-like configuration. Energy outputs from the OWECs with 2, 3, 5, and 10 MFCs were investigated in a horizontally floating configuration. The harvester with 3 MFCs demonstrated the highest wave energy conversion in such configuration (12.1µW, on its peak), while the harvester containing 10 MFCs demonstrated the lowest production (0.3µW, on its

peak). The energy harvester with 3 MFC was also investigated under a one-sided horizontal anchoring configuration and showed a promising 29.7μW energy harvesting ability. The output voltage and power production demonstrated consistent energy production during the 336-hour long experiment period. The capacitance of each OWEC was stable before, during, and after the experiment, and so as the internal electrical connection.

To use the newly proposed OWEC for real-life applications, there are several paths that have to be followed, depending on different applications. For wave monitoring and remote sensing, the introduced OWEC can be used in the current form on offshore structures or be moored on the open water's surface. The harvested energy can be used for driving sensors and communication purposes, while the OWEC can be used as a self-energized sensor itself. For Large scale energy harvesting, this proposed scalable OWEC should be fabricated at larger dimensions, featuring the same thickness but a much larger surface area. One of the limitations of scaling up this proposed OWEC is the limited size of commercialized MFCs, which is limited by the length of piezofibers and fabrication limitations. Even so, integrating a higher number of commercialized small MFCs into a big sheet of soft material and connecting them in a proper circuit configuration may still be a feasible method to scale up energy harvesting from the OWEC. The foldable nature of the introduced OWEC structure can also reduce the deployment costs remarkably. While the reported information in this article can be useful for effective scaling up of the OWEC with proper stiffness, bendability, and power production capacity, further characterization should be performed to achieve more efficient OWECs for larger-scale energy productions. While the hydrodynamic studies about the harvester/wave mutual effects have not been investigated, we will further investigate their relations in future research.

3-5-Bibliography

1) Maria Mayara de Souza Grilo, Anderson Felipe Chaves Fortes, Raoni Pinheiro Gonzaga de Souza, Ju'lio Augusto Mendes Silva, and Monica Carvalho "Carbon footprints for the supply of electricity to a heat pump: Solar energy vs electric grid," *J. Renew. Sustain. Energy, vol. 10, no. 2, pp. 1–9, 2018, doi: 10.1063/1.4997306.*

2) A.McCrone, U.Moslener, F.d'Estais, C.Grüning "Global Trends in Renewable Energy Investment 2018" Frankfurt School-UNEP Centre/BNEF. 2018, http://www.fs-unep-centre.org.

3) D. Keček, D. Mikulić, and Ž. Lovrinčević, "Deployment of renewable energy : Economic effects on the Croatian economy," *Energy Policy*, vol. 126, no. November 2018, pp. 402–410, 2019, doi: 10.1016/j.enpol.2018.11.028.

4) T. Bauwens, "Analyzing the determinants of the size of investments by community renewable energy members : Findings and policy implications from Flanders," *Energy Policy*, vol. 129, no. March, pp. 841–852, 2019, doi: 10.1016/j.enpol.2019.02.067.

5) K. S. Herman, "Attracting Foreign Direct Investment: The Chilean Government ' s Role Promoting Renewable Energy," in *International Conference on Renewable Energy Research and Applications*, 2013, no. October, pp. 20–23, doi: 10.1109/ICRERA.2013.6749722.

6) A.A. Romano, G.Scandurra, "Investments in Renewable Energy Sources in OPEC Members: a Dynamic Panel Approach" Metodološki zvezki, Vol. 11, No. 2, 2014, pp. 93-106.

7) S.Ntanos, M.Skordoulis , G.Kyriakopoulos,G.Arabatzis, M.Chalikias, S.Galatsidas, A.Batzios, and A.Katsarou “Renewable Energy and Economic Growth: Evidence from European Countries” Sustainability 2018, 10, 2626; doi:10.3390/su10082626.

8) Y. Choi, C. Lee, and J. Song, “Review of Renewable Energy Technologies Utilized in the Oil and Gas Industry,” *Int. J. Renew. ENERGY Res.*, vol. 7, no. 2, pp. 592–598, 2017.

9 H. Saadawi, “Application of Renewable Energy in the Oil and Gas Industry,” in *SPE Middle East Oil and Gas Show and Conference*, 2019, no. March, pp. 18–21, doi: 10.2118/194972-MS.

10) M. Khazaee, A. Rezaniakolaie, A. Moosavian, and L. Rosendahl, “A novel method for autonomous remote condition monitoring of rotating machines using piezoelectric energy harvesting approach,” *Sensors Actuators, A Phys.*, vol. 295, pp. 37–50, Aug. 2019, doi: 10.1016/j.sna.2019.05.016.

11) S. Malinchik, C. Hill, A. Roerts, and S. Fierro, “Geo-Spatial Resource Analysis and Optimization of Investment Strategies for Renewable Energy,” in *2010 IEEE Conference on Innovative Technologies for an Efficient and Reliable Electricity Supply*, 2010, pp. 70–77, doi: 10.1109/CITRES.2010.5619855.

12) Z. Yang, S. Zhou, J. Zu, and D. Inman, “High-Performance Piezoelectric Energy Harvesters and Their Applications,” *Joule*, vol. 2, no. 4, pp. 642–697, 2018, doi: 10.1016/j.joule.2018.03.011.

13) S. Roy, D. Mallick, and K. Paul, “MEMS-Based Vibrational Energy Harvesting and Conversion Employing Micro- / Nano-Magnetics,” *IEEE Trans. Magn.*, vol. 55, no. 7, pp. 1–15, 2019, doi: 10.1109/TMAG.2019.2896105.

14) A. Moure *et al.*, “Feasible integration in asphalt of piezoelectric cymbals for vibration energy harvesting,” *Energy Convers. Manag.*, vol. 112, pp. 246–253, 2016, doi: 10.1016/j.enconman.2016.01.030.

15) C. V. C. Weiss, R. Guanche, B. Ondiviela, O. F. Castellanos, and J. Juanes, “Marine renewable energy potential: A global perspective for offshore wind and wave exploitation,” *Energy Convers. Manag.*, vol. 177, no. September, pp. 43–54, 2018, doi: 10.1016/j.enconman.2018.09.059.

16) L. B. Zhang, H. L. Dai, Y. W. Yang, and L. Wang, “Design of high-efficiency electromagnetic energy harvester based on a rolling magnet,” *Energy Convers. Manag.*, vol. 185, no. January, pp. 202–210, 2019, doi: 10.1016/j.enconman.2019.01.089.

17) Y. Naito and K. Uenishi, “Electrostatic MEMS Vibration Energy Harvesters inside of Tire Treads,” *Sensors*, vol. 19, no. 4, p. 890, Feb. 2019, doi: 10.3390/s19040890.

18) I. Izadgoshasb, Y. Y. Lim, L. Tang, R. Vasquez Padilla, Z. S. Tang, and M. Sedighi, “Improving efficiency of piezoelectric based energy harvesting from human motions using double pendulum system,” *Energy Convers. Manag.*, vol. 184, no. November 2018, pp. 559–570, 2019, doi: 10.1016/j.enconman.2019.02.001

19) Z. L. Wang, T. Jiang, and L. Xu, “Toward the blue energy dream by triboelectric nanogenerator networks,” *Nano Energy*, vol. 39, no. June, pp. 9–23, 2017, doi: 10.1016/j.nanoen.2017.06.035.

20) T. Aderinto and H. Li, “Review on Power Performance and Efficiency of Wave Energy Converters,” *energies*, vol. 12, no. 22, 2019, doi: 10.3390/en12224329.

21) A. Sharon, J. Briggs, and H. Wirz, “Mobile Wave Energy Harvesting System,” in *NSTI-Nanotech 2011*, 2011, vol. 3, pp. 683–686.

22) R. Song, M. Zhang, X. Qian, X. Wang, and Y. M. Dai, “A Floating Ocean Energy Conversion Device and Numerical Study on Buoy Shape and Performance,” *J. Mar. Sci. Eng.*, vol. 4, no. 35, pp. 1–14, 2016, doi: 10.3390/jmse4020035.

23) A. Uihlein and D. Magagna, “Wave and tidal current energy – A review of the current state of research beyond technology,” *Renew. Sustain. Energy Rev.*, vol. 58, pp. 1070–1081, 2016, doi: 10.1016/j.rser.2015.12.284.

24) C. Frid *et al.*, “The environmental interactions of tidal and wave energy generation devices,” *Environ. Impact Assess. Rev.*, vol. 32, no. 1, pp. 133–139, 2012, doi: 10.1016/j.eiar.2011.06.002.

25) D.Spreemann, Y.Manoli, “Electromagnetic Vibration Energy Harvesting Devices: Architectures, Design, Modeling, and Optimization” Springer Series in Advanced Microelectronics, 35, Feb 15, 2012 , pp. 1-198, doi: 10.1007/978-94-007-2944-5.

26) C. Wei and X. Jing, “A comprehensive review on vibration energy harvesting : Modelling and realization,” *Renew. Sustain. Energy Rev.*, vol. 74, no. February, pp. 1–18, 2017, doi: 10.1016/j.rser.2017.01.073.

27) I. Izadgoshasb, Y. Y. Lim, R. V. Padilla, M. Sedighi, and J. P. Novak, “Performance Enhancement of a Multiresonant Piezoelectric Energy Harvester for Low,” *energies*, vol. 12, no. July, pp. 1–9, 2019, doi: 10.3390/en12142770.

28) Y. Wada, Y. Hamate, S. Nagasawa, and H. Kuwano, “AGING CHARACTERISTICS OF ELECTRET USED IN A VIBRATION-BASED ELECTROSTATIC INDUCTION ENERGY HARVESTER,” in *2011 16th International Solid-State Sensors, Actuators and Microsystems Conference*, 2011, vol. 1, pp. 2626–2629, doi: 10.1109/TRANSDUCERS.2011.5969869.

29) J. Peng, S. D. Kang, and G. J. Snyder, “Optimization principles and the figure of merit for triboelectric generators,” *Sci. Adv.*, vol. 3, no. 12, pp. 1–6, 2017, doi: 10.1126/sciadv.aap8576.

30) S. Mishra, L. Unnikrishnan, S. K. Nayak, and S. Mohanty, “Advances in Piezoelectric Polymer Composites for Energy Harvesting Applications : A Systematic Review,” *Macromol. Mater. Eng.*, vol. 1800463, no. 304, pp. 1–25, 2019, doi: 10.1002/mame.201800463.

31) Y. Sun, J. Chen, X. Li, Y. Lu, S. Zhang, and Z. Cheng, “Flexible piezoelectric energy harvester / sensor with high voltage output over wide temperature range,” *Nano Energy*, vol. 61, no. April, pp. 337–345, 2019, doi: 10.1016/j.nanoen.2019.04.055.

32) R. Caliò *et al.*, “Piezoelectric Energy Harvesting Solutions,” *Sensors*, vol. 14, pp. 4755–4790, 2014, doi: 10.3390/s140304755.

33) E. S. Leland, J. Baker, E. Reilly, B. Otis, J. M. Rabaey, and P. K. Wright, “Improving power output for vibration-based energy scavengers,” *Pervasive Comput.*, vol. 4, no. 1, pp. 28–36, doi: 10.1109/MPRV.2005.14.

34) A. C. Turkmen and C. Celik, “Energy harvesting with the piezoelectric material integrated shoe,” *Energy*, vol. 150, pp. 556–564, 2018, doi: 10.1016/j.energy.2017.12.159.

35) G. Zhang, S. Gao, and H. Liu, “A utility piezoelectric energy harvester with low frequency and high-output voltage : Theoretical model , experimental verification and energy storage,” *AIP Adv.*, vol. 6, no. 9, pp. 1–17, 2016, doi: 10.1063/1.4962979.

36) Z. Yang, S. Zhou, J. Zu, and D. Inman, “High-Performance Piezoelectric Energy Harvesters and Their Applications,” *Joule*, vol. 2, no. 4, pp. 642–697, 2018, doi: 10.1016/j.joule.2018.03.011.

37) S. Xu, B. J. Hansen, and Z. L. Wang, “Piezoelectric-nanowire-enabled power source for driving wireless microelectronics,” *Nat. Commun.*, pp. 1–5, 2010, doi: 10.1038/ncomms1098.

38) M. Rezaei, S. E. Khadem, and P. Firoozy, “Broadband and tunable PZT energy harvesting utilizing local nonlinearity and tip mass effects,” *Int. J. Eng. Sci.*, vol. 118, pp. 1–15, 2017, doi: 10.1016/j.ijengsci.2017.04.001.

39) N. Tran, M. H. Ghayesh, and M. Arjomandi, “Ambient vibration energy harvesters : A review on nonlinear techniques for performance enhancement,” *Int. J. Eng. Sci.*, vol. 127, pp. 162–185, 2018, doi: 10.1016/j.ijengsci.2018.02.003.

40) G. Kim and J. Kim, “Compliant bistable mechanism for low frequency vibration energy harvester inspired by auditory hair bundle structures,” *Smart Mater. Struct.*, vol. 22, no. 1, pp. 1–6, 2013, doi: 10.1088/0964-1726/22/1/014005.

41) M. A. Karami, J. R. Farmer, and D. J. Inman, “Parametrically excited nonlinear piezoelectric compact wind turbine,” *Renew. Energy*, vol. 50, pp. 977–987, 2013, doi: 10.1016/j.renene.2012.07.037.

42) M. T. Todaro *et al.*, “Piezoelectric MEMS vibrational energy harvesters : Advances and outlook,” *Microelectron. Eng.*, vol. 183–184, pp. 23–36, 2017, doi: 10.1016/j.mee.2017.10.005.

43) F. Khameneifar, S. Arzanpour, and M. Moallem, “A Piezoelectric Energy Harvester for Rotary Motion Applications : Design and Experiments,” *Trans. Mechatronics*, vol. 18, no. 5, pp. 1527–1534, 2013, doi: 10.1109/TMECH.2012.2205266.

44) M. Argent, A. Mcdonald, W. Leithead, and A. Giles, “Optimisation of design and operation of generators for offshore vertical axis wind turbines,” *Wind Energy*, vol. 22, no. May 2017, pp. 1324–1342, 2019, doi: 10.1002/we.2359.

45) I. Izadgoshasb, Y. Y. Lim, N. Lake, L. Tang, R. V. Padilla, and T. Kashiwao, “Optimizing orientation of piezoelectric cantilever beam for harvesting energy from human walking,” *Energy Convers. Manag.*, vol. 161, no. January, pp. 66–73, 2018, doi: 10.1016/j.enconman.2018.01.076.

46) A. Felix *et al.*, “Wave Energy in Tropical Regions : Deployment Challenges , Environmental and Social Perspectives,” *J. Mar. Sci. Eng.*, vol. 7, no. 219, pp. 1–21, 2019, doi: 10.3390/jmse7070219.

47) K. B. Tawfiq, A. S. Mansour, H. S. Ramadan, M. Becherif, and E. E. El-Kholy, “Wind Energy Conversion System Topologies and Converters : Wind Energy Conversion System Topologies and Converters : Comparative Review,” *Energy Procedia*, vol. 162, pp. 38–47, 2019, doi: 10.1016/j.egypro.2019.04.005.

48) M. Hamlehdar, A. Kasaeian, and M. R. Safaei, “Energy harvesting from fluid flow using piezoelectrics : A critical review,” *Renew. Energy*, vol. 143, no. Dec, pp. 1826–1838, 2019, doi: 10.1016/j.renene.2019.05.078.

49) Z. Yang, A. Erturk, and J. Zu, “On the efficiency of piezoelectric energy harvesters,” *Extrem. Mech. Lett.*, vol. 15, no. May, pp. 26–37, 2017, doi: 10.1016/j.eml.2017.05.002.

50) A. Uihlein and D. Magagna, “Wave and tidal current energy – A review of the current state of research beyond technology,” *Renew. Sustain. Energy Rev.*, vol. 58, no. Jan, pp. 1070–1081, 2016, doi: 10.1016/j.rser.2015.12.284.

51) K. Haikonen, J. Sundberg, and M. Leijon, “Characteristics of the Operational Noise from Full Scale Wave Energy Converters in the Lysekil Project: Estimation of Potential Environmental Impacts,” *Energiesnergies*, vol. 6, pp. 2562–2582, 2013, doi: 10.3390/en6052562.

52) S. Patrício, A. Moura, and T. Simas, “Wave Energy and Underwater Noise : State of Art and Uncertainties,” in *OCEANS 2009-Europe*, 2009, pp. 1–5, doi: 10.1109/OCEANSE.2009.5278302.

53) G. Rinaldi, P. R. Thies, R. Walker, and L. Johanning, “On the Analysis of a Wave Energy Farm with Focus on Maintenance Operations,” *J. Mar. Sci. Eng.*, vol. 4, no. 51, pp. 1–11, 2016, doi: 10.3390/jmse4030051.

54) F. Rémouit, M. Chatzigiannakou, A. Bender, I. Temiz, J. Sundberg, and J. Engström, “Deployment and Maintenance of Wave Energy Converters at the Lysekil Research Site : A Comparative Study on the Use of Divers and Remotely-Operated Vehicles,” *J. Mar. Sci. Eng.*, vol. 6, no. 39, pp. 1–21, 2018, doi: 10.3390/jmse6020039.

55) A. Alsaadi, Y. Shi, L. Pan, J. Tao, and Y. Jia, “Vibration energy harvesting of multifunctional carbon fibre composite laminate structures,” *Compos. Sci. Technol.*, vol. 178, no. January, pp. 1–10, 2019, doi: 10.1016/j.compscitech.2019.04.020.

56) H.Kim, Y.Tadesse, S.Priya, “Energy Harvesting Technologies” Ed. S.Priya, D.J.Inman, Springer, 2009, pp.3-40, doi: 10.1007/978-0-387-76464-1 1.

57) Smart-Materials MFC products engineering properties, Shear modulus.

58) D. Steck, J. Qu, S. B.Kordmahale, D. Tscharnuter, A. Muliana, and J. Kameoka, “Mechanical responses of Ecoflex silicone rubber : Compressible and incompressible behaviors,” *J. Appl. Polym. Sci.*, vol. 136, no. 5, pp. 1–11, 2019, doi: 10.1002/app.47025.

59) A. P. Saghati, S. B. Kordmahale, A. P. Saghati, J. Kameoka, and K. Entesari, “Reconfigurable quarter-mode SIW antenna employing a fluidically switchable via,” in *2016 IEEE Antennas and Propagation Society International Symposium, APSURSI 2016 - Proceedings*, 2016, pp. 845–846, doi: 10.1109/APS.2016.7696131.

60) A. P. Saghati, S. B. Kordmahale, J. Kameoka, and K. Entesari, “Reconfigurable Quarter-Mode Substrate Integrated Waveguide Cavity Filter Employing Liquid-Metal Capacitive Loading,” in *2015 IEEE MTT-S International Microwave Symposium*, 2015, pp. 20–22, doi: 10.1109/MWSYM.2015.7166885.

61) P.-J. Huang, S. Baghbani Kordmahale, C.-K. Chou, H. Yamaguchi, M.-C. Hung, and J. Kameoka, “Development of automated high throughput single molecular microfluidic detection platform for signal transduction analysis,” in *SPIE 9705, Microfluidics, BioMEMS, and Medical Microsystems XIV*, vol. 9705, pp. 1–5, doi: 10.1117/12.2213259.

62) S. Baghbani Kordmahale and J. Kameoka, “Smart Soft Actuation System,” *Ann. Mater. Sci. Eng.*, vol. 2, no. c, pp. 2–3, 2015, [Online]. Available: https://austinpublishinggroup.com/material-science-engineering/fulltext/amse-v2-id1021.php.

63) Y. Yang, L. Tang, and H. Li, “Vibration energy harvesting using macro-fiber composites,” *Smart Mater. Struct.*, vol. 18, no. 11, pp. 1–8, 2009, doi: 10.1088/0964-1726/18/11/115025.

64) L. Tang, Y. Yang, and H. Li, “Optimizing efficiency of energy harvesting by macro-fiber composites,” in *SPIE 7268, Smart Structures, Devices, and Systems IV*, 2008, vol. 726808, no. December 2008, pp. 1–9, doi: 10.1117/12.810682.

65) T. Kashiwao, I. Izadgoshasb, Y. Y. Lim, and M. Deguchi, “Optimization of rectifier circuits for a vibration energy harvesting system using a macro-fiber composite piezoelectric element,” *Microelectronics J.*, vol. 54, pp. 109–115, Aug. 2016, doi: 10.1016/j.mejo.2016.05.013.

66) S. Baghbani Kordmahale, J. Do, K.-A. Chang, and J. Kameoka, “Low Cost and Piezoelectric based Soft Wave Energy Harvester,” *MRS Adv.*, vol. 4, no. 15, pp. 889–895, 2019, doi: 10.1557/adv.2018.675.

67) R. G. Dean and R. A. Dalrymple, *Water Wave Mechanics for Engineers and Scientists*. World Scientific Publishing Company, 1991, doi:10.1142/1232.

CHAPTER IV

SUMMARY AND FUTURE WORK

4-1-Summary

In the research demonstrated in this dissertation, combinations of soft materials and elements were used successfully to form several tools. The development of the devices was in two different directions. The first direction was toward the tools with biomedical applications. The second direction was toward sustainable water wave energy harvesting. For each presented project in this dissertation, there have been various steps. First, after reviewing the literature about required devices, proper devices with the required functionality were designed. Also, available fabrication and characterization equipment and facilities were evaluated. In addition, the process for each device development had to be optimized, based on the fabrication amenities limitations, to meet the required functionality. Alongside optimization of the fabrication process, like choosing the proper 3D printing technique, selecting the appropriate material is another important measure. PDMS and Ecoflex are two main soft materials that were used to develop the required devices. In the presented research, the developed tools were characterized successfully, and the devices executed the required functionality of their purpose.

Because the backbone of the developed fabrication methods has been based on 3D printing, various 3D printers were investigated and their printing process was optimized for the required structures and devices. The investigation of 3D printers proved their ability to meet the commercially released specifications. Perfactory Micro-printer developed by EnvisionTEC showed the highest resolution. Form-2 from the FormLabs was the second accurate 3D printer.

The MakerGear M2 extrusion 3D printer showed the lowest precision. Based on the insight obtained through primitive experiments, the proper 3D printer was chosen for each fabrication.

Soft material molding was the method that was used successfully to shape the soft elastomers in the presented projects. As it was mentioned before, this method is a simple and low-cost method in comparison with standard lithography to form microrobots and microchannels in microfluidics. To improve the surface quality of the molds, several methods, like TCE polymerization and TCS evaporation, were tested. These surface modifications made the surface of 3D printed molds more hydrophobic and made it easier to remove the cured polymers from them without any residual elastomer. TCS evaporation was chosen as a simple and fast method that improved the surface remarkably, increased the hydrophobicity, and increased the number of repetitive uses of the same mold for successive fabrication.

In chapter 2, the development steps of microrobotic devices with application in microscale manipulation, biospecimen manipulation, and Minimally Invasive Surgery (MIS) are described. The presented devices were designed based on the hydraulic/pneumatic actuation of a deformable membrane. The deformable membrane with three fingers placed on it, as a monolithic structure, was fabricated by using PDMS as the material and through soft material molding. The pressure deviation between two sides of the membrane can bend it and cause the fingers placed on it being opened or closed. The safe 300µm size was chosen as the diameter of the fingers. This size selection was based on the resolution of the Perfactory Micro 3D printer by EnvisionTEC and the safe removing of the cured PDMS from the mold. After 3D printing the molds of the microhand structures, the required surface treatments were done on it to make it usable for PDMS mold casting. The curing of very soft PDMS was done at 25°C at room temperature.

The fabrication of devices was finished by assembling them. Two different types of microhands were developed and presented in this chapter. First, was the one compatible with microfluidic technology. The second was the compatible one with the syringe tip. The successfully fabricated devices were characterized under an optical microscope, and volume-deflection and volume-force curves were obtained. To prove the ability of these devices to manipulate fragile biospecimen, an embryonic cell in the aqueous medium and an ant in the air were manipulated successfully. The same concept and design were used to develop a surgical device for MIS that is matched with the size of standard trocars. For this small hand-like tool, the fingers were 3D printed and assembled on the flexible membrane. The handling of a piece of chicken was done successfully to mimic the manipulation of abdominal organs.

In chapter 3, the development steps for a blue energy harvesting device, based on a soft material platform, are presented. The Ecoflex 030 was chosen as the soft elastomer for the fabrication of the Wave Energy Converters (WECs). To form a flexible and floatable structure as a Wave Energy Converter, a proper flexible transducer and a piece of normal bubble wrap were integrated into a sheet of elastomer. The required transducer should be flexible and durable. A piezoelectric P2-type Macro Fiber Composite (MFC), made by Smart Materials, was chosen as the transducer. The parallel electrical connection of transducers was chosen as the proper configuration to maximize the outcome. The WECs outputs were connected to a diode bridge to make it DC and make it possible to compare the results of various WECs. These WECs showed that can be used as self-powered sensors. All the data acquisitions were done by using a TI data acquisition unit controlled by LabVIEW. To characterize the fabricated WECs, at first, they were placed vertically in the flume to check the relation between bending value, power production

potential, and real power production. Then they were placed in horizontal configuration to check if they can work as floatable WECs. The optimized number of MFCs in the device was determined for this horizontal configuration. Finally, the anchoring configuration was changed to the one-sided horizontally anchored configuration, and its effect was investigated on the power production. It was found that the one-sided horizontally anchored configuration led to the maximum power production, while the vertical anchoring caused it to produce the least. The WECs with 3 MFCs showed the maximum power production in the flume.

4-2-Future Works

Future works can be in both directions of biomedical devices and energy harvesting. The innovative devices for laparoscopy can be developed and an animal surgery experiment can be conducted with it. Also, proper sensors can be integrated with the fingers as the haptic sensor to improve the functionality and controllability of the device for biospecimen manipulation or MIS. Moreover, the developed microhand structures can be tested for microsurgery.

The wave energy conversion systems can be developed based on the various piezo elements and various sizes for the required energy level. Various configurations of the MFCs can be investigated to optimize the WECs. They can be used for remote sensing applications and as self-powered sensors or to drive communication and remote sensing equipment.

APPENDIX A

The various steps for the process of soft material mold-casting that was used in this research are listed in detail in this appendix. Two soft materials, PDMS and Ecoflex 030, have been used as soft elastomers.

1-Mold Fabrication and Preparation

The mold fabrication was used by using EnvisionTEC Perfactory-Micro 3D printer. The HTM 140 V2 M liquid photopolymer, produced and distributed by EnvisionTEC, was used as the 3D printer material. The steps to fabricate and finalize the proper 3D printed mold are listed below:

1- The proper design should be prepared by the designer. The feasibility of 3D printing should be checked, and the proper direction of printing should be determined by the designer. A file in STL format of the design should be used for EnvisionTEC 3D printer.

2- The 3D printer's tray should be half-filled with HTM 140 V2 M liquid photopolymer. The liquid polymer should be clean and without any solidified particles.

3- The 3D printing should be executed.

4- After finishing the 3D printing, the solidified 3D printed device should be removed from the 3D printer's holder. Extra supports should be removed carefully. Then the 3D printed part should be washed with IPA. If the 3D printed device has small features like small holes, the washing should be followed by 10-60 seconds of sonication in IPA. And another round of washing with IPA.

5- The washed devices should be dried by N_2.

6- The 3D printed device should be placed in the light-curing system, developed by EnvisionTEC, and be cured for 2000 pulses of intense light.

7- The light-cured 3D printed devices should be placed in the oven at 65°C for 72 hours

8- The 3D printed, light-cured, and thermally-cured devices need another step of Silane surface treatment to be a proper soft material mold. The Silane treatment helped the molds to be reusable and the cured soft materials could be removed from the mold easily without any unwanted residue.

Note: The light curing system, developed by EnvisionTEC, is shown in figure 57. This light-curing system can light cure the 3D printed elements by using pulses of high-intensity white light.

Figure.57. The light-curing system developed by EnvisionTEC.

Note: An oven with a precise temperature control system should be used. In figure58, the oven that was used in the device's thermal treatment is shown.

Figure.58. The oven with precise temperature control that was used for 3D printed parts thermal treatment.

2-PDMS Mold Casting

PDMS is a biocompatible, transparent, and flexible soft material that can be used in various kinds of device fabrication. PDMS mold casting is an effective and low-cost method that can be used to form PDMS in a proper shape. The steps of this process are as mentioned below:

1- Monomer and curing agent should be mixed in a proper ratio. 10 part of monomer and 1 part of curing agent is a usually used ratio that can be used for microfluidic device fabrications (10:1).
2- After mixing two parts of liquid PDMS, the resulted mixture should be placed in a desiccator, the pressure should go down to vacuum, and the entrapped bubbles should be removed from the mixture in the vacuum.
3- The un-bubbled liquid PDMS should be dispensed in the prepared mold.
4- If the mold contains small features like holes, it is essential to put the mold that contains liquid PDMS in the desiccator again and remove the entrapped bubbles.
5- The mold that contains liquid PDMS should be placed in the oven at 65° C for 4 hours.
6- The cured PDMS should be removed from the mold, carefully.

Note: Both desiccators with a handy pump or mechanical pump can be used to un-bubble the liquid PDMS. In figure 59, the photo images of desiccators and their handy pump can be seen. In figure 60, the desiccator with a mechanical pump is shown. The desiccators with mechanical pumps can go to higher levels of vacuum and remove all the bubbles faster.

Figure.59. The desiccators and their handy pump.

Figure.60. The desiccator with a mechanical pump.

3-Ecoflex Mold Casting

Ecoflex 030 is a biocompatible, flexible, and stretchable elastomer. Ecoflex 030 widely have been used in soft robotic investigations and fabrications. The Ecoflex 030 has been used in this research to encapsulate MFCs and electrical connections among them for making a flexible and floatable platform as a Wave Energy Converter. The process that is used has the following steps:

1- Two parts of Ecoflex 030 should be mixed in a 1:1 ratio.
2- The container of the very well mixed liquid elastomers should be placed in the desiccator and the entrapped bubbles should be removed in the vacuum.
3- After removing the bubbles, the liquid elastomer should be dispensed in the prepared mold.
4- If the mold contains small features like holes, it is essential to put the mold that contains liquid elastomer in the desiccator again and remove the entrapped bubbles.
5- The liquid Ecoflex 030 will be cured in 2 hours at room temperature.
6- The cured Ecoflex 030 should be removed carefully from the mold.

APPENDIX B

The formation of a self-assembled monolayer (SAM) of a hydrophobic layer on various layers can reduce friction and is essential in soft material casting. Several procedures can be used to form a hydrophobic layer. Here we have mentioned three different procedures that we have used in our projects.

1-Method 1

The first method is a liquid phase process and has three following steps.

1- Preparation of 0.01 mM toluene solution of Octadecyltrichlorosilane(OTS).

2- Immerse samples in 0.01 mM toluene solution of OTS for 6 hours at room temperature.

3- Baking the sample in an oven at 125°C for 1 hour.

The achieved thickness of OTS SAM through this method is around 10nm.

2-Method 2

The second method is in the gaseous phase and phase and has the following steps.

1- Preparation of 3-4 mM solution of Octadecyltrimethoxysilane (OTMS) in Trichloroethylene(TCE).

2- Spin coat the OTMS-TCE solution ate 3000RPM and for 10 seconds.

3- Place the prepared samples in a brown bottle.

4- Place a vial contains 1-2 ml of Hydrochloric Acid (HCl) or Ammonia Hydroxide (NH_4OH) into the brown bottle, alongside small silica particles. Silica particles will absorb the moisture and will prevent the moisture to catalyze multilayer polymerization.

5- Tightly close the lid of the brown bottle.

6- Let the monolayer form in at least 6 hours.

7- Sonicate samples for 3 minutes in each of Toluene, Acetone, Isopropyl Alcohol, and DI water.

8- Rinse the samples with solvents.

9- Dry samples with N_2.

The achieved SAM that can be formed through this method is highly uniform and durable with 10nm thickness.

3-Method 3

This method is a simple and fast method at the gaseous phase. There in this process will not be any chemical polymerization and just physical evaporation/deposition will occur. This process is compatible with 3D printed polymeric devices and can be used for surface treatment of these devices. Use of UCT's (United Chemical Technologies) special chemical for mold-making process contains (Tridecafluro-1,1,2,2-Tetrahydrooctyl)-1-Trichlorosilane with the commercial number (T2492-KG) is essential in this method. A desiccator connected to a vacuum pump is also needed to execute this process.

This method has the following steps.

1- Put three drops of (Tridecafluro-1,1,2,2-Tetrahydrooctyl)-1-Trichlorosilane in a container.

2- Place the container that contains liquid in a desiccator side-by-side the samples.

3- Close the desiccator lid and turn on the vacuum pump.

4- Leave the sample and container that contains liquid in a vacuum for 5 mins.

5- Vent the desiccator under the hood.

6- Wash the sample with IPA.

7- Dry the sample with N_2.

This fast method is safe for polymeric 3D printed molds. The desiccator that was used for this process can be seen in figure 61.

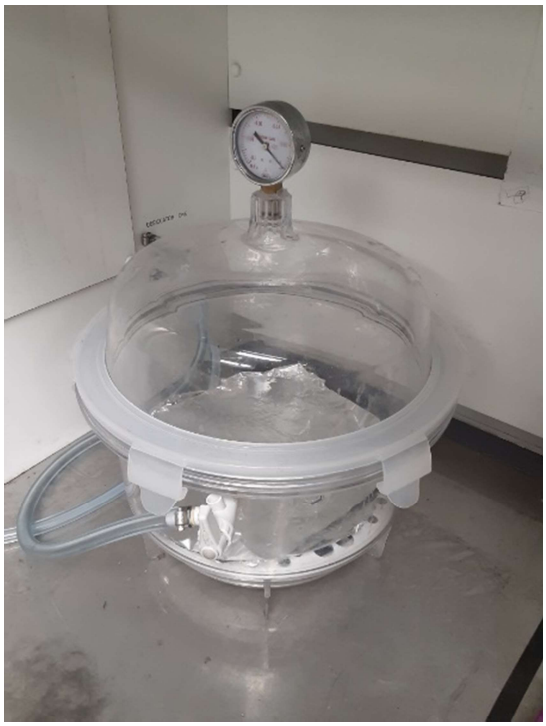

Figure.61. The desiccator has been used for 3D printed surface modification by using gases contain silane compounds.

APPENDIX C

A user subroutine UMAT code is attached below.

```
SUBROUTINE UMAT(STRESS,STATEV,DDSDDE,SSE,SPD,SCD,
    1 RPL,DDSDDT,DRPLDE,DRPLDT,STRAN,DSTRAN,
    2 TIME,DTIME,TEMP,DTEMP,PREDEF,DPRED,MATERL,NDI,NSHR,NTENS,
    3 NSTATV,PROPS,NPROPS,COORDS,DROT,PNEWDT,CELENT,
    4 DFGRD0,DFGRD1,NOEL,NPT,KSLAY,KSPT,KSTEP,KINC)
C
     INCLUDE 'ABA_PARAM.INC'
C
     CHARACTER*8 MATERL
     DIMENSION STRESS(NTENS),STATEV(NSTATV),
    1 DDSDDE(NTENS,NTENS),DDSDDT(NTENS),DRPLDE(NTENS),
    2 STRAN(NTENS),DSTRAN(NTENS),DFGRD0(3,3),DFGRD1(3,3),
    3 TIME(2),PREDEF(1),DPRED(1),PROPS(NPROPS),COORDS(3),DROT(3,3)
C LOCAL ARRAYSS
C - - - - - - - - - - - - - - - - - - - - - - - - - - - - - - - - - - - - - - - - - - - - - -
C BBAR - DEVIATORIC RIGHT CAUCHY-GREEN TENSOR
C DISTGR - DEVIATORIC DEFORMATION GRADIENT (DISTORTION TENSOR)
C - - - - - - - - - - - - - - - - - - - - - - - - - - - - - - - - - - - - - - - - - - - - - -
C
     DIMENSION BBAR(6),B(6),DISTGR(3,3)
```

```
C
      PARAMETER(ZERO=0.D0, ONE=1.D0, TWO=2.D0, THREE=3.D0, FOUR=4.D0,
     1 EIGHT=8.D0, NINE=9.D0)

C - - - - - - - - - - - - - - - - - - - - - - - - - - - - - - - - - - - - - - - - - - - - - - - - - -
C FOR LOW D1 HYBRID ELEMENTS SHOULD BE USED
C - - - - - - - - - - - - - - - - - - - - - - - - - - - - - - - - - - - - - - - - - - - - - - - - - -
- - - - - - - - - - - - - - - - - - - - - - - - - - - - - - - -
      REAL*8 EMU, EJM, TERM, TRBBAR,TERM1, TERM2, TERM3, DUDJ, DDUDDJ,
     1 DWDI1, DDWDDI1, TRBBAR, DET, SCALE
C ELASTIC PROPERTIES
C
      EMU=PROPS(1)
      EJM=PROPS(2)
      AK= PROPS(3)
C
C JACOBIAN AND DISTORTION TENSOR
C Define DET=J

      DET=DFGRD1(1, 1)*DFGRD1(2, 2)*DFGRD1(3, 3)
     1 -DFGRD1(1, 2)*DFGRD1(2, 1)*DFGRD1(3, 3)
      IF(NSHR.EQ.3) THEN
```

```
      DET=DET+DFGRD1(1, 2)*DFGRD1(2, 3)*DFGRD1(3, 1)
     1     +DFGRD1(1, 3)*DFGRD1(3, 2)*DFGRD1(2, 1)
     2     -DFGRD1(1, 3)*DFGRD1(3,1)*DFGRD1(2, 2)
     3     -DFGRD1(2, 3)*DFGRD1(3, 2)*DFGRD1(1, 1)
      END IF
      SCALE=DET**(-ONE/THREE)
      DO K1=1, 3
       DO K2=1, 3
        DISTGR(K2, K1)=SCALE*DFGRD1(K2, K1)
       END DO
      END DO
C
C CALCULATE LEFT CAUCHY-GREEN TENSOR
C
      BBAR(1)=DISTGR(1,1)**2+DISTGR(1,2)**2+DISTGR(1,3)**2
      BBAR(2)=DISTGR(2,1)**2+DISTGR(2,2)**2+DISTGR(2,3)**2
      BBAR(3)=DISTGR(3,3)**2+DISTGR(3,1)**2+DISTGR(3,2)**2
      BBAR(4)=DISTGR(1,1)*DISTGR(2,1)+DISTGR(1,2)*DISTGR(2,2)
     1        +DISTGR(1,3)*DISTGR(2,3)

      IF(NSHR.EQ.3) THEN
       BBAR(5)=DISTGR(1,1)*DISTGR(3,1)+DISTGR(1,2)*DISTGR(3,2)
```

```
     1      +DISTGR(1,3)*DISTGR(3,3)
      BBAR(6)=DISTGR(2,1)*DISTGR(3,1)+DISTGR(2,2)*DISTGR(3,2)
     1 +DISTGR(2,3)*DISTGR(3,3)
      END IF

C**********************************************************************
C UPDATE THE STRESS OF THE NEW NETWORK: ANISOTROPIC NEO-HOOKEAN ELASTIC
      I1BAR=BBAR(1)+BBAR(2)+BBAR(3)
      TRBBAR=(BBAR(1)+BBAR(2)+BBAR(3))/THREE
      DWDI1=EMU*EJM/TWO/(EJM+THREE-I1BAR)
      DDWDDI1=EMU*EJM/TWO/(EJM+THREE-I1BAR)**2
      DUDJ=AK/two*(DET-one/DET)
      DDUDDJ=AK/two*(one+one/DET**2)
       TERM1=-FOUR/(THREE*DET)*DWDI1
       TERM2=FOUR/DET*DDWDDI1
       TERM3=DET*DDUDDJ
      CALL CALCSTRESS(BBAR,TRBBAR,DET,DUDJ,DWDI1,NDI,NSHR,
     1 STRESS)
      CALL CALCTANGENT(DDSDDE,STRESS,BBAR,TRBBAR,DUDJ,
     1 DWDI1,DDWDDI1,TERM1,TERM2,TERM3,DET,NTENS,NSHR)
      RETURN
      END
```

```
      SUBROUTINE CALCSTRESS(BBAR,TRBBAR,DET,DUDJ,DWDI1,NDI,NSHR,
     1 STRESS)
      REAL*8 BBAR,TRBBAR,DET,DUDJ,DWDI1,STRESS
      DIMENSION BBAR(6),STRESS(6)
      PARAMETER(TWO=2.D0)
      INTEGER NDI,NSHR,K1
      DO K1=1,NDI
      STRESS(K1)=TWO/DET*DWDI1*(BBAR(K1)-TRBBAR)+DUDJ
      END DO
      DO K1=NDI+1,NDI+NSHR
      STRESS(K1)=TWO/DET*DWDI1*BBAR(K1)
      END DO
      RETURN
      END


C**********************************************************************
C UPDATE THE STIFFNESS
C UPDATE THE STIFFNESS OF THE FIRST NETWORK


C UPDATE THE STIFFNESS OF THE NEW NETWORK
      SUBROUTINE CALCTANGENT(DDSDDE,STRESS,BBAR,TRBBAR,DUDJ,
     1 DWDI1,DDWDDI1,TERM1,TERM2,TERM3,DET,NTENS,NSHR)
```

```
 REAL*8 DDSDDE,STRESS,BBAR,TRBBAR,DUDJ,DWDI1,DDWDDI1,
1 TERM1,TERM2,TERM3,DET
 DIMENSION DDSDDE(6,6),STRESS(6),BBAR(6)
 INTEGER NTENS,NSHR,K1,K2
 PARAMETER(TWO=2.D0, THREE=3.D0, FOUR=4.D0)
 DDSDDE(1, 1)=-DUDJ+TERM3+TWO*TERM1*(BBAR(1)-TWO*TRBBAR)+
1 TERM2*(BBAR(1)**TWO+TRBBAR*(-TWO*BBAR(1)+TRBBAR))+
2 TWO*STRESS(1)
 DDSDDE(2, 2)=-DUDJ+TERM3+TWO*TERM1*(BBAR(2)-TWO*TRBBAR)+
1 TERM2*(BBAR(2)**TWO+TRBBAR*(-TWO*BBAR(2)+TRBBAR))+
2 TWO*STRESS(2)
 DDSDDE(3, 3)=-DUDJ+TERM3+TWO*TERM1*(BBAR(3)-TWO*TRBBAR)+
1 TERM2*(BBAR(3)**TWO+TRBBAR*(-TWO*BBAR(3)+TRBBAR))+
2 TWO*STRESS(3)
 DDSDDE(1, 2)=DUDJ+TERM3+TERM1*(BBAR(1)+BBAR(2)-TRBBAR)+
1 TERM2*(BBAR(1)*BBAR(2)-TRBBAR*(BBAR(1)+BBAR(2))+
2 TRBBAR**TWO)
  DDSDDE(1, 3)=DUDJ+TERM3+TERM1*(BBAR(1)+BBAR(3)-TRBBAR)+
1 TERM2*(BBAR(1)*BBAR(3)-TRBBAR*(BBAR(1)+BBAR(3))+
2 TRBBAR**TWO)
 DDSDDE(2, 3)=DUDJ+TERM3+TERM1*(BBAR(2)+BBAR(3)-TRBBAR)+
1 TERM2*(BBAR(2)*BBAR(3)-TRBBAR*(BBAR(2)+BBAR(3))
```

```
2 +TRBBAR**TWO)
 DDSDDE(1, 4)=FOUR/DET*BBAR(4)*(-DWDI1/THREE+
1 DDWDDI1*(BBAR(1)-TRBBAR))+STRESS(4)
 DDSDDE(2, 4)=FOUR/DET*BBAR(4)*(-DWDI1/THREE+
1 DDWDDI1*(BBAR(2)-TRBBAR))+STRESS(4)
 DDSDDE(3, 4)=FOUR/DET*BBAR(4)*(-DWDI1/THREE+
1 DDWDDI1*(BBAR(3)-TRBBAR))
 DDSDDE(4, 4)=-DUDJ+TWO/DET*(TRBBAR*DWDI1+
1 TWO*DDWDDI1*BBAR(4)**TWO)+(STRESS(1)+STRESS(2))/TWO
 IF(NSHR.EQ.3) THEN
 DDSDDE(1, 5)=FOUR/DET*BBAR(5)*(-DWDI1/THREE+
1 DDWDDI1*(BBAR(1)-TRBBAR))+STRESS(5)
  DDSDDE(2, 5)=FOUR/DET*BBAR(5)*(-DWDI1/THREE+
1 DDWDDI1*(BBAR(2)-TRBBAR))
 DDSDDE(3, 5)=FOUR/DET*BBAR(5)*(-DWDI1/THREE+
1 DDWDDI1*(BBAR(3)-TRBBAR))+STRESS(5)
  DDSDDE(1, 6)=FOUR/DET*BBAR(6)*(-DWDI1/THREE+
1 DDWDDI1*(BBAR(1)-TRBBAR))
  DDSDDE(2, 6)=FOUR/DET*BBAR(6)*(-DWDI1/THREE+
1 DDWDDI1*(BBAR(2)-TRBBAR))+STRESS(6)
  DDSDDE(3, 6)=FOUR/DET*BBAR(6)*(-DWDI1/THREE+
1 DDWDDI1*(BBAR(3)-TRBBAR))+STRESS(6)
```

```
 DDSDDE(5, 5)=-DUDJ+TWO/DET*(TRBBAR*DWDI1+
1 TWO*DDWDDI1*BBAR(5)**TWO)+(STRESS(1)+STRESS(3))/TWO
 DDSDDE(6, 6)=-DUDJ+TWO/DET*(TRBBAR*DWDI1+
1 TWO*DDWDDI1*BBAR(6)**TWO)+(STRESS(2)+STRESS(3))/TWO
 DDSDDE(4,5)=TERM2*BBAR(4)*BBAR(5)+STRESS(6)/TWO
 DDSDDE(4,6)=TERM2*BBAR(4)*BBAR(6)+STRESS(5)/TWO
 DDSDDE(5,6)=TERM2*BBAR(5)*BBAR(6)+STRESS(4)/TWO
 END IF
 DO K1=1, NTENS
 DO K2=1, K1-1
  DDSDDE(K1, K2)=DDSDDE(K2, K1)
 END DO
 END DO
 RETURN
 END
```